UNIVERSITÀ
POLITECNICA
DELLE MARCHE

Università Politecnica delle Marche

DIPARTIMENTO DI INGEGNERIA INDUSTRIALE E SCIENZE MATEMATICHE
Corso di Dottorato di Ricerca in Ingegneria Industriale – Curriculum Ingegneria Energetica

PH.D. THESIS

Design, Manufacturing, Testing, and Mathematical Modeling of Concentrating Solar Systems: a Study Applied to Prototypes of Parabolic Trough Collector and Solar Box Cooker

Advisor:
Prof. Giovanni Di Nicola

Ph.D. Dissertation of:
Gianluca Coccia

Curriculum Supervisor:
Prof. Ferruccio Mandorli

XV Edition – New Series

Gianluca Coccia: *Design, Manufacturing, Testing, and Mathematical Modeling of Concentrating Solar Systems: a Study Applied to Prototypes of Parabolic Trough Collector and Solar Box Cooker,* Ph.D. Thesis, © Novemeber 2016.

To Jessica

Contents

List of Figures

List of Tables

Abstract

Use of solar thermal energy has to be sustained to reduce consumption of climate-changing fossil fuels. Thus, in this study two concentrating solar prototypes were designed and manufactured: a parabolic trough collector (PTC) and a solar box cooker.

The PTC has a 90° rim angle and a concentration ratio of 19.89. The concentrator is a sandwich composite structure with high-reflectance aluminum foils applied on it. The receiver is a steel pipe painted with a selective coating. The tracking system is based on a solar-position computer program. Experimental tests were carried out with water and temperatures up to 85 °C. Thermal efficiency, incident angle modifier, and time constant curves were found. Results show that the thermal efficiency equation is comparable with that of other PTCs in literature.

Experimental data were utilized to validate a simulation environment able to determine the yearly yield of PTCs. The simulation was carried out to evaluate the convenience in adopting metal-based nanofluids respect to the base fluid (water). Five inlet fluid temperatures and three mass flow rates were analyzed. Results show that only Au, TiO_2, ZnO, and Al_2O_3 nanoparticles, at the lowest concentrations, present reduced improvements respect to water.

The solar box cooker is a high concentration ratio prototype (11.57). The cooker has a cooking chamber with a glass cover on the top and is composed by two rows of booster mirrors. The prototype allows both a solar azimuth and zenith manual orientation. Tests without load were carried out to evaluate the maximum cooker temperature. Tests with load, conduced using aluminum vessels containing a certain amount of water, were accomplished both with non-painted vessels and black-coated ones, and with one or two vessels. Additional tests were carried out with peanut oil. Using this fluid, temperatures higher than the water ones were achieved (> 200 °C) and results exhibited values comparable to those in literature.

Sommario

L'utilizzo di energia solare termica deve essere sostenuto per ridurre il consumo di fonti fossili climalteranti. Nel presente studio si sono progettati e realizzati due sistemi solari a concentrazione: un collettore parabolico assiale (PTC) ed un forno solare a scatola.

Il PTC ha un angolo di bordo di 90° ed un rapporto di concentrazione di 19,89. Sul concentratore, realizzato in sandwich composito, sono state applicate pellicole in alluminio ad elevata riflettanza. Il ricevitore è un tubo di acciaio rivestito da una vernice selettiva. Il sistema di inseguimento è governato da un algoritmo solare. I test sperimentali sono stati condotti con acqua ad una temperatura massima di 85 °C. Il PTC è stato caratterizzato ottenendo curve di efficienza termica, modificatore dell'angolo di incidenza e costante di tempo. I risultati mostrano che l'equazione dell'efficienza termica è confrontabile con quella di collettori simili.

I dati sperimentali sono stati utilizzati per validare un ambiente di simulazione della resa annuale di PTC. Si è determinata la convenienza nell'adozione di nanofluidi a base di metalli rispetto al fluido di base (acqua). Sono state analizzate 5 temperature del fluido in ingresso e 3 portate in massa. I risultati mostrano che solo le nanoparticelle di Au, TiO2, ZnO e Al2O3 alle più basse concentrazioni presentano ridotti miglioramenti.

Il forno solare a scatola ha un rapporto di concentrazione di 11,57, ed è costituito da una camera di cottura, un coperchio superiore vetrato e una doppia fila di specchi riflettenti. Il prototipo consente un allineamento solare manuale sia azimutale che zenitale. La temperatura massima del forno è stata determinata attraverso prove a vuoto. Sono state inoltre svolte prove a carico inserendo nel forno una o due pentole di alluminio, verniciate o meno in nero, riempite con acqua o olio di arachidi. In quest'ultimo caso, si è giunti a temperature superiori a 200 °C e a risultati confrontabili con quelli in letteratura.

Inde cibum coquere ac flammae mollire vapore
sol docuit, quoniam mitescere multa videbant
verberibus radiorum atque aestu victa per agros.

— Titus Lucretius Carus, De rerum natura V, vv. 1102–1104

Acknowledgments

Firstly, I would like to thank Prof. Giovanni Di Nicola for his assistance, support, and collaboration during my doctoral carrier. I am grateful to Dr. Giulio Santori and Eng. Adio Miliozzi, who accepted to spend their time and efforts to review this thesis. I thank Eng. Miliozzi for his kind technical support on phase change materials, too.

My thanks also go to all the people who have worked with me in this period: my colleague Dr. Mariano Pierantozzi, the technicians of DIISM (Department of Industrial Engineering and Mathematical Sciences), the ICT (Institute of Construction Technologies) researchers of Padua (Italy), and all the students with whom I had the pleasure to share my experience. In particular, I'd like Eng. Giuliano Giuliani, Gabriele Gabrielli, and Gaetano Borrelli to know I appreciated their help with my experimental activities; the same feeling is addressed to Dr. Laura Colla, Dr. Laura Fedele, and Dr. Sergio Bobbo. As concerns students, I would like to express my special gratitude to everyone who has contributed to realize some parts of this thesis. I have decided not to report the entire list of people involved, as it would be extremely long. I hope this decision will be understood by everyone.

My special thanks go to Eng. Gianni Crovatto too, for his appreciated advices about solar cookers, and to Ms. Debra Tranquilli, for her priceless help in the English revision of the thesis.

In addition, I cannot forget to be grateful to Eng. Marco Sotte, Ph.D., who, in DIISM, originally undertook an experimental program called PTC.project. This program marked the beginning of my work on parabolic trough collectors.

Finally, I would like to thank my parents for all their continuous assistance and support; without them, I doubt that this work could have existed.

Ancona, Novemeber 2016 G. C.

Introduction

Global energy demand, and thermal energy demand in particular, is continuously increasing. In order to reduce consumption of climate-changing fossil fuels, use of renewable sources such as solar thermal energy has to be encouraged and sustained.

Thus, this thesis is focused on concentrating solar collectors, systems able to convert solar energy into heat through the utilization of special reflective mirrors and other optical devices. There are various types of solar collectors; this manuscript shows the work developed on prototypes of parabolic trough collector (PTC) and solar box cooker. Both the devices were intended to be used for low and medium enthalpy (or low and medium temperature) demands, for temperatures up to about 85 and 300 °C for the PTC and the box cooker, respectively.

The manuscript is divided into five chapters. The state of the art is presented in Chapter 1, which is about solar thermal engineering fundamentals and classification of solar collectors and cookers available on the market. PTCs are usually classified by dividing them into two different parts: the concentrator and the receiver. Solar box cookers, instead, are presented as a specific classification of solar cookers. Solar thermal applications involving such devices are also discussed.

Chapter 2 provides a detailed description of the PTC prototype design and realization. This prototype, called UNIVPM.02, is a greater and more complex version of the previous one, UNIVPM.01. Both the PTCs were designed and manufactured in DIISM (Department of Industrial Engineering and Mathematical Sciences). UNIVPM.02 is a 90° rim angle PTC, having a concentration ratio of 19.89. The concentrator structure is based on a sandwich composite composed by two inside fill components: fiberglass as reinforcing material and low-density polyvinyl chloride (PVC) as matrix. The external shell was gel-coated. Aluminum reflective foils with high reflectance in the solar spectrum were applied on the concentrator surface to focus solar radiation in the parabola focal line. The receiver, placed in the focal line, is a not-evacuated steel circular tube, painted with a selective coating. In this way, absorption of solar energy was augmented and radiative heat losses with the environment were reduced. The tracking system, operated by an electric engine, can be manual or automatic. In this last case, the concentrator rotation is ruled by a solar tracking algorithm. The design and manufacturing processes are firstly introduced then, the test bench used to evaluate the collector thermal efficiency is reported. Tests were performed according to the directives of ANSI/ASHRAE Standard 93-2010 and using demineralized water at temperatures up to 85 °C. The equation obtained for the thermal efficiency is comparable to that of other similar collectors available in literature.

A way to improve a low-enthalpy PTC thermal efficiency could lie in the adoption of heat transfer fluids alternative to water. Thus, nanofluids, i.e. solutions composed by a base fluid (e.g., water) and a solute uniformly dispersed in form of solid particles with nanometric dimension, were studied. Different types of nanoparticles were analyzed in literature: oxide ceramics, nitride ceramics, carbide ceramics, metals, semiconductors, carbon nanotubes, carbon nanohorns, and composite materials. If the suspension is stable, a reduced quantity of nanoparticles could have the potential to increase the thermal properties of the base fluid. In Chapter 3, the results of thermal conductivity and dynamic viscosity measurements, carried out for six water-based nanofluids, are reported. The nanoparticles under study were: Fe_2O_3 (5, 10, 20 wt%), SiO_2 (1, 5, 25 wt%), TiO_2 (1, 10, 20, 35 wt%), ZnO (1, 5, 10 wt%), Al_2O_3 (0.1, 1, 2 wt%), and Au (0.01 wt%). A simulation environment, built to evaluate the yearly yield of a nanofluid-based PTC, is then presented. The inputs of the simulation environment include fluid and material properties, geometrical features of the systems, plant working conditions, sun position, and a hourly-resolution typical meteorological year. The mathematical model of the simulation environment was validated through experimental tests carried out on the prototypes UNIVPM.01 and UNIVPM.02. The model was coupled with a specific low-temperature heat demand profile: 5 inlet fluid temperatures (40, 50, 60, 70, 80 °C) and 3 mass flow rates (0.5, 1, 1.5 kg/s) were analyzed. Results, which are provided through a direct comparison with water, prove that there is no general convenience in adopting nanofluids, at least for the low-temperature applications under study.

The design, manufacture, and testing of a prototype of solar box cooker is presented in Chapter 4. This prototype, based on a freeware design, has a concentration ratio of 11.57 and was manufactured in DIISM. It was modified in some components (absorber coating, reflecting mirrors, glass double cover, insulation material) to increase thermal insulation and optical efficiency. The cooker is composed by an internal metal box used as cooking chamber, with a glass cover on the top. In the higher part of the container, there is a double row of mirrors. Each row has a different inclination angle respect to the horizontal plane. The cooker has two border wooden hands and two wheels that allow its movement and its azimuth orientation. Moreover, a zenith orientation is possible thanks to a rotation around the horizontal axis. In the cooking chamber, there is a rotating vessel support able to rotate of 360°, so that it can maintain in balance the vessels put on it when the zenith orientation changes.

The test bench used for the oven characterization was realized to satisfy different experimental procedures available in literature. Two kinds of experimental test were carried out: with and without load. Tests without load allowed to evaluate the maximum temperature of the cooker. Tests with load, otherwise, were conduced putting in the cooking chamber aluminum vessels (18 cm diameter and 16 cm high) able to contain about four liters of fluid. Such tests were done both with non-painted vessels and black-coated ones, in order to evaluate the differences in performance. In addition, experimental tests with one vessel containing water and with two vessels containing the same amount of fluid were carried out. Results showed some differences respect to the procedures usually followed in literature; these differences could be due to the high insulation level of the cooker. In order to deeply investigate this behavior, an additional type of tests was conduced, using one and two black-painted vessels filled with peanut oil instead of water. In this case, temperatures higher respect to water ($> 200\,°C$) were achieved, and results exhibited not only values comparable to those in literature, but also considerable performances.

Finally, Chapter 5 reports some critical conclusions and future advancements of the work presented.

In order to give a complete overview on solar collectors, Appendix A and Appendix B describe a complete mathematical model for PTCs and the available standards used to test these solar collectors, respectively.

Chapter 1

Overview on Solar Thermal Energy

In this introductory chapter, fundamentals of solar thermal energy are discussed. Further, solar thermal collectors and solar cookers, devices able to convert solar energy into heat, are briefly presented. Among these, parabolic trough collectors (PTCs) and solar box cookers, which are the main subjects of this thesis, are introduced. PTCs are usually studied by dividing them into two different parts: the concentrator and the receiver. Instead, solar box cookers are presented as a specific classification of solar cookers, which can fall within several categories. The materials used in such devices and their working principle are also discussed. Finally, typical solar thermal applications are presented, in particular as regards their utilization with PTCs and solar box cookers.

1.1 The Role of Heat and Solar Thermal Energy

The growth in energy consumption over the past 20 years has been significant and demand for energy will continue to grow due to global population increase. Even though the demand for electric energy is generally considered of maximum importance, civil and industrial processes based on heat are not less relevant. A paper published by IEA (International Energy Agency) in 2014 [1] underlines that, nowadays, the production of heat accounts for more than 50% of global final energy consumption. One of the most important aspects of such sector is that heat use per capita varies considerably less than total energy use per capita between different world regions. This means that the need of thermal energy has a fundamental impact in all countries. Global energy use for heat in industry, buildings, and other sectors reached 172 EJ in 2011. About three-quarters (129 EJ) of global energy use for heat processes is met with fossil sources, leading to around 10 Gt of CO_2 emissions per year, one third of the global total in the energy sector.

In Europe, two-thirds of the energy demand consists of heat, and it is confirmed that about 50% of this heat demand (estimated at about 300 TWh in 2000) is required at temperatures up to 250 °C [2]. The global commercial low-temperature heat consumption is estimated to be about 10 EJ per year only for hot water production [3]. The only way to meet that global heat demand without contributing to climate change and environmental problems implies the utilization of renewable sources.

Several renewable heating technologies are already mature and can provide heat at costs competitive with fossil fuel-based heat in an increasing number of circumstances, thus providing a way to enhance energy security and reduce energy-related CO_2 emissions. Renewable energy accounts for 43% (36 EJ) of total energy use for heat in buildings, while in the industry sector, it accounts for 10% of the total. However, in both cases, most of heat comes from the use of traditional bioenergy. Only 4 EJ are currently produced by more sustainable renewable energy technologies: the largest contribution (3 EJ) comes from modern bioenergy, while a reduced amount derives from the use of solar thermal (0.7 EJ) and geothermal energy (0.3 EJ). In particular, solar thermal energy use for heat is growing rapidly in a number of countries: with 12% annual growth from 2000 to 2011, solar thermal energy is the fastest growing renewable energy source used for heat in the buildings sector.

Solar energy is the most abundant permanent energy resource on earth. One of the most popular low-temperature application of solar system is domestic water heating. Beyond the domestic applications, solar energy has several potential fields of application for low-temperature industrial processes. A wide range of collectors can be used for these low-temperature applications: flat plate, evacuated tube, compound parabolic, and more advanced types such as parabolic trough collectors (PTCs), which appear to be one of the most promising technologies to use the energy of solar radiation [4]. Low-temperature (or low-enthalpy) PTCs could provide thermal energy to domestic applications (e.g., domestic water heating, space heating, and cooling) and to industrial processes (e.g., pressurization, boiler feed-water, preheating water, pasteurization, cooking, etc.) at temperatures up to about 100 °C [5].

Among the application of solar thermal energy, solar cooking is considered as one of the simplest and attractive ways of the utilization of solar energy [6]. Energy for cooking is one of the fundamental uses in developing countries. Wood is still the primary energy source in much of the development world because of its cheapness; this situation is responsible for some serious ecological problems, especially deforestation. In most of rural areas of Africa, the energy demand for cooking is supplied by non-commercial fuels (e.g., firewood, agricultural waste, cow dung, kerosene); in India, the energy required for cooking accounts for 36% of total primary energy consumption and 90% of rural households depend on biomass fuels [7]. In addition to the environmental and economic issues, the firewood use also causes some serious health problems such as burns, eye disorders, and lung diseases.

However, considering that in most of the developing countries of the world there is abundance of solar radiation (a mean daily solar radiation of 5-7 $\mathrm{kWh/m^2}$ and more than 275 sunny days in a year have been estimated [8]), it is clear that solar cookers represent in such countries a possibility to meet the energy demand in the domestic sector. Other advantages of solar cookers are reduction of costs and drudgery, high nutritional value of food, and high durability. Unfortunately, the large-scale dissemination of solar cookers still remains limited; such devices are diffused all over the world, but most of them are intended for research purposes only [9]. The main obstacles to the dissemination of the technology are the resistance to acceptance as it is a new technology, variable nature of solar radiation, limited space availability in urban areas, and higher initial costs [10].

1.2 Solar Thermal Collectors

The principle usually followed in solar thermal energy collection is to expose a dark surface to solar radiation so that this one is absorbed. A fraction of this absorbed radiation is then transferred to a heat transfer fluid (HTF) such as water or air.

Solar collectors can be divided into stationary (or non-concentrating) and concentrating systems. The main difference between them is that the former have the same area for intercepting and absorbing solar radiation, while the latter generally have reflecting/refracting surfaces which intercept and focus the solar beam radiation to a smaller receiving area, thus resulting in an increased radiation flux.

Stationary collectors are permanently fixed in a certain position and are not able to follow the sun. Collectors which fall into this category are:

- flat plate collectors (FPCs);
- evacuated tube collectors (ETCs);
- solar air heaters.

When higher temperatures are required, solar radiation needs to be focused. This is achieved by using concentrating collectors. Solar radiation can be concentrated by interposing a reflecting arrangement of mirrors or a refracting arrangement of Fresnel lenses between the source of radiation and the absorber surface. The level of concentration is generally described by a quantity referred to as concentration ratio, C, which is defined as the ratio between the aperture area of the collector, A_a, and its receiver area, A_r:

$$C = \frac{A_\mathrm{a}}{A_\mathrm{r}} \tag{1.1}$$

The optical system which directs the solar radiation on to the absorber is defined concentrator, while the system including the absorber, its cover, and other accessories is defined receiver. The reflecting surfaces may be parabolic, spherical, or flat and continuous or segmented. Also, they can be classified according to the formation of the image, being either imaging or non-imaging. Imaging concentrators may focus on a line or at a point. The absorber can be convex, flat, or concave and it has a reduced area respect to that of the reflecting/refracting system. In addition, it can be uncovered or surrounded by a transparent cover.

The presence of the optical system compromises the overall performance by adding several inefficiencies:

- reflection losses;
- absorption losses;
- losses due to geometrical imperfections of the optical system.

However, the introduction of these inefficiencies is compensated for by the fact that the area from which heat losses occur (i.e., that of the absorber) is considerably reduced.

From an engineering point of view, concentrating collectors present additional problems to those of stationary collectors. In fact, because of the presence of the optical system, concentrating collectors have to be oriented to follow or track the sun in order to have the beam radiation directed on to the absorber surface. Different tracking methods are possible, and a proper choice depends on the precision with which it has to be done:

Table 1.1: Solar energy collectors (as reported by Kalogirou [5]).

Type	Tracking	Absorber	C	Temperature range (°C)
FPC	Stationary	Flat	1	$30 \div 80$
ETC	Stationary	Flat	1	$50 \div 200$
CPC	Stationary	Tubular	$1 \div 5$	$60 \div 240$
	One-axis	Tubular	$5 \div 15$	$60 \div 300$
PTC	One-axis	Tubular	$10 \div 80$	$50 \div 400$
LFR	One-axis	Tubular	$10 \div 40$	$60 \div 250$
PDR	Two-axis	Point	$600 \div 2000$	$100 \div 1500$
HFC	Two-axis	Point	$300 \div 1500$	$150 \div 2000$

- in collectors with a low concentration ratio, it is often adequate to manually make one or two adjustments of the collector orientation every day;
- in collectors with a high concentration ratio, a continuous adjustment of the collector orientation is necessary.

Tracking may be required around one or two axis. Obviously, the necessity of a tracking method introduces complexity in the design, and maintenance requirements are also increased; all these factors weight on the costs. In addition, the almost entirely part of diffuse radiation is lost being not focused. Compared to FPCs, there are few manufacturers of concentrating collectors all over the world, and the volume production is low [11].

A classification of solar collectors available on the market is provided in Table 1.1.

1.2.1 Flat Plate Collectors

Flat plate collectors (FPCs) are the most important and widely used type of solar collectors because they are simple in design, have no moving parts, and need little maintenance. From a mechanical point of view, they are much simpler than concentrating collectors and they can be used for applications where temperatures range from 40 to 100 °C [11].

A FPC using a liquid as HTF (Heat Transfer Fluid) is shown in Figure 1.1. The liquid heated is generally water, but sometimes mixtures of water and ethylene glycol are used if ambient temperatures below 0 °C are encountered. A FPC consists of four components:

- an absorber plate, usually made from a thin metal sheet;
- tubes fixed to the absorber plate through which the HTF flows, made of metal;
- a cover transparent to the incoming solar radiation and, at the same time, opaque to long wavelength radiation emitted by the absorber plate;
- a collector box, usually made of aluminum with an epoxy coating on the outside for protection.

Solar radiation falls on the absorber plate after crossing the transparent cover. The absorbed radiation is partially transferred to the liquid flowing through the tubes.

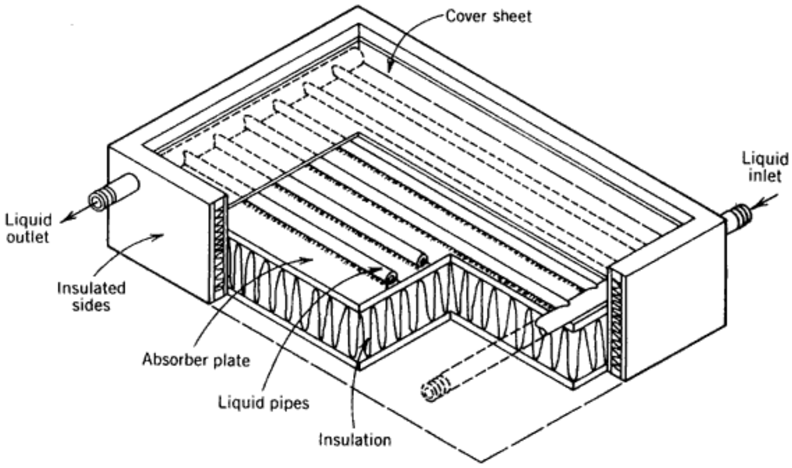

Figure 1.1: Schematic of a liquid flat plate collector (FPC) [12].

This heat transfer represents the useful gain. The remaining part of the radiation absorbed in the absorber plate is lost by convective and radiative heat transfers to the surroundings from the top surface, and by the conductive heat transfer through the back and the edges. The cover helps in reducing the losses by convection and radiation, while thermal insulation on the back and the edges, generally made with mineral wool, rock wool, or glass wool, allows to reduce the conductive loss.

A selective coating can be put on the absorber plate for reducing heat lost by radiation and improving the efficiency. To reach this goal, the selective coating must exhibit high absorptance in the range of solar spectrum and reduced emissivity in the range of mid/long infrared.

The main advantage of a FPC is that it utilizes both the beam and diffuse components of the solar radiation. On the other hand, its principal disadvantage is that the collection area is large because there is no optical concentration; therefore, the efficiency is generally low.

1.2.2 Evacuated Tube Collectors

Further enhancements in the efficiency of a FPC can be obtained by evacuating the volume between the absorber plate and the cover. In this way, the heat losses by convection from the top to the surroundings are reduced. Most practical designs are based on glass tubes because only a tubular surface can provide the structural strength to withstand the stresses introduced by the pressure difference.

A device with the above mentioned design is called ETC (Evacuated Tube Collector). It consists of a number of long cylindrical FPCs modules side-by-side. Each module is an evacuated, cylindrical glass tube containing a metal absorber plate with a selective coating. A U-tube heat removal system is attached to the absorber plate: an arrangement of this type is shown in Figure 1.2a. The incoming solar radiation is absorbed on this surface and partially transferred by conduction to the U-tube, then by convection to the HTF. A glass-to-metal seal is provided at the end cover of the glass tube.

The need of a seal, which is difficult to maintain, can be eliminated by adopting designs using all-glass double-walled evacuated tubes, as shown in Figure 1.2b. In this

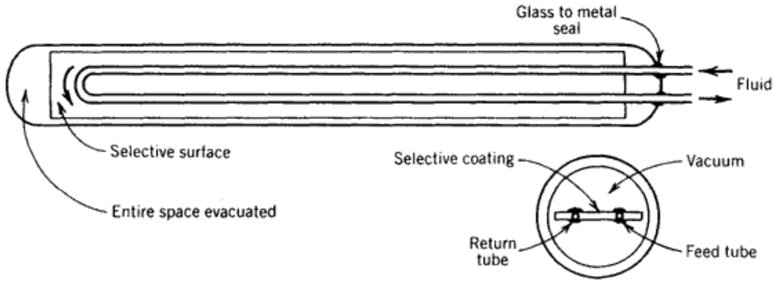

(a) Evacuated tube with U-tube removal system.

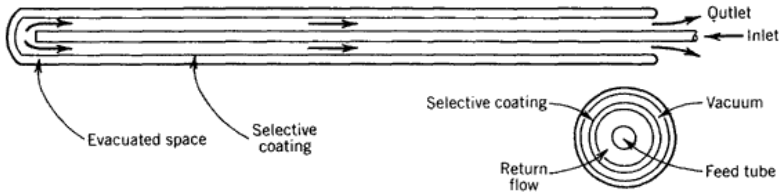

(b) Double-walled evacuated tube.

Figure 1.2: Designs of evacuated tube collectors (ETCs) [12].

case, each module consists of a long evacuated tube having the outer surface of the inner tube as the selective absorber. Other possible designs include the utilization of heat pipes. Thanks to the suppression of convective losses and the provision of a selective surface, ETCs can exhibit an efficiency significantly higher than that of conventional collectors.

1.2.3 Solar Air Heaters

A FPC used to heat air is referred to as solar air heater. The construction of this collector is similar to that of a liquid FPC, except for the passages where the air flows. In fact, these passages have to be made larger in order to keep the pressure drop across the collector limits. For this reason, a conventional solar air heater generally consists of an absorber plate with a parallel plate below forming a passage through which the air flows. A transparent cover is provided above the absorber plate, and a sheet metal container filled with insulation is provided on the bottom and sides. Materials of construction and sizes are similar to those adopted with FPCs. However, plastics are being used in increasing numbers [11].

Solar air heaters are simple in design and require little maintenance. Also, they can operate below 0 °C because air does not freeze, and corrosion and leakage problems are less severe. On the other hand, the convective heat transfer between the absorber plate and the air is low, thus a lower efficiency is obtained. To overcome this problem, surfaces are often roughened or longitudinal fins are provided in the air-flow passage. Another disadvantage is that large volumes of fluid are required, thus resulting in significant electrical inputs, especially if pressure drops are not kept within prescribed limits.

Compared to FPCs, commercialization of solar air heaters has been slow all over the world. According to Sukhatme and Nayak [11], in India the reason is the fact that these systems have been used primarily for forced convection drying of various kinds

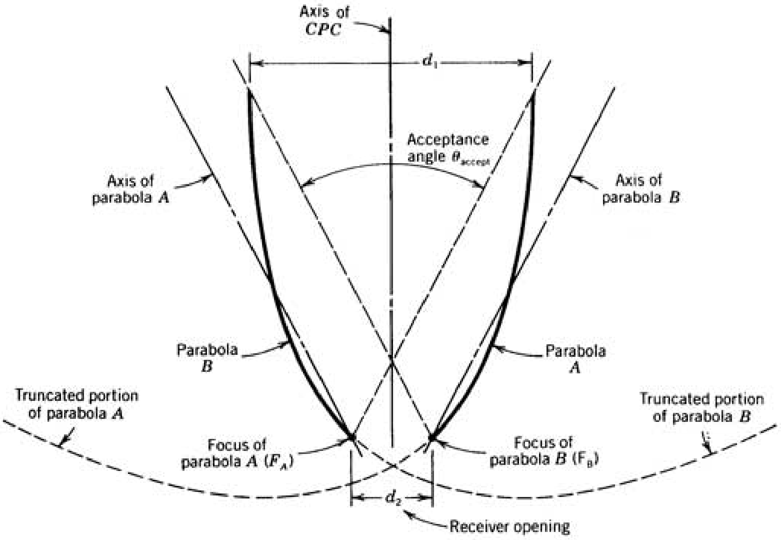

Figure 1.3: Cross-section of a compound parabolic collector (CPC) [12].

of agricultural products; being this one a seasonal activity, the drying systems remain idle for a large part of the year and the payback period is poor. A more attractive market for solar air heaters could be the utilization for industrial purposes and space heating.

1.2.4 Compound Parabolic Collectors

This non-imaging collector consists of curved segments facing each other that are parts of two parabolas (Figure 1.3). A compound parabolic collector (CPC) is capable to reflect to the absorber all the incident radiation within wide limits. In fact, the main advantage of CPCs is that they have high acceptance angles and require only occasional or intermittent tracking. By using multiple internal reflections, any radiation entering the collector acceptance angle reaches the absorber surface located at the bottom of the collector. The absorber can be flat, bi-facial, wedge, or cylindrical.

The concentration ratio is generally low, ranging from 3 to 10, and is equal to the maximum value possible for a given acceptance angle. CPCs can be manufactured either as one unit with one opening and one receiver or as a panel, in this case being similar to a FPC [5]. No significant commercial development has taken place [11].

1.2.5 Parabolic Trough Collectors

A schematic of a line-focusing concentrating collector, also referred to as PTC (Parabolic Trough Collector), is shown in Figure 1.4. This collector consists of:

- a concentrator, including the reflector and the support structure;
- a receiver, that includes the absorber tube located at the focal axis through which the HTF flows, and the transparent cover.

The reflector is a mirror having the shape of a cylindrical parabola, and it concentrates the beam radiation on to its focal axis, where it is absorbed on the absorber tube

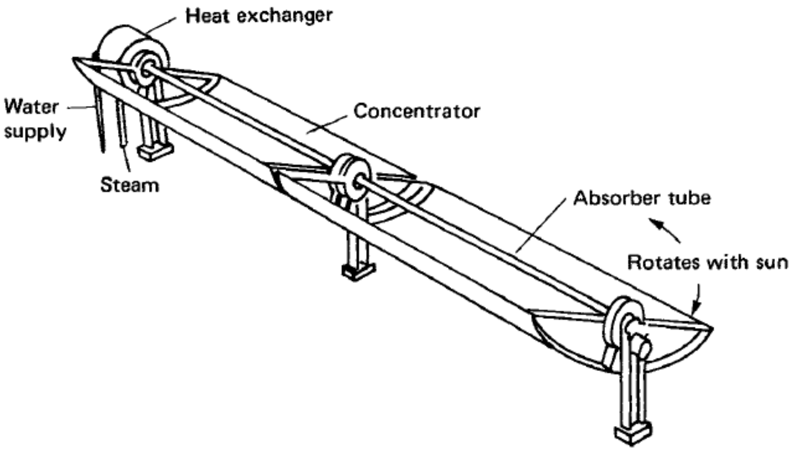

Figure 1.4: Schematic of a parabolic trough collector (PTC) [12].

surface and transferred to the fluid flowing through it. The concentrator must rotate about its axis to let the beam radiation to be focused on the absorber tube.

The reflective surface is generally made of a curved back silvered glass, fixed on a light-weight structure. The support structure should not distort significantly due to its own weight and it should be able to withstand wind loads.

The absorber tube is generally made of stainless steel, copper, or aluminum and has a diameter of 25 to 50 mm [11]. It is coated with a heat resistant black paint. The concentric glass cover has usually an annular gap of 10 or 20 mm and allows to reduce radiative and especially convective losses to the surroundings. To improve performances, the absorber tube can be coated with a selective paint and the annulus can be evacuated.

These collectors are available over a wide range of aperture areas from about 1 to 60 m^2, and widths from 1 to 6 m. Fluid temperatures between 50 and 400 °C, and concentration ratios ranging from 10 to 80 can be obtained [11].

1.2.6 Fresnel Collectors

Concentration may be also achieved by adopting lenses. One of the most common device is the Fresnel lens. Fresnel collectors have two variations, as shown in Figure 1.5:

- Fresnel lens collector (FLC, Figure 1.5a). It is usually a thin sheet, flat on one side and with fine longitudinal grooves on the other; these grooves are disposed so that radiation is brought to a line focus. The lens are generally made of extruded acrylic plastic sheets.
- Linear Fresnel reflector (LFR, Figure 1.5b). It is an array of linear mirror strips that concentrate the solar radiation onto a linear receiver. It can be imagined as a broken-up PTC, but the individual strips do not need to be of parabolic shape.

The strips of LFRs can also be mounted on ground and focus the solar radiation on a linear fixed receiver mounted on a tower. In this case, larger absorbers can be adopted. The greatest advantages of this arrangement are that reflectors are cheaper because they do not need to be parabolic and they can be mounted close to the ground, thus minimizing the structural requirements [5].

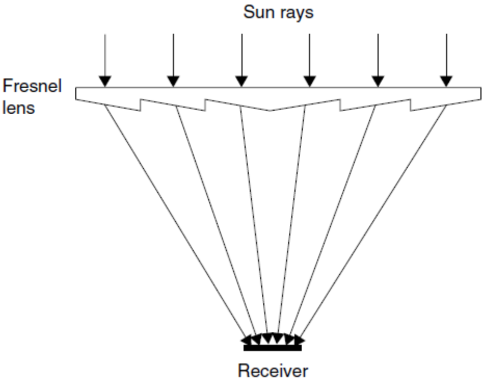

(a) Fresnel lens collector (FLC).

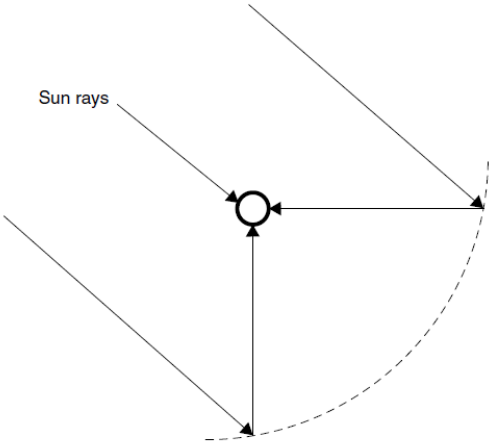

(b) Linear Fresnel reflector (LFR).

Figure 1.5: Fresnel collectors [5].

One difficulty with LFRs is that avoidance of shading and blocking between adjacent reflectors leads to an increased spacing between reflectors themselves. Blocking can be reduced by adopting higher absorber towers, but this increases costs. Fresnel collectors can achieve concentration ratios between 10 and 80, and yield temperatures between 150 and 400 °C [11].

1.2.7 Paraboloid Dish Reflectors

Still higher temperatures can be reached by adopting PDRs (Paraboloid Dish Reflectors), concentrating systems having a point focus rather than a focal line. Figure 1.6 shows the schematic of a PDR. This system has a concentrator that tracks the sun by rotating about two axes. Thus, the solar beam radiation is brought to a point focus, so that the sun is in line with the focus and the vertex of the paraboloid. A HTF flowing through a receiver at the focus is heated and this heat is typically used to drive a Stirling engine.

The receiver is an important component of PDRs. It is difficult to design because it has to receive a high heat flux (of the order of 10^6 W/m^2 and at about 700 °C), absorb

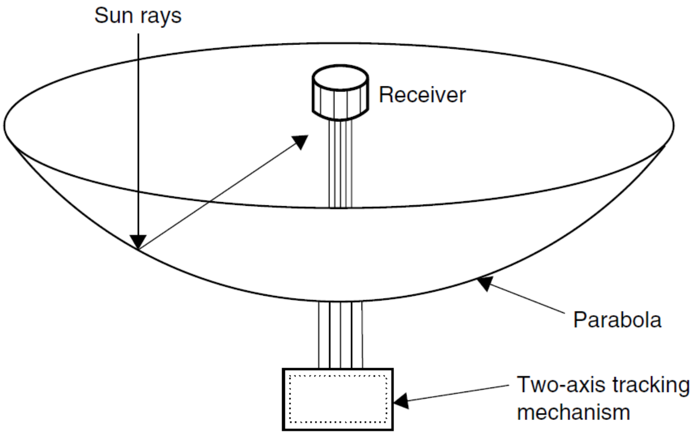

Figure 1.6: Schematic of a paraboloid dish reflector (PDR) [5].

it, and transfer the energy to the engine HTF. For all of these reasons, a number of new ideas have been tried out [11]:

- heat pipes using liquid metals like sodium, used to transfer the heat from the receiver to the engine head;
- hybrid receivers which can absorb both solar energy and energy from other sources (e.g., fossil fuel or bio-gas);
- volumetric receivers similar to those used in heliostat field collectors (see Section 1.2.8).

These collectors can have concentration ratios ranging from 100 to a few thousand, and yield temperatures up to 2000 °C [11]. However, there are limitations to the size of the concentrator and hence the amount of energy that can collected by one dish. Commercial versions have been built with dish diameters up to 17 m [11].

1.2.8 Heliostat Field Collectors

In order to collect larger amounts of energy at one point, HFCs (Heliostat Field Collectors) have been developed. In this type of concentrating collector (Figure 1.7), solar radiation reflected from an array of large mirrors called heliostats is focused on a receiver located at the top of a tower. The orientation of the heliostats is individually controlled so that throughout the day they reflect direct radiation on the receiver.

The heliostats form an array of circular arcs around the central tower. Their function is to intercept, reflect, and focus the solar radiation on the receiver. They are generally served by a two-axis tracking control system; when the solar radiation is not being collected, the control system orients the heliostats in a safe direction in order to protect the receiver. Degradation of the mirrored surfaces of the heliostats and low availability of the heliostats are major issues in the development of these collectors. Also, the costs of the heliostats and of their control systems form a significant part ($\simeq 40 \div 50\%$) of the initial investment. For these reasons, new concepts have been proposed, e.g. the utilization of larger size glass-mirrors, or heliostats using a stretched membrane ($\simeq$30% more cheaper than the glass-mirror design) [11].

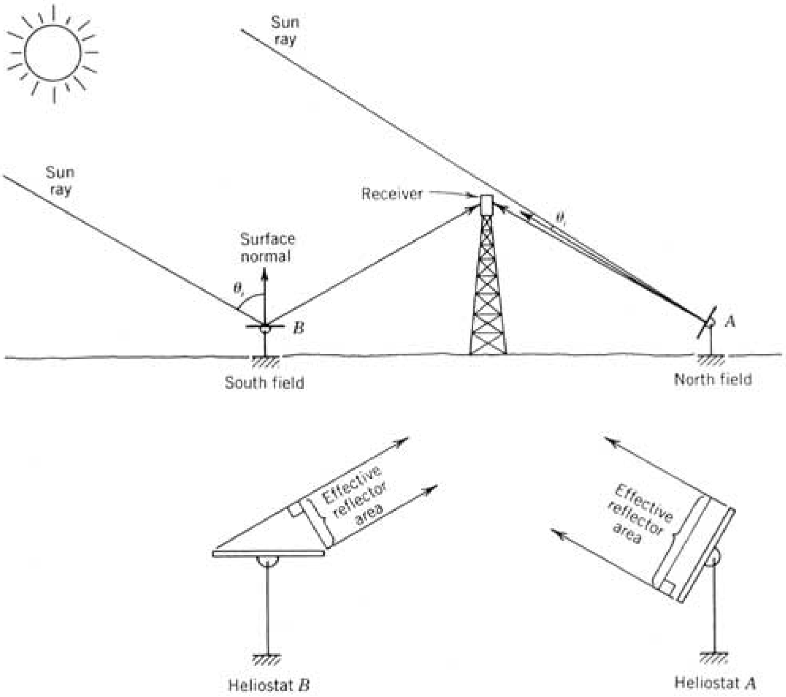

Figure 1.7: Heliostat field collectors (HFCs) [12].

The receiver is the most complex part of the system. The principal factor that influences its design consists of its ability to accept the large and variable heat flux that results from the solar concentration by the heliostats. The value of the heat flux can achieve 1000 kW/m^2, resulting in high temperatures, thermal gradients, and stresses in the receiver. For these reasons, the absorber shape, the HTF, the arrangement of tubes carrying the fluid, and the materials adopted need to be chosen with particular attention [11].

1.2.9 Solar Ponds

Devices that combine the functions of both solar energy collection and storage are called solar ponds. They consist of a large expanse of water of about 1 or 2 m in depth where salts like sodium or magnesium chloride are dissolved, in order to maintain a concentration gradient. These devices are referred to as salt-gradient solar ponds [11] and are shown in Figure 1.8. The concentration of the salt is more at the bottom and less at the top; in this way, the bottom layers of water are denser than the surface layers even if they are hotter, and free convection does not occur. Therefore, absorbed solar energy at the bottom of the pond is retained in the lower depths, and the upper layers of water act like a thermal insulation.

In the last 40 years, many salt-gradient solar ponds have been built in a number of countries, both for experimental and demonstrative purposes. The indications are that they would be economical for applications requiring low temperature processes up to 70 or 80 °C [11]. However, long-term operation and maintenance are problems of main concern.

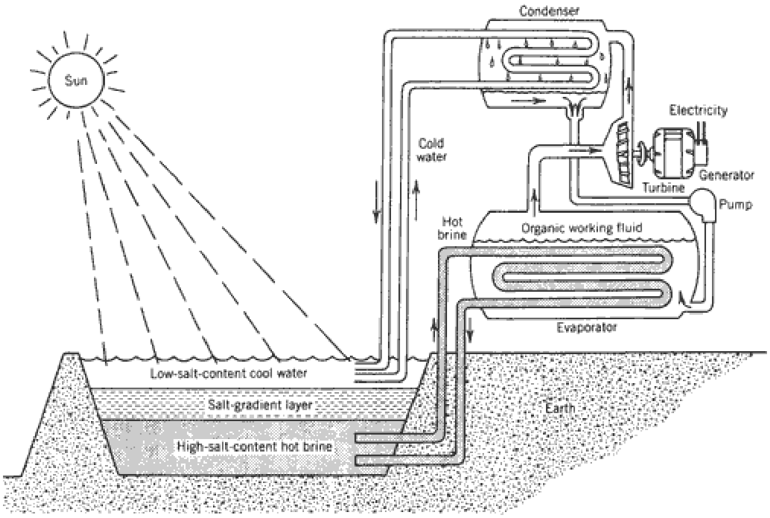

Figure 1.8: A salt-gradient solar pond [12].

1.3 Solar Cookers

Solar cookers (also called solar ovens) are devices able to cook food by utilizing solar energy. These devices can be used for processes such as pasteurization and sterilization, too. In the world, there are many arrangements of solar cookers and a comprehensive classification is not easy to be done. However, solar cookers can be broadly classified into two groups [10]:

- solar cookers without storage;
- solar cookers with storage.

Solar cookers without storage are categorized under direct and indirect solar cookers depending upon the involved heat transfer processes. Direct solar cookers use solar radiation directly in the cooking process, while indirect solar cookers use a working fluid to transfer the heat from the collector to the cooking device. As in indirect solar cookers the pot is physically displaced from the collector and flat plate collectors, evacuated tube collectors, and concentrating collectors are usually adopted to collect solar energy, this type of solar cookers will not be further analyzed in this thesis.

Instead, direct solar cookers are usually classified into the following two types [10]:

- box cookers;
- concentrating cookers.

Figure 1.9 summarizes the proposed classification of solar cookers.

1.3.1 Box Cookers

The first invented solar cooker was a box-type and was invented in 1767 by a French-Swiss naturalist called Horace de Saussure [6]. In the last decades, box cookers showed considerable developments in terms of design and performance.

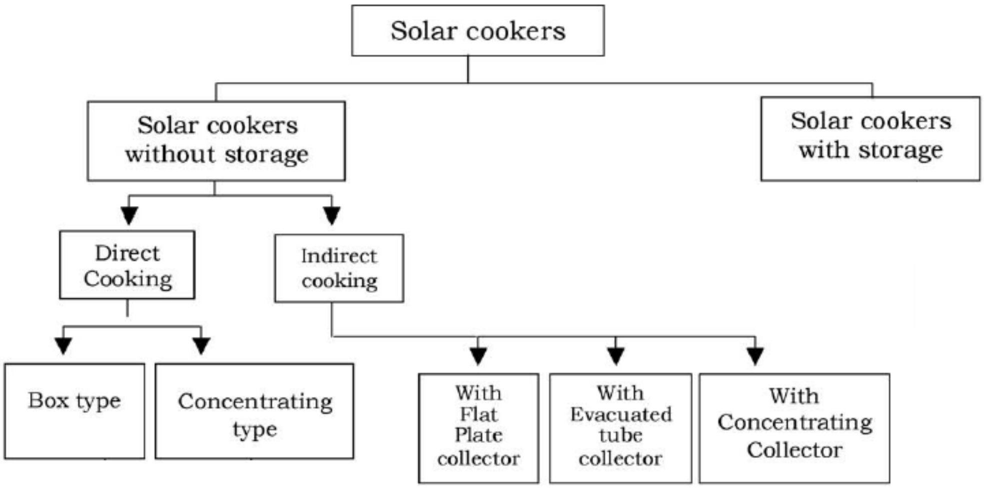

Figure 1.9: A classification of solar cookers. Adapted from Muthusivagami et al. [10].

A solar box cooker consists of an insulated box with a transparent glass cover and mirrors to reflect direct solar radiation into the box, as shown in Figure 1.10. The inner part of the box is usually painted in black in order to maximize the absorption of solar energy. Even if solar box cookers are slow to heat up, it was noted that they work well even with diffuse radiation, wind, intermittent cloud cover, and reduced ambient temperatures [13]. Additional advantages of box cookers include simplicity of manufacture and operation with minimal attendance required during the cooking process. This kind of cooker is also more stable and can keep food warm for a long period of time.

The payback period of a common solar box cooker, even if used 6–8 month a years, was found to be around 12–14 months [14]. Even with booster mirrors, solar box cookers have concentration ratios up to 10 and they rarely reach temperatures above 100 °C [10].

1.3.2 Concentrating Cookers

In concentrating solar cookers, the cooking vessel is placed at the focus of a concentrating mirror. These solar cookers can work with one or two axis tracking and can reach concentration ratios up to 50 and temperatures up to 300 °C. However, they have disadvantages such as size, cost, the risk of fires and burns, frequent adjustments to track the sun, and the impossibility to use thermal storage units for cooking during off-sunshine periods. Concentrating cookers include panel, funnel, spherical, parabolic, Fresnel, and cylindro-parabolic type [10].

Solar panel cookers are the most available type of solar cookers because of their ease of manufacture and low-cost materials [6]. They utilize reflective mirrors in order to direct solar rays to a cooking vessel which is enclosed in a clear plastic bag (Figure 1.11). Their reduced dimensions make them highly appreciated by people living or traveling alone. Performance of solar panel cookers strongly depends on reflected radiation, therefore they require clear-sky conditions to work properly; they are not very effective during cloudy days. Some solar panel cookers were also designed and

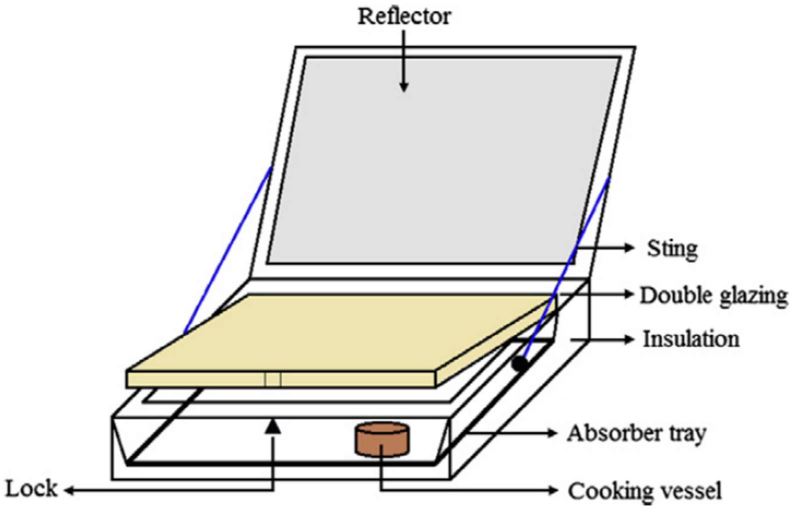

Figure 1.10: A solar box cooker [6].

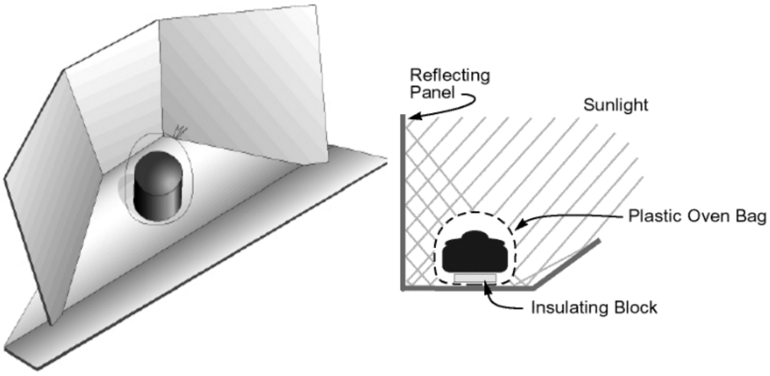

Figure 1.11: A solar panel cooker [16].

manufactured for sterilization purposes [15].

The first parabolic cooker was developed by Ghai and Bansal [17] in the early 1950s in India. This type of solar cooker can reach very high temperatures in a very short time and, unlike the panel and box cooker, they do not require a special cooking pot. A typical solar parabolic cooker (Figure 1.12) consists of a parabolic concentrator with a cooking pot located on the focus point of the cooker and a stand to support the cooking system [6]. Parabolic cookers are the most widespread type of concentrating cookers because the focus is much better and sharper than that of other types of reflectors, but at the same time they require constant tracking [10].

1.3.3 Other Direct Solar Cookers

In recent years, research focused on studying and manufacturing novel designs of solar cookers in order to provide better cooking efficiency [6].

In 1987 Khalifa et al. [18] carried out some tests on new design concentrating

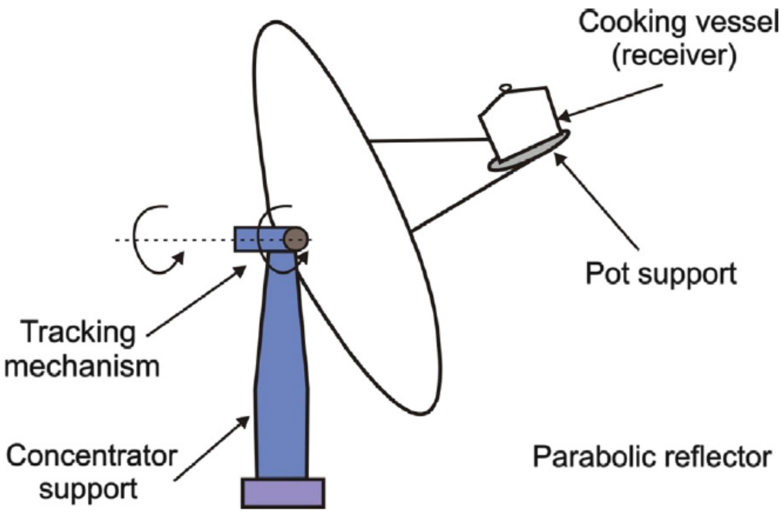

Figure 1.12: A solar parabolic cooker [9].

type solar cookers. Tiwari and Yadav [19] realized an alternative solar box cooker integrated with a single reflector at the cover and found that it was more efficient respect to a conventional cooker. In 1991, Al-Saad and Jubran [20] designed a low-cost solar cooker made of clay and locally available materials. No skilled labor was needed and the absorber plate was replaced with locally available black stones, which allowed energy storage and, thus, late cooking. Sonune and Philip [21] developed a Fresnel concentrating cooker where the highest plate bottom temperature was found to be 255 °C in approximately 40 minutes when ambient temperature and direct solar radiation were, respectively, 30 °C and 859 W/m^2. Kurt et al. [22] manufactured two different models of solar box cookers, rectangular and cylindrical, and tested the effects of the box geometry on the performance. They found that the cylindrical model provided higher thermal efficiency and lower characteristic boiling time than the rectangular type. Kumar et al. [23] designed and realized a truncated pyramid type solar cooker that did not require a solar tracking system; the maximum stagnation temperature was found to be 140 °C and water temperature inside the cooker reached 98.6 °C in 70 minutes. Abu-Malouh et al. [24] designed, manufactured, and tested a spherical type solar cooker coupled with an automatic sun tracking system; the temperature inside the cooker reached more than 93 °C in a day with a maximum ambient temperature of 32 °C.

1.3.4 Solar Cookers with Storage

When a mismatch between the supply and consumption of energy exists, thermal energy storage is necessary. In order to cook when there are frequent clouds in the day or during off-sunshine hours, solar cookers must adopt a heat storage material to store thermal energy in form of sensible heat, latent heat, thermo-chemical heat, or a combination of them [10].

In sensible heat storage, thermal energy is stored by raising the temperature of a solid or a liquid. For the purpose, researchers used engine oil [8], sand [25], and vegetable oil [26]. Limitations of sensible heat storage materials include low specific

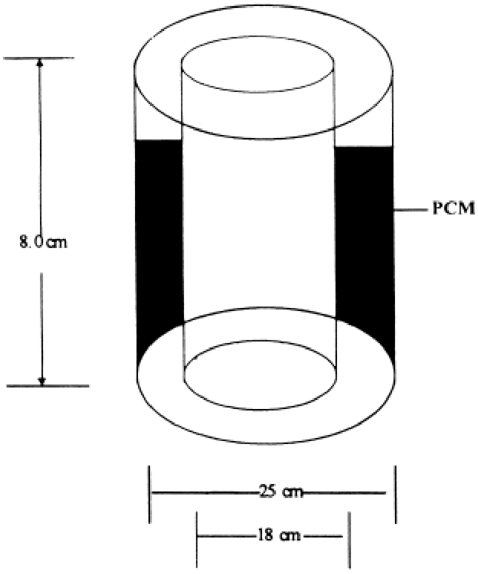

Figure 1.13: The latent heat storage unit designed by Sharma et al. [27].

heat capacity and the decrease in effectiveness of cooking since the temperature of the storage material decreases rapidly during discharging [10].

Latent heat storage uses the energy stored when a substance changes from one phase to another. The use of PCMs (Phase Change Materials) for storing latent heat has been recognized to be a compact and efficient way because of their high storage density and constant operating temperature [10]. Sharma et al. [27] designed and realized a PCM storage unit made of two hollow concentric aluminum cylinders of diameter 18 and 25 cm (Figure 1.13). The gap between the cylinders was filled with acetamide and the heat transfer rate between the PCM and the storage unit was enhanced by eight fins welded at the inner wall. They found that a second batch of food could be cooked if it was loaded before 15:30 and by using 2 kg of acetamide.

1.4 Solar Thermal Applications

Solar energy is used in a great number of thermal applications to meet various energetic needs. These are [11, 28]:

1. water heating;
2. space heating;
3. space cooling and refrigeration;
4. industrial process heat;
5. power generation;
6. distillation;
7. drying;

8. cooking.

Most of the above applications use one or more of the devices described in the previous sections. The applications 1, 2, 4, 6, 7, and 8 use thermal energy collected from solar radiation directly, while the applications 3 and 5 use the heat collected in thermodynamic cycles to obtain cooling or electrical work. From an economic point of view, applications that use heat directly are obviously more attractive [11].

1.4.1 Water Heating

Solar water heating is one of the most attractive solar thermal applications from an economic standpoint [11]. In many countries of the world, this technology is already competing on equal terms with systems using other energy sources. FPCs are the most adopted collectors for this kind of application [11]. Hot water is generally used for domestic, industrial, and commercial purposes.

Solar water-heating systems can be classified into two categories:

- natural circulation (or passive, or thermosyphon) systems;
- forced circulation (or active) systems.

The two main components of a natural circulation system are a liquid FPC and a storage tank. The last one is usually located above the collector level. As water in the collector is heated by solar radiation, it flows automatically to the top of the water tank and is replaced by cold water from the bottom of the tank. Hot water is withdrawn from the top of the tank. Natural circulation systems were used fairly widely in many countries from the beginning of the 20th century till about 1940 until cheap oil and natural gas became available. Today, passive systems are being installed again in large numbers [11].

Domestic water heating systems based on ETCs are also adopted. These systems consist of a number of evacuated tube modules connected directly to the storage tank. The inner part of each module is filled with water, which gets heated up by the solar radiation. A thermosyphon circulation is then established: hot water flows out of each module and cold water from the storage tank takes its place.

When a large amount of hot water is required to supply industrial or commercial heat demands, a forced circulation system maintained with a water pump is adopted. In this case, there is no necessity to put the storage tank at a higher level. Water from the storage tank is pumped through a collector array, where it is heated and then flows back into the storage tank. Solar water systems of this type are well suited for factories, hospitals, hotel, offices, etc. [11].

1.4.2 Space Heating

Space heating is of particular relevance in colder countries where a significant amount of energy is required for the purpose [11]. Heat for comfort in buildings can be provided by systems that are similar to water heating systems and can be distinguished into two types:

- active methods;
- passive methods.

Active methods use pumps or blowers to circulate the HTF in the space-heating system. On the other hand, with passive methods thermal energy flows through a living space by natural means without a mechanical device help.

The use of passive techniques for heating, as well as ventilation and cooling, is not new. They were adopted by almost all ancient civilizations [11]. However, passive methods are not used extensively because do not provide the same degree of comfort as an active heating system. But it is worth noting that nowadays, with rising fossil fuel costs, people are realizing the possibilities offered by passive methods and they are being slowly rediscovered [11]. In many new buildings, hybrid systems using both passive and active methods are being considered; in this way, the size of the active system is considerably reduced.

Compared to flat plate collectors, solar air heaters can be a logical choice for these applications, because they eliminate the need to transfer heat from one fluid to another.

1.4.3 Space Cooling and Refrigeration

Cooling is one of the most interesting thermal applications of solar energy as it can be adopted to provide comfortable living conditions or food preservation. Since solar energy is received as heat, an obvious choice is a system working on the absorption refrigeration cycle which requires most of its energy input as heat. Cooling is required most in summer, thus a seasonal matching between the energy needs of the space cooling system and the availability of solar radiation is generally satisfied.

Unfortunately, the installation cost of a solar absorption refrigeration system is high because of the cost of the large collector array required [11].

1.4.4 Industrial Process Heat

The most important application for solar energy at medium-high temperature ($80 \div 240\,°\mathrm{C}$) is heat production for industrial processes, which represents a significant amount of heat. Industrial heat demand constitutes about 15% of the overall demand of final energy requirements in the southern European countries [5]. The heat demand in the European Union for medium and medium-high temperatures is estimated to be about 300 TWh/year [29].

Several industrial sectors were identified as having favorable conditions for the application of solar energy [5, 28]:

- sterilizing;
- pasteurizing;
- drying of lumber or food;
- hydrolyzing;
- washing;
- cleaning in food processing;
- extraction operations in metallurgical or chemical processing;
- curing of masonry products;
- paint drying;

- polymerization.

Temperatures for these applications can range from near ambient to those of low-pressure steam. Energy can be provided both from FPCs (for low-temperature applications) and concentrating collectors (for medium-high temperatures). Industries which use most of the energy are food industry and manufacture of non-metallic mineral products. Favorable conditions exist in food industry because food treatment and storage are processes with high energy consumption and running time [5].

PTCs are frequently adopted for solar steam generation since relatively high temperatures can be obtained with good efficiencies. Low-temperature steam can be used in industrial applications, sterilization, and for powering desalination evaporators. Different methods were developed to generate steam by using PTCs [5].

Since solar energy is transient and intermittent, and investments in industrial processes are usually large, the choice of different arrangements in solar industrial applications can be done by using simulation methods at lower costs respect to the investments. In order to replace the utilization of large quantities of fossil fuels, solar energy for industrial process heat may represent an interesting alternative [28].

1.4.5 Power Generation

The generation of electrical power is one of the most important applications of solar energy [11]. Solar thermal power cycles can be classified as:

- low temperature cycles (<100 °C), using FPCs or solar ponds;
- medium temperature cycles (<400 °C), using PTCs;
- high temperature cycles (>400 °C), using either PDRs or HFCs.

Low temperature systems using FPCs generally work on a Rankine cycle. The overall efficiency of these systems are rather low, because the temperature difference between the steam leaving the generator and the condensed liquid leaving the condenser is small. In order to reduce costs, solar ponds have been used instead of FPCs. The first two solar pond power plants having capacities of respectively 6 and 150 kWe were constructed in Israel about 40 years ago. However, they proved to be not economically attractive being only less costly than plants using FPCs [11].

Solar thermal power plants operating with PTC technology at temperatures of about 400 °C have proved to be the most cost-effective and successful so far [11]. The first commercial plant of this type is SEGS I (Solar Electric Generating System), a power plant of 14 MWe based on PTCs. Since then, six plants of 30 MWe capacity (SEGS II to VII), followed by two plants of 80 MWe (SEGS VIII and IX), were commissioned and installed, for a total installed capacity of 354 MWe. The installed cost of this kind of plant has reduced over the years because of the increasing installed capacity, but it is still very high (e.g., SEGS VII is reported to have cost 4000 USD per kWe [11]). However, SEGS I-IX have continued to operate and a valuable operating experience extending to more than twenty years has been obtained.

Because of the limitations on the size of the concentrator, PDRs can generate only moderate power (of the order of kilowatts). Two important issues for commercializing PDRs with Stirling engines are cost and reliability. Respect to the former, presently installation costs are very high ($\simeq$ 10 000 USD per kWe); however, it is estimated that the cost of a system could reduce to 2500 USD/kWe if the yearly production improves [11]. In HFCs, a HTF flowing through the receiver absorbs the incident radiation and transports the heat to the ground where it is used in a Rankine or a Brayton cycle. Molten salts, water, and air have been used as HTFs. Of all the plants built in eighties, the largest (10 MWe) was Solar One, built in 1982 at Barstow, California. The plant was operated for six years from 1982 to 1988 and its feasibility was successfully demonstrated. However, in order to overcome the problems encountered with Solar One, some modifications were made: molten salts were used as HTF instead of water/steam so that only single phase liquid flow occurred in the tubes of the receiver. Also, a new molten salt thermal storage system with a larger capacity was installed and 108 heliostats were added. This modified plant was called Solar Two. The project began operative in 1996 and was run for three years, demonstrating the potential of molten salt technology.

It has been recognized that solar thermal energy can make a real impact if it leads to a large scale cost-effective electrical power generation [11]. Medium temperature systems using PTC technology have been commercialized to some extent. In addition, HFCs have been tested extensively on a pilot scale. Both systems seem promising, but need a considerable amount of developmental work before their suitability and feasibility can be assessed [11].

1.4.6 Distillation

The natural supply of fresh water is inadequate respect to the availability of brackish or saline water in many small communities of the world [11]. Solar distillation could be an effective way of supplying drinking water to such communities.

A detailed discussion of the principles of solar distillation is beyond the purposes of the present work. However, it has to be noted that an output of about $3\,\mathrm{l/m^2}$ with an associated efficiency of 30 to 35% can be obtained in a well-designed conventional basin-type solar still on a good sunny day [11]. A number of basin-type solar still plants having areas greater than $100\,\mathrm{m^2}$ are operative in many parts of Africa and West Indies [11].

1.4.7 Drying

Drying of agricultural products is one of the traditional uses of solar energy [11]. The drying process helps in removing moisture and preserving products. Traditionally, drying is done on open ground. The disadvantages associated with this are that the process is slow and that insects and dust get mixed with the product. The use of dryers helps to eliminate these disadvantages; in addition, drying can be done faster and a better quality for the product is obtained.

1.4.8 Cooking

The energy demand for cooking in developing countries is an important portion of the global energy consumption. For example, in India about the 50% of thermal energy is used only for cooking, and a large fraction of this demand is satisfied by non-renewable sources such as wood, kerosene, and liquefied petroleum gas [6]. Therefore, many developing countries find an attractive opportunity in using solar cookers with the aim of cooking different types of food.

Chapter 2

Parabolic Trough Collector Prototype: Testing and Characterization

The manufacture of novel parabolic trough collectors (PTCs) for industrial process heat applications ranging from $70 \div 250\,^{\circ}\mathrm{C}$ is crucial for the widespread availability of this solar technology. Thus, a prototype of a PTC with a 90° rim angle and a concentration ratio of 19.89, called UNIVPM.02, was designed and manufactured. Gel coat was used as the external shell, while fiberglass and low density polyvinyl chloride (PVC) as the inside fill components. The receiver is a pipe of circular cross-section made of steel. The tracking system is based on a solar-position computer program. First, the design and manufacturing processes are presented. Then, the test bench used to evaluate the collector thermal efficiency is shown. Tests were performed following the directives of ANSI/ASHRAE Standard 93-2010 and using demineralized water for temperatures up to $85\,^{\circ}\mathrm{C}$. Results show that the equation for thermal efficiency is comparable to that of other similar collectors available in literature.

2.1 PTC Prototypes in Literature

The development of low-cost PTCs plays a decisive role in the spread of this technology. This objective can be reached only by studying and testing profoundly innovative prototype designs. For this reason, a research program called PTC.project was started at the Department of Industrial Engineering and Mathematical Sciences (DIISM) of Marche Polytechnic University (UNIVPM) regarding the development of PTCs for industrial heat production in the range of $70 \div 250\,^{\circ}\mathrm{C}$.

The systematic study of PTC design began several decades ago. In his paper of 1976, Treadwell [30] considered how optical and thermal effects influence the efficiency of a PTC. He found that rim angles of 90° minimize the maximum distance between the parabolic reflector and the focus. Since the receiver diameter is proportional to this distance, thermal losses, which are proportional to the diameter itself, are reduced.

In a detailed work published in 1992, Thomas and Guven [31] outlined the main structural design requirements for a PTC. A PTC should: a) provide and maintain the correct optical shape of the reflective surfaces; b) maintain its shape within the specified tolerances during operations; c) protect the reflective surfaces under extreme weather conditions; d) withstand long-term environmental exposure. In other words, the stresses and deflections experienced by the receiver and the reflector must remain below specified levels under gravitational, wind, and thermal loads. On the other hand, the choice of materials depends on environmental stability, durability, mechanical and physical properties, suitability of the construction method, fitness for high production rates, low total weight, and cost. The authors also state that a sandwich structure is a good design, but high precision molds are required in order to successfully fabricate high quality PTCs.

In 1994, Kalogirou et al. [32] presented a PTC design with high stiffness-to-weight ratio and a low-labor manufacturing process. The structure is made of polyester resin and woven fiberglass cloth, with plastic conduits that provide reinforcement. In a paper published the same year [33], the authors outlined an optimization of the design based on three parameters: a) collector aperture; b) rim angle; c) receiver diameter. They also proposed a tracking mechanism with a control system consisting of three light-dependent resistors.

The EUROTROUGH project [34] carried out in 2001 proposed a torque box design with lower weight and less collector deformation than other designs. This technology presents different advantages: a) the possibility of connecting more collector elements on one drive, so that their number, in addition to costs and thermal losses, is reduced; b) reducing the torsion and bending increases the optical performance and wind resistance. A torque box structure was also used by Brooks et al. [35] with a mix of advanced and less sophisticated technologies to manufacture a reflector made of stainless steel sheets covered with aluminized acrylic film. This solution grants accessibility, accuracy, ease of fabrication, and cost reduction.

ENEA (Italian National Agency for New Technologies, Energy and Sustainable Economic Development) investigated almost every aspect related to PTCs, and designed and realized several PTC prototypes. As concerns structural aspects, different studies were carried out [36–38].

In 2007, Valan Arasu and Sornakumar [39] presented a simple, low-cost hand lay-up method for manufacturing PTCs based on the previous work of Kalogirou et al. [32]. The design proposed consists of a smooth 90° rim angle, reinforced parabolic trough made of layers of polyester resin and chopped strand fiberglass.

In 2011, Rosado Hau and Escalante Soberanis [40] illustrated the production of a water-heating system based on PTC technology limited to a maximum temperature of 55 °C. The collector presented uses a sheet of polished stainless steel. The receiver is a copper tube coated with a thin black paint, and shielded by a polycarbonate glass; it is not evacuated.

In their work of 2012, Venegas-Reyes et al. [41] described a light but robust structure of aluminum made only using hand tools. This PTC has a rim angle of 45° and, since it is designed for low-enthalpy steam generation and hot water, it presents an unshielded receiver without a glass cover in order to reduce costs. In another work published in 2013 [42], the authors presented five PTCs for the same purpose; three of them have a rim angle of 90° and the other two have a rim angle of 45°.

In 2011, a small PTC prototype called UNIVPM.01 was designed, manufactured, and tested at DIISM [43]. This prototype had a 90° rim angle and a concentration ratio of 9.25. The main feature of UNIVPM.01 was the parabolic support structure: it was a composite of fiberglass (used as an external shell) and extruded polystyrene (XPS, as inside fill component). These two materials were chosen for different reasons: a) cost; b) weight; c) resistance to atmospheric agents; d) ease of manufacturing. This solution was preferred to the simple fiberglass structure because it offered high

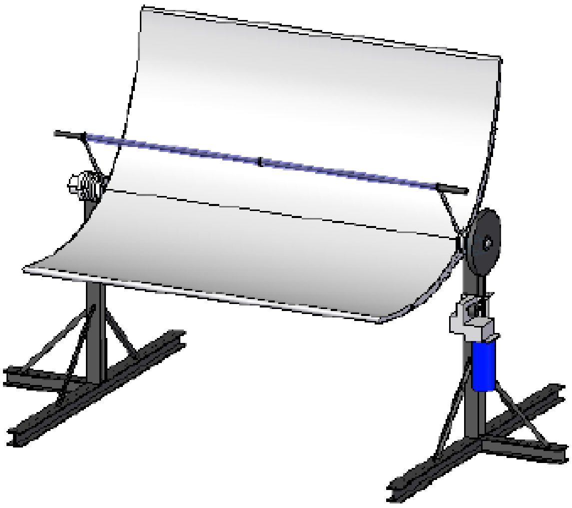

Figure 2.1: UNIVPM.02 PTC prototype [44].

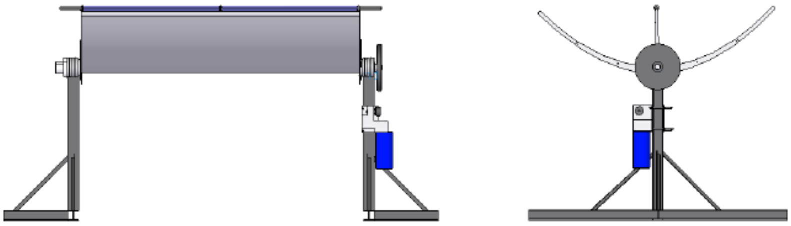

Figure 2.2: UNIVPM.02: 2D drawings [44].

structural performances and low weight. Experimental tests showed a performance similar to other PTCs reported in literature.

2.2 Design and Manufacture

UNIVPM.01 was intentionally kept small in size in order to have ease of manufacture and to test the realization process. Starting from the experience gathered, a second PTC was designed and manufactured: UNIVPM.02 (Figure 2.1, 2.2, and 2.3).

The structural concept of UNIVPM.02 was kept the same as the previous prototype (sandwich composite), as it has proven to be an excellent solution in terms of stiffness, weight, and cost. UNIVPM.02 is about twice the size of the previous prototype and a different material was used for the matrix: low density polyvinyl chloride (PVC) instead of XPS. PVC is widely used in naval industry as a matrix for sandwiches thanks to its mechanical strength and also to the many different densities, thicknesses, and geometries that are commercially available.

In addition, UNIVPM.02 was realized with a gel-coat superficial coating, so that it could better withstand atmospheric agents. The rim angle was kept equal to 90°, in order to minimize slope and tracking errors [5, 30]. To improve the fiberglass manufacture, the hand lay-up method used for the UNIVPM.01 concentrator was replaced with a VARTM (Vacuum Assisted Resin Transfer Molding) technique.

Figure 2.3: A picture of UNIVPM.02.

2.2.1 Mold

The parabolic concentrator of UNIVPM.02 is a sandwich-structured composite including gel coat, fiberglass, and PVC. Generally, manufacturing processes used to realize fiberglass composites require the use of a mold. Two molding techniques can be used to obtain the final fiberglass structure in the desired shape: open or closed molding methods. In the former, the mold bounds the composite layers from just one side, while in the latter the composite layers are completely bounded [45].

The simplest and oldest molding method is open molding, which is used for both small and large fiberglass parts. The mold can be a flat surface or a cavity (called male surface) and is usually made of wood, metal, or plastic. The only requirement is that the surface must have the shape to be obtained in the final piece. Once the mold is prepared, the fibers are placed against the mold surface, along with the resin, using a hand lay-up (Figure 2.4) or a spray-up method. The thickness of the composite is controlled by the number of layers placed against the mold. An open molding technique was used to realize the first PTC prototype, UNIVPM.01 [43].

Closed molding can be classified into different methods: injection molding, compression molding, resin transfer molding, etc. In the case of injection or compression molding, both a male and female mold are required. Therefore, these methods are not appropriate for prototyping purposes. In this case, a vacuum assisted resin transfer molding (VARTM) is a more appropriate method, as it can be adopted with just a male or a female mold; in addition, it is cost-effective for low and medium volume applications [44]. In VARTM processes, the mold can be made of aluminum or steel, but plastic or wood are also used for low production volumes. The mold must be hermetic to air and have appropriate mechanical properties in order to withstand the loads induced by the low pressure on the surfaces (Figure 2.5). The main advantages of

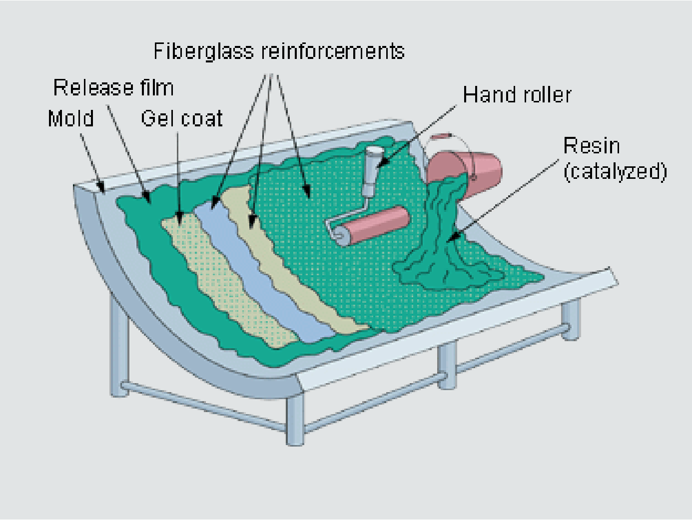

Figure 2.4: Hand lay-up technique used in open molding [46].

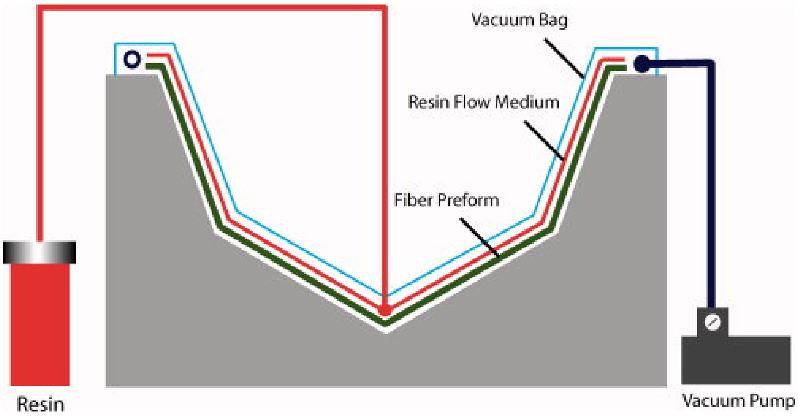

Figure 2.5: VARTM method [47].

VARTM respect to the hand lay-up method are the possibility to control the quantity of resin and the speed of the process; also, it generally guarantees better mechanical qualities and surface finishes. However, VARTM requires experienced personnel and some equipment and accessories which are not required by the hand lay-up method.

Taking into account the advantages offered by the VARTM technique, this method was finally chosen to realize the UNIVPM.02 concentrator. The mold cutaway used for the manufacture is shown in Figure 2.6. The parabolic frame consisted of 13, 15 mm thick, PVC ribs. Each rib presented two rectangular cuts on its lower part which allow some room for four longitudinal steel L-profiles, 2 mm thick, used as reinforcement. The PVC ribs and L-profiles were connected each other by means of screws and their lower surfaces were screwed to a wood floor 12 mm thick. Two AISI 304 steel sheets, 0.8 mm thick, were placed upon the parabolic surface created by the ribs, representing the area on which the fiberglass layers were laid. The two sheets were placed side by side and held in position by two longitudinal aluminum bars which were screwed to the PVC ribs.

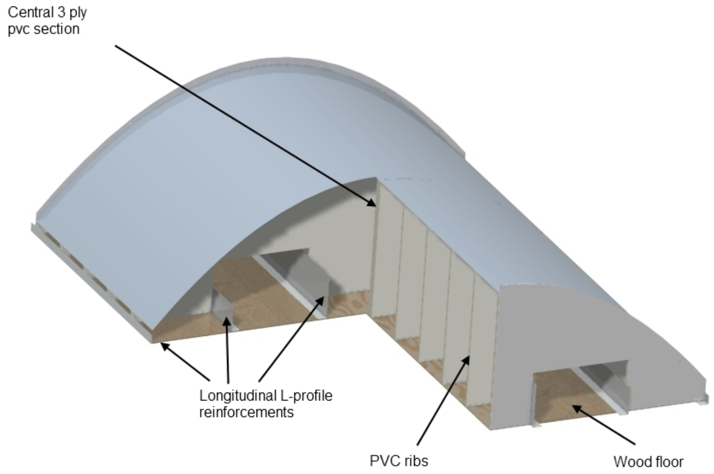

Figure 2.6: Mold cutaway [48].

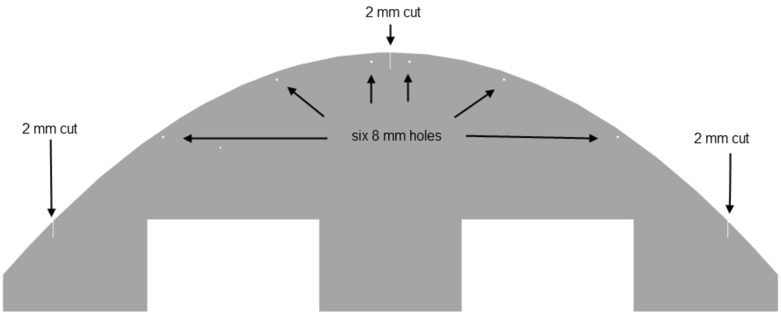

Figure 2.7: Mold aluminum end plates [48].

Since no single steel sheet was found with the required dimensions, the gap between the two AISI sheets was carefully sealed. In fact, the VARTM process requires a tight seal around the vacuum bag in order to run properly. Hence, a central 3 ply PVC rib section was arranged, as reported in Figure 2.6. The result is a 15 mm wide and 3 mm deep channel, running the length of the 3 ply assembly. Before fixing the two steel sheets on the frame, this channel was filled with a silicon high-temperature resistant sealant, which filled the gap between the mounted sheets and provided a tight seal.

Two 5 mm thick aluminum plates were fixed at the mold ends (Figure 2.7). These plates are 50 mm higher than the PVC ribs and include some cuts and holes required in the VARTM process. The six holes on the end plates are reference points for the placing of six small brass plates which were embedded on the side surfaces of the infused concentrator frame.

The fiberglass final frame had a parabolic surface smaller than the one available, as a Teflon rim placed along the borders of the steel surface was needed to seal the vacuum bag before the VARTM process. The effective surface of the final fiberglass structure is visible in Figure 2.8, while the characteristics of the mold are reported in Table 2.1. The final dimensions and weight of the mold are relevant matters to be

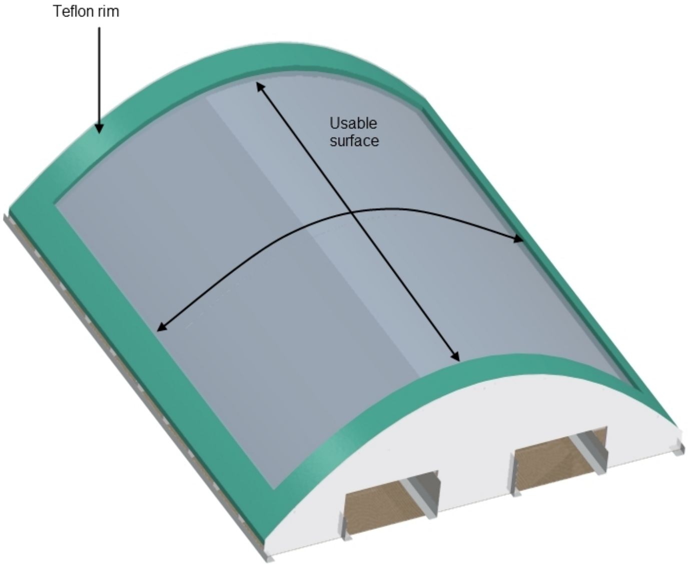

Figure 2.8: Effective surface of the final fiberglass structure [48].

Table 2.1: Characteristics of the UNIVPM.02 mold.

Characteristic	Value
Length (m)	3.100
Width (m)	2.524
Height (m)	0.860
Parabolic profile length (m)	3.000
Parabolic surface (m^2)	$\simeq 9$
Weight (kg)	$\simeq 250$

considered as they can be problematic if operations are carried out in a laboratory environment [44].

2.2.2 Concentrator

The UNIVPM.02 concentrator is a structure based on a sandwich composite system. Composite materials have two or more constituent materials or phases of significantly different physical properties; thus, the composite properties are quite different from the constituent properties. Generally, the component having harder and stronger properties is called reinforcement material, whereas the other component is referred to as matrix. Fiber-based reinforced materials are the most widespread kind of composite materials and contribute to enhance mechanical qualities. Among all fiber-based reinforced materials, fiberglass is a fiber reinforced polymer obtained with a plastic matrix and fine fibers of glass. The matrix, instead, can be a thermosetting plastic, a thermoplastic polymer, or an epoxy resin, and binds the fibers together protecting them against aggressive environmental conditions. Evidently, the characteristics of the final material depend upon the characteristics of the fibers and the characteristics of the matrix.

Among composite materials, the field of sandwich-structured composites includes

Table 2.2: Layers used in the UNIVPM.02 concentrator structure.

Layer	Material
1	Gel-coat
2	Mat 300
3	Mat 300
4	Biaxial 1200
5	Low density PVC
6	Biaxial 1200

products that are fabricated attaching two thin skins to a thick lightweight core. The former are stiff materials, while the latter is a low strength component. The core is often made of open and closed-cell-structured foams of honeycombs. Instead, the skins are usually laminates of glass or carbon fiber reinforced thermoplastics or polymers; in some cases, metal sheets are used, too.

The layers adopted for the UNIVPM.02 concentrator are reported in Table 2.2. In particular, mat 300 is a fiberglass layer, while biaxal 1200 is a non-woven fabric with 0–90° fiber orientation and polyester stitchings (Figure 2.9). The molding procedure was realized according to the following steps [44]:

1. application of wax paste;
2. gel-coating;
3. deposition of all the following layers;
4. collocation of the peel-ply and of the diffusion layer;
5. positioning of the Enka channels and of the inlet ports;
6. positioning of the vacuum tube and of the outlet ports;
7. sealing of the vacuum bag;
8. infusion;
9. extraction of the laminate.

Further information about the molding process can be found in Sotte [44]. Once dry, the structure was removed from the mold and a highly reflective aluminum foil (MIRO-SUN Weatherproof Reflective 90 [49]) was glued to the concave surface to create a parabolic reflective surface. The reflective foil consists of anodized aluminum with a specially coated surface on one side studied for outdoor solar applications that require high reflectance and resistance to atmospheric agents.

The main characteristics of the UNIVPM.02 concentrator are summarized in Table 2.3.

2.2.3 Receiver

The receiver used in the UNIVPM.02 prototype has the geometrical and thermal/optical properties reported in Table 2.4. It is a steel pipe of circular cross-section: the outer surface is painted with a black selective coating. Unlike the first PTC prototype, the UNIVPM.02 receiver is not shielded. This choice was driven by two reasons:

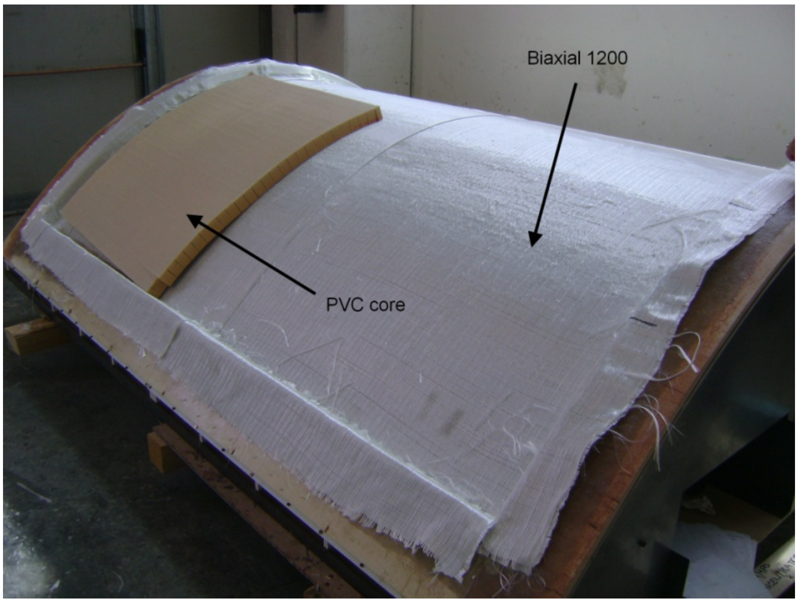

Figure 2.9: Concentrator layers [48].

Table 2.3: Characteristics of the UNIVPM.02 concentrator.

Characteristic	Symbol	Value
Focal length (m)		0.550
Mirror length (m)	L_{m}	2.570
Mirror aperture (m)		2.500
Aperture area (m^2)	A_{a}	6.425
Rim angle (°)	ϕ_{r}	90
Foil normal specular reflectance	ρ_{n}	0.94
Weight (kg)		180

- reduction of costs and design simplification;
- improvement of optical efficiency.

However, the absence of the cover worsens the thermal insulation respect to the surroundings. This effect is particularly relevant for PTCs working at high temperatures, especially because radiative losses predominate. In low-enthalpy PTCs, where temperature ranges are limited to 100 °C, the cover can be omitted [35, 41, 42].

Taking into account the geometrical dimensions of the receiver, the concentration ratio C, i.e. the ratio between the aperture area of the collector A_{a} and the absorber outer surface area A_{r}, is [28]:

$$C = \frac{A_{\mathrm{a}}}{A_{\mathrm{r}}} = 19.89 \tag{2.1}$$

2.2.4 Tracking System

The tracking system is composed of five elements:

Table 2.4: Characteristics of the UNIVPM.02 receiver.

Characteristic	Symbol	Value
Inner absorber diameter (m)	D_{ai}	0.035
Outer absorber diameter (m)	D_{ao}	0.040
Length (m)	L_{r}	2.570
Absorber outer surface area (m^2)	A_{r}	0.32
Absorber th. conductivity (W/(m K))	λ_{a}	60
Coating normal absorptance	α_{n}	0.95
Coating emissivity	ϵ_{a}	0.30

1. an asynchronous three-phase motor (0.18 kW power, 900 RPM speed) with 6 poles;
2. an inverter that allows the motor speed to be regulated;
3. three worm drives with gear ratios of 1/60, 1/60, and 1/35;
4. a belt drive with a transmission ratio of approximately 1/5 that couples the last worm gear to the PTC axis;
5. a 5000 position-per-revolution encoder, coupled to the rotation axis of the collector.

A picture representing the motor, the worm drives, and the drive belt is shown in Figure 2.10. The motor was attached to the support structure via four bolts and two plates. This allowed to regulate the height of the motor respect to the ground and to set the correct tension of the belt drive. The presence of the worm drives was necessary in order to reduce the maximum rotational speed of the collector: in fact, the motor was too fast and the transmission ratio of the belt drive too small to guarantee a correct tracking of the sun. The belt drive also acts as a clutch to prevent torques that are too high from being transmitted from the PTC to the tracking system.

The use of a common industrial asynchronous motor and a gear reduction system is a solution that can easily be scaled up. The idea is to rotate an entire line with just one motor; thus, it is necessary to adopt a solution that can be adapted to produce a large torque on the final axis. Other solutions, such as stepper motors, are easier to adapt to smaller systems but become very expensive when a relevant torque has to be produced. In addition, the non-reversibility of motion in worm drives is an advantage because it allows the system to be kept in position without powering the motor.

The encoder and the inverter communicate with a PC through appropriate electronics. A diagram of the electronic signals is shown in Figure 2.11. A solar-position routine based on Michalsky's algorithm [50] was implemented in LabVIEW to calculate the correct rotational speed to be given to the PTC at any instant. The date and time inputs are imported into LabVIEW from the PC operative system. The routine elaborates the desired position for the collector, β, with a time-step of one second.

The tracking system is able to follow the sun with the PTC oriented in two different directions. When the PTC axis has a EW (east–west) orientation, the desired position is [28]:

$$\tan\beta = \tan\theta_{\mathrm{z}}|\cos\gamma_{\mathrm{s}}| \tag{2.2}$$

Figure 2.10: A picture of the motor, worm drives, and drive belt used in the tracking system.

Instead, when the PTC axis has a NS (north–south) orientation, the desired position is given by [28]:

$$\tan\beta = \tan\theta_{\mathrm{z}}|\cos(\gamma_{\mathrm{PTC}} - \gamma_{\mathrm{s}})| \tag{2.3}$$

In Equation (2.2) and (2.3), θ_{z} is the zenith angle, γ_{s} is the solar azimuth angle, and γ_{PTC} is the PTC axis azimuth angle.

At the instant t, the correct value for the angular speed to track the sun, ω, is:

$$\omega = \frac{\beta_{t+\Delta t} - \beta_t}{\Delta t} \tag{2.4}$$

where $\Delta t = 1\,\mathrm{s}$. The angular speed ω has a minimum equal to 4.7×10^{-5} rad/s and a maximum equal to 1.7×10^{-4} rad/s throughout a year: for a PTC axis with NS orientation and situated in Ancona, Italy (latitude 43.5867 N, longitude 13.5150 E), the minimum and the maximum speed occur, respectively, during the sunrise (or sunset) of summer solstice and during the solar noon of winter solstice. The rotational speed of the collector can be adjusted at the minimum and maximum speed via the inverter: in particular, when the inverter frequency is set to 5 Hz, the minimum speed is obtained. Alternatively, when a frequency of 100 Hz is set, the PTC axis rotates at the maximum speed. All these settings were automatized in the solar-position routine.

The proposed tracking mechanism would be correct only for an ideal collector that was always in focus. In reality, the collector can be misaligned during normal working conditions, or at the start. Thus, for each time step the calculated value of β is used

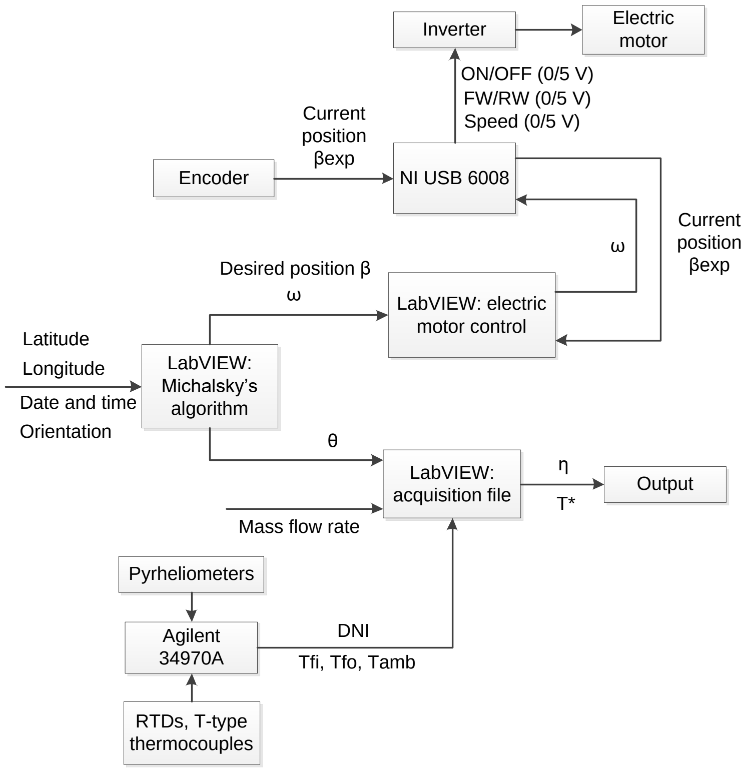

Figure 2.11: Data flow schematic of the electronic signals.

as input for the motor control system: this compares the desired position, β, with the current position read on the encoder, β_{exp}. If we introduce a tolerance position error equal to the resolution of the encoder:

$$\Delta\beta = \frac{360}{5000} = 0.072^{\circ} \tag{2.5}$$

three cases are possible (see the flow chart in Figure 2.12):

- if $\beta < \beta_{\text{exp}} - \Delta\beta$, the motor is slowed down to the minimum speed in order to regain focus;
- if $\beta < |\beta_{\text{exp}} - \Delta\beta|$, the collector is in focus and the tracking mechanism previously described is adopted;
- if $\beta > \beta_{\text{exp}} + \Delta\beta$, then the motor is accelerated to the maximum speed to regain focus.

In addition, the LabVIEW environment allows to manually: a) turn on and off the motor; b) set the appropriate degree of rotation; c) give a user-defined rotational speed. A soft start was also included in the inverter to avoid damage to the motor or to the gears.

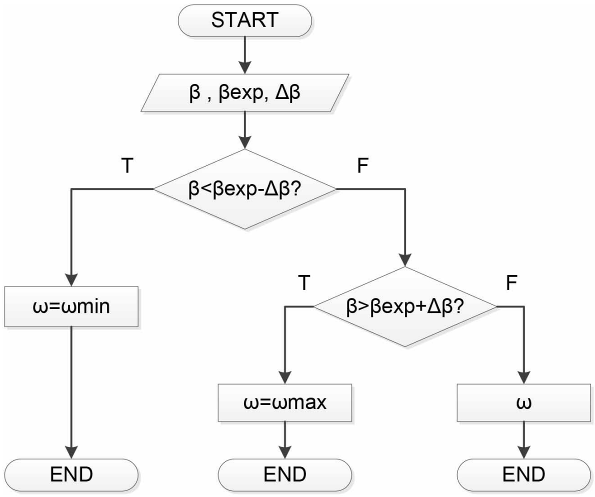

Figure 2.12: Flow chart of the tracking mechanism.

Computing the solar position has some advantages respect to systems that move the PTC based on a feedback signal: there is no disturbance due to clouds or sky shading and a high precision can be reached. But there are also some disadvantages: a positioning error in the PTC axis (not pointing due north or east) or small misalignments or imperfections in the geometry can produce tracking errors.

2.3 Test Bench and Methodology

Outdoor tests were performed in Ancona, Italy (latitude 43.5867 N, longitude 13.5150 E) and the ANSI/ASHRAE Standard 93-2010 [51] was adopted as a reference. In order to define the thermal efficiency of the PTC, the following quantities need to be measured: mass flow rate $\dot{m}$, inlet (T_{fi}) and outlet (T_{fo}) fluid temperatures, and direct normal irradiance DNI. The specific heat at constant pressure of the working fluid c_p and aperture area A_{a} must also be calculated.

The test bench is composed of two parts: the hydraulic circuit and the signal acquisition and calculation system.

2.3.1 Hydraulic Circuit

The hydraulic system used for the tests is composed of a primary and a secondary circuit. The heat transfer fluid (HTF), which absorbs heat passing through the PTC receiver, flows in the primary circuit. Instead, a cooling fluid (water in the case under study) flows in the secondary circuit in order to subtract heat from the HTF. The primary and secondary circuits interact by means of a heat exchanger which guarantees optimal conditions of heat transfer and avoids contamination between the two fluids.

The piping and instrumentation (P&I) diagram of the hydraulic circuit is reported in Figure 2.13. The diagram shows the interconnections between the devices, the piping system, and the control instrumentation. The primary circuit is drawn in red, while the secondary circuit is in blue. Starting from the PTC prototype UNIVPM.02, which was described in the previous sections, the primary circuit elements are discussed here.

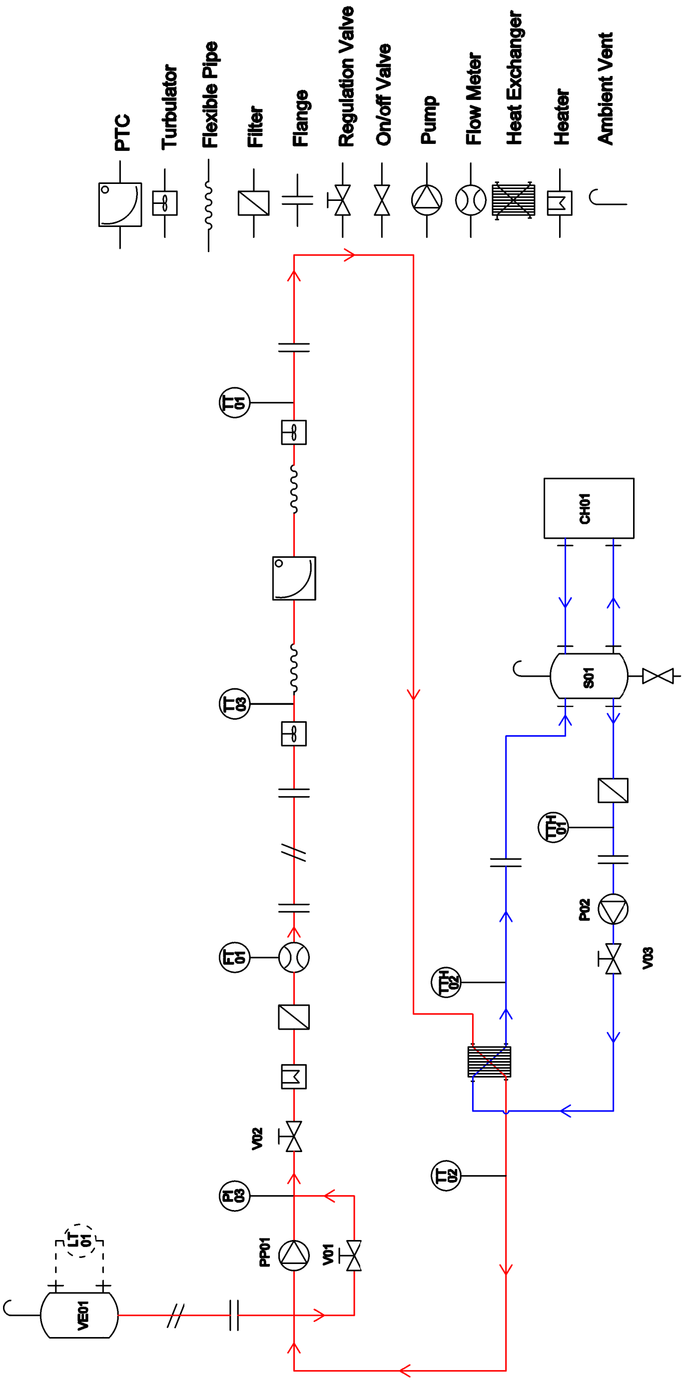

Figure 2.13: Hydraulic circuit P&I.

Flexible Pipe They are two and connect the PTC to the test bench. The tubes are made of steel and have spherical joints. In order to guarantee good thermal insulation, in particular of the inlet tube, elastomeric and mineral wool coatings were used.

Heat Exchanger It is a plate heat exchanger with a countercurrent flow arrangement. It simulates a thermal energy demand by absorbing heat from the HTF.

Expansion Tank VE01 It is located in the highest part of the bench and is able to absorb the HTF volume variations caused by the temperature rising during tests.

Pump PP01 It is a volumetric gear pump coupled to an asynchronous three-phase motor (three poles, 50 Hz, 220 V). The elaborated flow rate is independent of hydraulic head and depends only on the pump rotational speed. It can work both with water and diathermic oil.

Regulation Valve V01 This bypass valve was used to reduce the HTF elaborated by the pump in order to balance the fluid temperature variation.

Heater It is a 1.5 kW electric resistance having a 8 mm inner diameter and a 250 mm long sensible element. The heater transfers heat to the HTF with the aim to compensate heat losses and maintain a constant inlet fluid temperature during experimental tests. The socket is composed of a metal cylinder with a greater diameter.

Filter A filter was installed to avoid the presence of impurities in the pipes.

Turbulator Turbulators are small metal twisted-tape ribbons located inside the inlet and outlet sections of the absorber. They are fixed through brackets which also allow the correct positioning of resistance thermal detectors (RTDs). Their function is to facilitate the HTF turbulence, in order to enhance the heat transfer rate between the fluid itself and the absorber.

The devices installed in the secondary circuit are described as follows.

Chiller CH01 It is also referred to as economizer and reduces the cooling fluid temperature in the secondary circuit. The chiller is controlled by a remote controller having several set point temperatures.

Storage Tank S01 It is a 100 liters cooling fluid tank working as an inertial accumulator: it absorbs the possible temperature fluctuations and represents a constant temperature tank for the heat exchanger. It is a metal sheet made of hot zinc carbon steel and its internal and external insulation includes an anti-condensation system. The tank was positioned on the same chiller framework and was connected to this last one and to the secondary circuit by means of rubber pipes.

Circulator P02 It allows the cooling fluid to flow from the storage tank to the heat exchanger and consists of a centrifugal wet-rotor mono-phase pump (50 Hz, 230 V, two magnetic poles). The circulator has three power levels (220, 228, and 260 W) which can be manually selected by rotating a lever. In addition to the power levels, the circulator delivery can be also regulated by a manual ball valve (V03). However, since this valve is more properly an intercept valve, in order to guarantee a preciser regulation, the circulator was controlled by an inverter. In this way, the pump rotational speed could be regulated according to the following equation:

$$n = (1 - s)\frac{120f}{p} \tag{2.6}$$

where n is the rotor rotational speed, s is the slip, f is the frequency, and p is the number of magnetic poles.

The heat transfer fluid used during experimental tests was demineralized water at atmospheric pressure. According to several calculations based on the dimensions of the primary piping and the heat exchanger, the overall HTF volume contained in the primary circuit was equal to about 9 liters. The HTF level in the circuit could be visualized through a level indicator installed on the expansion tank.

2.3.2 Instruments and Computational Procedure

The test bench includes measurement instruments with the purpose to characterize the PTC prototype according to the ANSI/ASHRAE Standard 93-2010. A volumetric flow meter (FT01 in Figure 2.13), having a declared precision of ±0.8% the measured quantity, was installed to determine the HTF volumetric flow rate and, hence, its mass flow rate, $\dot{m}$. A constant value of about 0.14 l/s was chosen both to satisfy the Standard requirements and to guarantee a turbulent regime.

Five Pt100 AA Class resistance thermal detectors (RTDs) were adopted to detect the fluid temperatures in different points of the circuit. Referring to Figure 2.13, these are:

- TT01, located at the receiver outlet;
- TT02, located at the heat exchanger primary outlet;
- TT03, located at the receiver inlet;
- TTH01, located at the heat exchanger secondary inlet;
- TTH02, located at the heat exchanger secondary outlet.

The two RTDs for measuring inlet (T_{fi}) and outlet temperature (T_{fo}) were inserted in the double end of the receiver. The maximum tested inlet temperature was about 85 °C, in order to avoid water vaporization. Ambient temperature, T_{amb}, was measured with a T-type thermocouple.

The direct normal irradiance, DNI, was measured using a first-class [52] normal-incidence pyrheliometer (NIP) mounted on a solar tracker [53]. The pyrheliometer has a 1 second time response, a temperature dependence of ±1% in the range from −20 to 40 °C, and shows a linear relationship of ±0.5% in the range 0–1400 $\mathrm{W/m^2}$.

The remaining part of the test loop consists of the signal acquisition and calculation system. Figure 2.11 shows a schematic of the data flow through the instrumentation. An Agilent 34970A data-acquisition unit was used for all data acquisition and for thermocouple compensation.

2.4 Thermal and Optical Analysis

A PTC thermal efficiency, η, is defined as the ratio of useful energy delivered to the heat transfer fluid to the energy collected from the aperture area of the collector. It is a function of the optical performance of the PTC and the amount of thermal losses.

When the angle of incidence, θ, defined as the angle between the solar rays and the normal to the aperture area of the collector, is $\simeq 0$ (i.e., when solar rays are nearly parallel to the normal), the analytic expression relating the parameters mentioned above is [5]:

$$\eta = \frac{\dot{m}\, c_p (T_{\mathrm{fo}} - T_{\mathrm{fi}})}{DNI\, A_{\mathrm{a}}} = F_{\mathrm{R}} \left[\eta_{\mathrm{o,n}} - \frac{U_{\mathrm{L}}}{C} \left(\frac{T_{\mathrm{fi}} - T_{\mathrm{amb}}}{DNI} \right) \right] \tag{2.7}$$

While the first ratio in Equation (2.7) derives directly from the definition of thermal efficiency and includes experimentally measurable quantities, the second expression can be obtained by carrying out an energy balance calculation for the receiver. In the second expression, $\eta_{\mathrm{o,n}}$ is the optical efficiency of the collector at normal incidence, defined as the ratio of solar radiation reaching the absorber to the energy collected from the aperture area. It can be expressed as [51]:

$$\eta_{\mathrm{o,n}} = \left[(\tau\alpha)\rho\gamma \right]_{\mathrm{n}} (1 - A_{\mathrm{f,n}}) \tag{2.8}$$

where:

- $(\tau\alpha)$ is the transmittance-absorptance product;
- ρ is the specular reflectance of the parabolic mirror;
- γ is the intercept factor, the fraction of reflected energy that is directed towards the receiver [54];
- A_{f} is the ratio of ineffective area due to geometrical effects [55] (e.g., shading due to blockages and the receiver, and solar rays reflected from the mirror past the end of the receiver) to the whole aperture area of the collector.

The heat removal factor F_{R} and the overall loss coefficient U_{L} depend on heat losses and are independent of the angle of incidence. In particular, heat loss from the collector is related to [56]:

- the collector geometry and materials;
- working conditions (inlet fluid temperature T_{fi}, mass flow rate $\dot{m}$, thermophysical properties of the heat transfer fluid);
- environmental conditions (ambient temperature T_{amb}, wind velocity, relative humidity, direct normal irradiance DNI).

Experimental investigations show that, if thermal efficiency η is plotted against the operative term $(T_{\mathrm{fi}} - T_{\mathrm{amb}})/DNI$, the data are related linearly. Thus, the expression on the right-hand side of Equation (2.7) can be considered as a straight line, with intercept a and slope b defined as follows:

- $a = F_{\mathrm{R}}\eta_{\mathrm{o,n}}$;
- $b = -\left(F_{\mathrm{R}}U_{\mathrm{L}}\right)/C$.

Actually, the thermal efficiency of a PTC is generally given in the form of a linear equation. Defining the operative term $T^* = (T_{\mathrm{fi}} - T_{\mathrm{amb}})/DNI$, it is possible to write:

$$\eta = a + bT^* \tag{2.9}$$

Experimental data can be used to estimate the optical efficiency $\eta_{\mathrm{o,n}}$ and the intercept factor γ_{n} at normal incidence conditions, i.e., when $\theta \simeq 0$. Let us consider the system of three equations of variables F_{R}, U_{L}, and F' (see Duffie and Beckman [28] for further details, and note that λ_{a} is the absorber pipe thermal conductivity):

$$\begin{cases} b = -\left(F_{\mathrm{R}} U_{\mathrm{L}}\right)/C \\ F_{\mathrm{R}} = \frac{\dot{m}\, c_p}{A_{\mathrm{r}} U_{\mathrm{L}}} \left[1 - \exp\left(-\frac{A_{\mathrm{r}} U_{\mathrm{L}} F'}{\dot{m}\, c_p}\right)\right] \\ F' = \frac{1/U_{\mathrm{L}}}{1/U_{\mathrm{L}} + D_{\mathrm{ao}}/(h_{\mathrm{f}}\, D_{\mathrm{ai}}) + D_{\mathrm{ao}} \ln\left(D_{\mathrm{ao}}/D_{\mathrm{ai}}\right)/(2\lambda_{\mathrm{a}})} \end{cases} \tag{2.10}$$

In order to solve this system of equations to obtain a more useful expression for F_{R}, the experimental value b, geometrical (C, A_{r}, D_{ai}, D_{ao}), process ($\dot{m}$, c_p), and material (λ_{a}) parameters have to be determined. The convective heat transfer coefficient between the absorber and the fluid h_{f} must be calculated. In this way, by substituting the expressions for b and F' in the expression of F_{R}, it is possible to find that:

$$F_{\mathrm{R}} = bC \left[\frac{A_{\mathrm{r}}}{\dot{m}\, c_p \ln\left(1 + \frac{A_{\mathrm{r}} bC}{\dot{m}\, c_p}\right)} + \frac{D_{\mathrm{ao}}}{h_{\mathrm{f}} D_{\mathrm{ai}}} + \frac{D_{\mathrm{ao}}}{2\lambda_{\mathrm{a}}} \ln\left(\frac{D_{\mathrm{ao}}}{D_{\mathrm{ai}}}\right) \right] \tag{2.11}$$

Once F_{R} has been determined, the optical efficiency at normal incidence $\eta_{\mathrm{o,n}}$ can be obtained from the expression of the intercept value a. Considering that for $\theta \simeq 0$ the contribution of $A_{\mathrm{f,n}}$ is only due to the shading of the receiver on the collector, the intercept factor at normal incidence γ_{n} can be calculated from Equation (2.8) when τ_{n}, α_{n}, and ρ_{n} are known.

2.5 Results

2.5.1 Thermal Efficiency

Figure 2.14 shows the experimental thermal-efficiency data from UNIVPM.02 for various combinations of inlet fluid temperature, ambient temperature, and direct normal irradiance. Tests were carried out during clear sky and near-normal incident conditions, with the PTC axis oriented in the EW direction. The obtained experimental data were carefully analyzed and only the most representative points were considered. By fitting the data, the following equation for the straight line representing the thermal efficiency was determined:

$$\eta = 0.555 - 2.188\, T^{*} \tag{2.12}$$

Equation (2.12) is shown in Figure 2.14 along with the experimental data. From the graph, it is possible to observe that the error bars are greater when T^{*} increases: this is due to the RTD uncertainty, which is linearly increasing with the detected temperature.

Comparison with efficiency expressions derived from literature reveals a slope that is higher than average (see Table 2.5). This can be explained considering that the UNIVPM.02 receiver is not evacuated. In fact, as shown in Table 2.5, other collectors with unshielded receivers have comparable slopes. Among these, if the $-bC$ product is taken into account, the value assumed by UNIVPM.02 is the lowest. In general, the parameter $-bC$ represents a good way to estimate the thermal losses of a PTC when F_{R}, and therefore U_{L}, are not available.

From the intercept a and the slope b, information regarding the optical efficiency $\eta_{\mathrm{o,n}}$ and the intercept factor γ_{n} at normal incidence can be obtained. In turbulent

Table 2.5: Comparison of different PTC parameters. The symbol (-) indicates that the receiver considered is unshielded.

Reference	Year	a	$-b$ (W/m^2°C)	C	$-bC$ (W/m^2°C)	ϕ_r (°)	$\eta_\mathrm{o,n}$	γ_n	τ_n	α_n	ρ_n	F_R	U_L (W/m^2°C)
UNIVPM.02	2015	0.555	2.188	11.89	26.02	90	0.603	0.725	-	0.90	0.94	0.919	47.33
UNIVPM.01 [43]	2014	0.658	0.683	9.25	6.32	90	0.668	0.829	0.93	0.95	0.94	0.985	6.42
[42] (PTC90)	2013	0.613	2.302	13.3	30.62	90	0.70	0.84	-	0.90	0.92	0.88	34.98
[42] (PTC45)	2013	0.351	2.117	14.9	31.54	45	0.48	0.58	-	0.90	0.92	0.73	43.09
[41]	2012	0.561	2.047	14.87	30.44	45	0.60	0.665	-	0.95	0.95	0.94	32.56
[40]	2011	0.054	0.189	38.84	7.32	65.56	n.a.	n.a.	0.95	0.95	0.59	n.a.	n.a.
[39]	2007	0.69	0.39	19.89	7.76	90	0.694	0.879	0.9	0.9	0.97	0.99	7.79
[35] (shielded)	2005	0.538	1.059	16.7	17.69	82.2	0.553	0.823	0.92	0.88	0.83	0.97	18.23
[35] (unshielded)	2005	0.552	2.009	16.7	33.55	82.2	0.601	0.823	-	0.88	0.83	0.92	36.47
[57]	1996	0.638	0.387	21.2	8.20	90	0.647	0.94	0.90	0.90	0.85	0.99	8.29
[33]	1994	0.642	0.441	21.2	9.36	90	0.648	0.98	n.a.	n.a.	n.a.	0.99	9.44
[58]	1984	0.65	0.382	n.a.	n.a.	n.a.	n.a.	n.a.	n.a.	n.a.	n.a.	n.a.	n.a.
[59]	1982	0.66	0.233	16.42	3.83	90	n.a.	n.a.	0.9	0.94	0.78	n.a.	n.a.

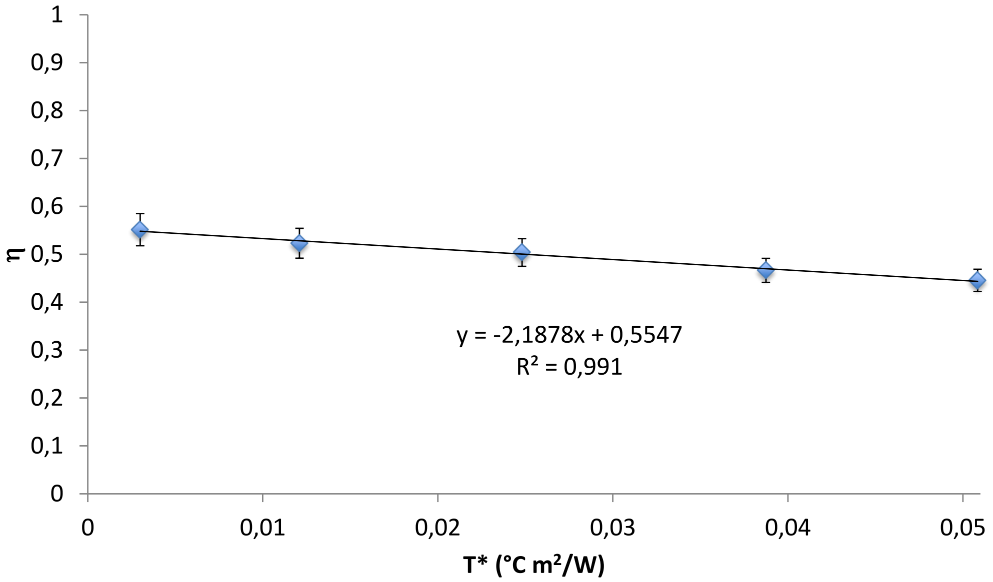

Figure 2.14: Experimental results and fit of the thermal efficiency of UNIVPM.02. R^2 is the coefficient of determination.

regime, the convective heat transfer coefficient between the absorber and the fluid can be evaluated by considering the Gnielinski [60] correlation for the Nusselt number:

$$h_\mathrm{f} = \frac{\lambda_\mathrm{f}}{D_\mathrm{ai}} Nu = \frac{\lambda_\mathrm{f}}{D_\mathrm{ai}} \left[\frac{(f/8)\,(Re-1000)\,Pr}{1+12.7(f/8)^{1/2}\left(Pr^{2/3}-1\right)} \right] \tag{2.13}$$

valid for $0.5 \leq Pr \leq 2\times10^3$ and $3\times10^3 < Re < 5\times10^6$. In Equation (2.13), λ_f is the thermal conductivity of the heat transfer fluid, Re is the Reynolds number, Pr is the Prandtl number, and f is the coefficient of friction, which can be calculated from the Colebrook equation [61]. Considering liquid water as the heat transfer fluid, a model based on the IAPWS (International Association for the Properties of Water and Steam) industrial formulation [62] was adopted to calculate $h_\mathrm{f} = 754\,\mathrm{W/(m^2\,°C)}$. Thus, Equation (2.11) yields $F_\mathrm{R} = 0.919$ and, from the definition of the intercept a:

$$\eta_\mathrm{o,n} = \frac{a}{F_\mathrm{R}} = 0.603 \tag{2.14}$$

Finally, considering shading on the collector aperture area due to the presence of the receiver, $A_\mathrm{f,n} = (D_\mathrm{ao}L_\mathrm{m})/A_\mathrm{a} = 0.016$, and from Equation (2.7) one obtains:

$$\gamma_\mathrm{n} = \frac{\eta_\mathrm{o,n}}{\left[(\tau\alpha)\rho\right]_\mathrm{n}(1-A_\mathrm{f,n})} = 0.725 \tag{2.15}$$

2.5.2 Incident Angle Modifier

The optical efficiency in Equation (2.8) is independent of the angle of incidence but, in reality, it strongly depends on this quantity. Since η_o is difficult to be described analytically and measured for off-normal incidence angles, a factor called incident angle

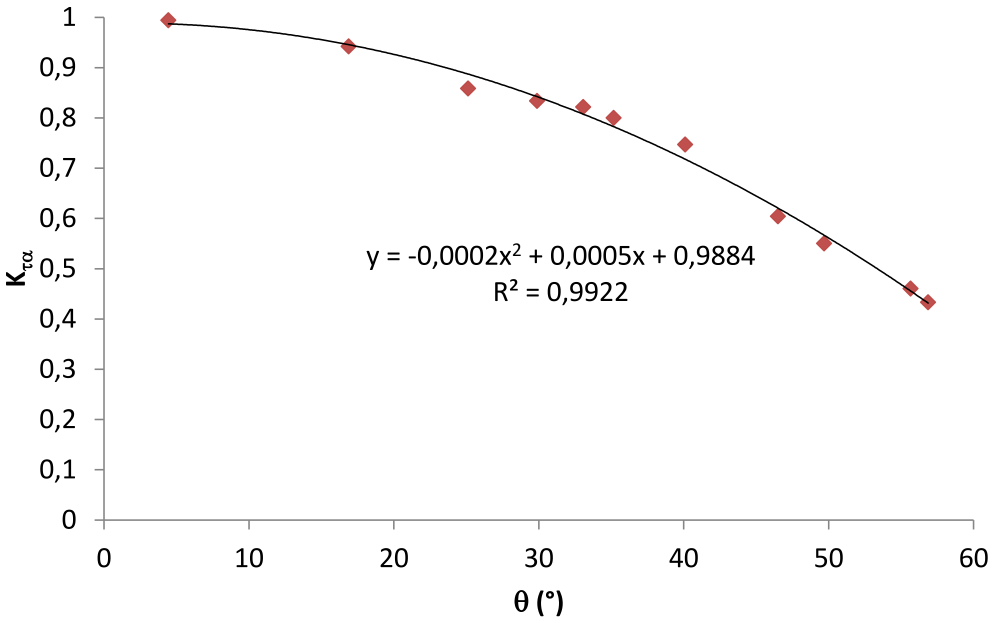

Figure 2.15: Incident angle modifier curve of UNIVPM.02.

modifier, $K_{\tau\alpha}$, is usually provided to take into account the effect of the incident angle. The incidence angle modifier is given by [51]:

$$K_{\tau\alpha} = \frac{(\tau\alpha)\rho\gamma(1 - A_{\mathrm{f}})}{[(\tau\alpha)\rho\gamma]_{\mathrm{n}}(1 - A_{\mathrm{f,n}})} = \frac{\eta_{\mathrm{o}}}{\eta_{\mathrm{o,n}}} \tag{2.16}$$

For the PTC prototype presented in this work, the incident angle modifier was obtained according to the ANSI/ASHRAE Standard 93-2010. Figure 2.15 shows the incident angle modifier data points plotted against the angle of incidence; the regression curve is also provided. It is possible to note that $K_{\tau\alpha}$ decreases rather rapidly with θ: this can be explained by considering that the receiver is not longer than the concentrator. Therefore, end effects [55] are relevant for higher angles of incidence, and the optical efficiency is consequently reduced.

The regression curve depicted in Figure 2.15 is a second order polynomial equal to (θ is expressed in degrees):

$$K_{\tau\alpha} = 0.9884 + 0.0005\,\theta - 0.0002\,\theta^2 \tag{2.17}$$

2.5.3 Time Constant

A PTC time constant allows to evaluate the collector transient behavior and is defined as the time, t, the PTC takes to go from its delta temperature with no solar radiation to 63.2% of its delta temperature at a steady state condition, given a stable exposure:

$$\frac{T_{\mathrm{fo}}(t) - T_{\mathrm{fi}}}{T_{\mathrm{fo,s}} - T_{\mathrm{fi}}} = 0.632 \tag{2.18}$$

where $T_{\mathrm{fo,s}}$ is the stabilized outlet temperature.

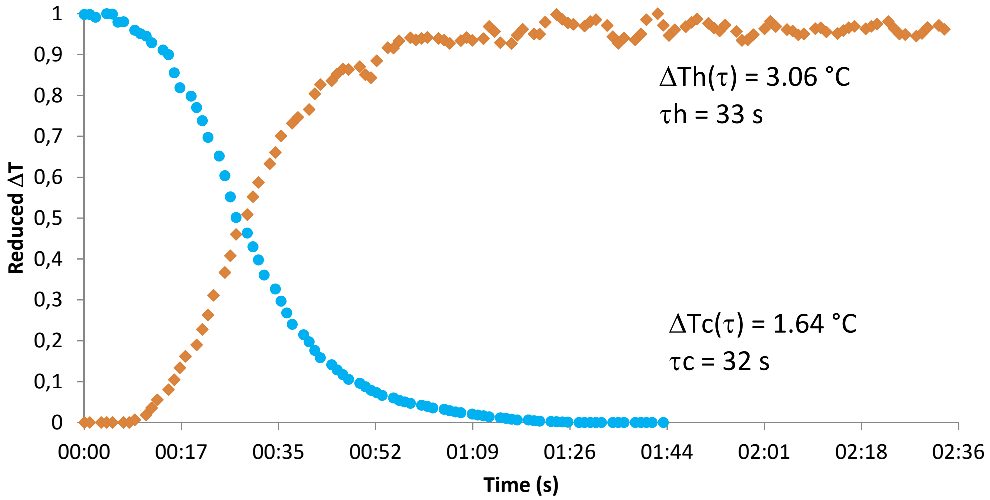

Figure 2.16: Time constants of UNIVPM.02.

To determine the time constant of UNIVPM.02, the inlet fluid temperature T_{fi} was set to a value equal to about the ambient temperature. Then, the PTC was covered and, once temperature stabilization was reached, the cover was removed and the acquisition started. This procedure is referred to as heating test. An inverse (cooling) test was also carried out, i.e. once the delta temperature was stabilized, the PTC was covered and data were acquired until $T_{\mathrm{fo,s}} = T_{\mathrm{fi}}$.

The acquired data are reported in Figure 2.16, where time is indicated in the abscissa and reduced temperature, i.e. the left-hand side of Equation (2.18), is reported in the ordinate. As can be seen, the time constants for both heating, t_{h}, and cooling, t_{c}, of the PTC are comparable, being equal to 33 s and 32 s, respectively.

Chapter 3

Nanofluid-based Parabolic Trough Collectors: Simulation of the Yearly Yield

In order to increase the thermal efficiency of low-enthalpy parabolic trough solar collectors (PTCs), a numerical analysis for the yearly yield evaluation of nanofluid-based PTCs was conduced. Six water-based nanofluids at different weight concentrations are investigated: Fe_2O_3 (5, 10, 20 wt%), SiO_2 (1, 5, 25 wt%), TiO_2 (1, 10, 20, 35 wt%), ZnO (1, 5, 10 wt%), Al_2O_3 (0.1, 1, 2 wt%), and Au (0.01 wt%). A simulation environment was validated by experimental tests using water as heat transfer fluid, in two PTC prototypes located in the city of Ancona (central Italy), while the convective heat transfer coefficient of nanofluids was measured through a dedicated apparatus. A typical meteorological year was built to perform the simulation, which presents a time-resolution of one hour. A specific arrangement for the PTC was defined, while different inlet fluid temperatures were considered at a mass flow rate of 0.50 kg/s: 40, 50, 60, 70, and 80 °C. For this last temperature, the variation in flow rate was also studied (at 1 kg/s and 1.5 kg/s). Results show that only Au, TiO_2, ZnO, and Al_2O_3 nanofluids at the lower concentrations, present small improvements compared to the use of water, while increasing the concentration of nanoparticles no advantage respect to water appears.

3.1 Nanofluids for Thermal Applications

The term nanofluid was introduced by Choi in 1995 [63] to describe a new class of heat transfer fluids obtained through nanotechnological processes. A nanofluid is a solution composed by a base fluid (e.g., water) and a solute uniformly dispersed in form of solid particles with nanometric dimension. Different types of nanoparticles were studied in literature: oxide ceramics, nitride ceramics, carbide ceramics, metals, semiconductors, carbon nanotubes, carbon nanohorns, and composite materials. If the suspension is stable, a reduced quantity of nanoparticles could increase the thermal properties of the base fluid. In the light of the previous considerations, it is reasonable to expect an increase in the thermal efficiency of PTCs when the heat transfer base fluid is substituted with a nanofluid of appropriate concentration of nanoparticles.

Some literature papers discuss how nanofluids affect solar PTCs, e.g., in Kasaeian et al. [64] carbon nanotube/oil based nanofluids were tested as working fluids finding an enhancement of 11% in the global efficiency of vacuumed tube. A literature review [65] on the applications of nanofluids in solar energy systems concluded indicating the necessity of further studies on the characterization of nanofluids, due to controversial results obtained until now. Another review [66] considered the efficiency in cooling photovoltaic and thermal solar collector systems.

SiO_2–water nanofluid is a promising heat transfer media: in literature it was studied in horizontal tubes finding an enhancement of heat transfer coefficient compared to pure water from 10% to 60% [67], in tubes under both steady and vibration states observing the larger increase of about 182% [68], and in Azmi et al. [69] obtaining a maximum heat transfer coefficient of 94.1% in a tube with twisted tape inserts. However, nanofluids are very complex fluids and experimental data acquired by using different experimental techniques could be different. Therefore, within an International Nanofluid Property Benchmark Exercise, thermal conductivity of identical samples of stable colloidal dispersions of nanoparticles was studied at ambient temperature by over 30 organizations worldwide, using a variety of experimental approaches [70]. In this work, we consider one of those nanofluids, SiO_2, 50 wt%, Grace & Co., Ludox TM-50. Thermal conductivity measurements [71] found a good agreement (the deviation is 0.1%) with measurements at the same conditions by Buongiorno et al. [70]. Water-based SiO_2 nanofluid was studied in a loop thermosyphon [72] and in a car radiator [73]. There are not studies involving SiO_2 nanofluids in a PTC.

TiO_2–water nanofluid is one of the most investigated nanofluids. Murshed et al. [74] showed that thermal conductivity increases with an increase of particle volume fraction, and that the particle size and shape also have effects on the enhancement of thermal conductivity. As concerns dynamic viscosity, the rheological behavior and suspension structure of TiO_2 nanoparticles dispersed in pure water have been investigated, generally exhibiting a pseudoplastic flow behavior and indicating an existence of particle aggregations in the liquid medium [75].

Thermophysical properties of Fe_2O_3 are object of several works, e.g., Phuoc and Massoudi [76] observed the rheological properties of Fe_2O_3 water-based nanofluids finding a non-Newtonian behavior, Pastoriza-Gallego et al. [77] investigated the rheological properties of Fe_2O_3 in ethylene glycol, and Vermahmoudi et al. [78] measured an improvement on the heat transfer coefficient of water-based iron oxide nanofluid in a compact aircooled heat exchanger. Other studies considered the applications of ferro-nanofluids on a micro-transformer [79], or the electrical and magnetic properties of ferro-nanofluid on transformers [80], or magnetic nanofluids [81] based on Fe_3O_4 nanoparticle.

Few works study ZnO nanoparticles dispersed in pure water. Amongst them, Ferrouillat et al. [82] obtained a small improvement of Nusselt numbers of studied nanofluids compared to those of the base fluid, while several papers showed studies on ZnO nanoparticles dispersed in ethylene glycol [83] or water-ethylene glycol [84] mixtures.

An improvement in heat transfer was found employing Al_2O_3/oil nanofluid as heat transfer fluid [85]. Kole and Dey [86] prepared various suspensions containing Al_2O_3 nanoparticles to be used in a car engine coolant using oleic acid as the surfactant; the concentration of 0.035% volume fraction displayed a fairly higher thermal conductivity than the base fluid and a maximum enhancement of about 10.41% was observed at room temperature. In the work of Yousefi et al. [87], the effect of Al_2O_3–water nanofluid on the efficiency of a flat-plate solar collector was investigated experimentally; the results showed that, respect to water, for 0.2 wt% the increased efficiency was 28.3%.

An aqueous solution of various-sized gold nanoparticles was employed as working medium for conventional circular heat pipe [88]; it was found that at a same charge volume, there is a significant reduction in thermal resistance of heat pipe with nanofluid as compared with water. The thermal conductivity of three volumetric fractions of gold/1-butyl-3-methylimidazolium hexafluorophosphate (Au/[Bmim][PF6]) was measured by a transient hot wire method and the results indicate that the thermal conductivity of the largest fraction is 13.1% higher than that of [Bmim][PF6] at 81 °C [89]. Shalkevich et al. [90] evaluated the thermal conductivity of gold nanofluids and, despite a significant search in parameter space, no significant anomalous enhancement of thermal conductivity was observed; the highest enhancement in thermal conductivity was 1.4% for 40 nm sized gold particles.

However, nanofluids formed by TiO_2, SiO_2, Fe_2O_3, ZnO, Al_2O_3, Au, and water were never considered in low-enthalpy PTCs. Thus, in this work the results obtained from a simulation environment suitable to calculate the yearly yield of a nanofluid-based low-enthalpy PTC, are presented. The aim of this study is to investigate the energy benefits of using nanofluids instead of water in a PTC. The numerical simulations were carried out for nanofluids in the liquid phase and for inlet fluid temperatures up to 80 °C. To date, it is difficult to test the thermo-physical properties of water-based nanofluids at atmospheric pressure and temperatures higher than 100 °C, especially because during the evaporating phase it is difficult to control nanoparticles. Therefore, the investigations are limited to low temperatures, in order to prove the convenience of nanofluids in this temperature range. Obviously, investigations at higher temperatures will play an important role with concentrating collectors such as PTCs, but additional data on nanofluids are required for the purpose.

3.2 Tested Nanofluids

The analysis includes six water-based nanofluids with different nanoparticles and particle concentrations ranging from 0.01 to 35 wt%. All the nanofluids were characterized in the Institute of Construction Technologies of National Research Council, Padua (Italy). Each nanofluid is commercial and bidistilled water (CARLO ERBA, Bidistilled water, CAS Nr 7732-18-5) was used to dilute the nanofluids to obtain the desired particle concentrations. The following nanofluids were considered:

- titanium dioxide (TiO_2) at 1, 10, 20 and 35 wt% (original nanofluid: 35 wt%, Sigma Aldrich);
- silicon dioxide (SiO_2) at 1, 5 and 25 wt% (original nanofluid: 50 wt%, Grace & Co., Ludox TM-50);
- iron oxide (Fe_2O_3) at 5, 10 and 20 wt% (original nanofluid: 20 wt%, Sigma Aldrich);
- zinc oxide (ZnO) at 1, 5 and 10 wt% (original nanofluid: 50 wt%, Sigma Aldrich);
- aluminum oxide (Al_2O_3) at 0.1, 1 and 2 wt% (original nanofluid: 10 wt%, Sigma Aldrich);
- gold (Au) at 0.01 wt% (Sigma Aldrich).

Dispersants and surfactants are often used to ensure the stability of the nanoparticles. Producers declared the presence of other components in Au–water nanofluid, acetic acid at 1–5 wt% in the TiO_2–water nanofluid, and 3-aminopropyltriethoxysilane at 2 wt% in the ZnO–water nanofluid. Fe_2O_3 and Al_2O_3–water nanofluid do not contain dispersants, while SiO_2–water nanofluid contains 500 ppm of a proprietary biocide.

To avoid that the tested fluids affected other systems, it was first ensured that the nanofluids were stable then, during conductivity and viscosity measurements, particular attention was paid to the interaction between nanofluids and instrumentation surfaces. For all the tests, it was possible to remove water-based nanofluids, using pure water. Furthermore, between two nanofluid measurements, one test was repeated using pure water as reference fluid in order to verify the value of a known fluid. No nanofluids deleterious effect was found.

It is worth noting that the experimental investigation of the thermophysical properties of SiO_2 [71], TiO_2 [91], Fe_2O_3 [92], and ZnO [93] were object of published papers, while the measurements of Al_2O_3 and Au are new [94]. All these measurements were used as input for the numerical simulation.

3.2.1 Thermal Conductivity Measurements

Thermal conductivity was measured using a Thermtest TPS2500, an instrument based on the Hot Disk technique with transient plane source. The sensor of the instrument is formed by a double nickel spiral covered by a Kapton insulating layer, which is immersed in the fluid in vertical position. It serves as plane source and the same sensor acquires the temperature increase during the transient period. A proper box, containing the sample and the sensor, is placed in a thermostatic bath to reach the test temperature. The power supplied by the sensor for each measurement was about 40 mW and the time of the power input was 4 s. The declared instrument uncertainty is 5%, however, tests performed on pure water revealed a percentage absolute average deviation AAD within 1% respect to REFPROP 9.0 database [95] at each experimental temperature.

3.2.2 Dynamic Viscosity Measurements

A rotational rheometer (AR G2, TA Instruments) was used to measure the dynamic viscosity of all the fluids. The geometry is formed of a static plate and a rotating 1° cone, between which the fluid sample was placed. The test temperature was imposed and controlled in both the plate and cone surfaces. For each test, at constant temperature, dynamic viscosity was measured varying the shear rate generally from 80 to 1200 Hz. The declared instrument uncertainty is 5%, however, as stated in Bobbo et al. [96], tests performed on pure water to test the instrument with a well-known fluid and to measure the viscosity of the base-fluid, revealed an AAD within 1.5% respect to REFPROP 9.0 database [95] at each experimental temperature.

3.3 Simulation Environment

A simulation environment was developed using Wolfram Mathematica for determining the yearly yield of a low-enthalpy PTC prototype serving an industrial heat demand profile. Starting from a mathematical model for the PTC thermal efficiency, validated by experimental results, a simulation was realized for the city of Ancona, situated in the center of Italy.

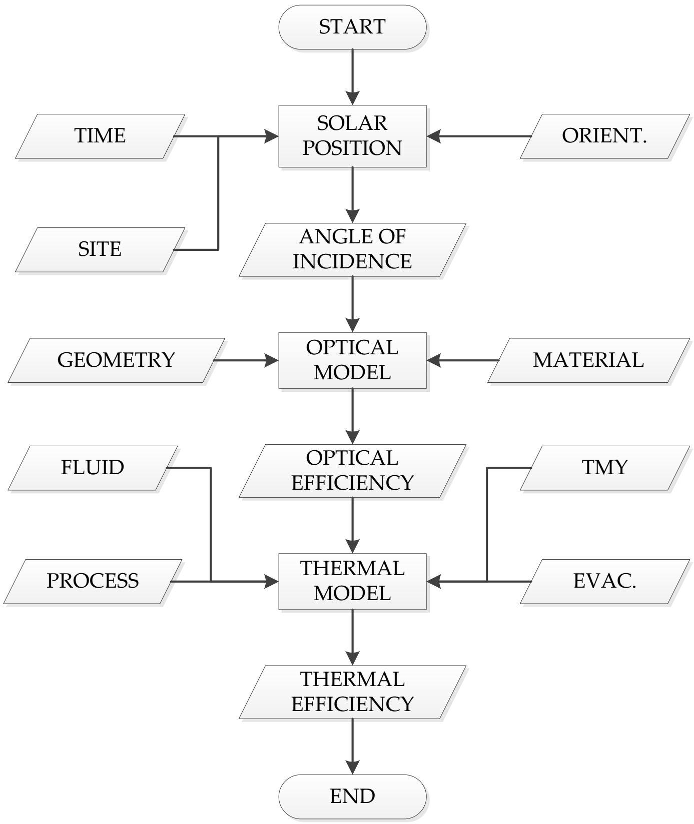

Figure 3.1: Flowchart of the simulation environment.

The flowchart of the simulation environment used for the purpose is shown in Figure 3.1. The environment consists of three processing blocks, represented with rectangles: Solar Position, Optical Model, and Thermal Model.

The main output of the system is the PTC plant thermal efficiency, η. However, once all routines have been performed, every single unknown quantity of the environment (temperatures, heat fluxes, etc.) is well-defined and available as output.

3.3.1 Input Blocks

The simulation environment requires the following input blocks, as shown in Figure 3.1.

Time Time consists of an array of 8760 elements, where each element contains the following information: year, month, day, and hour.

Site This block includes the PTC site latitude and longitude. These values are two scalars and are necessary to determine the sun position respect to the installation.

Orientation This input is a single boolean value that must be set accordingly with the PTC axis orientation: east-west horizontal or north-south horizontal.

Angle of Incidence It is the angle θ between the solar rays and the normal to the aperture area of the collector. In the proposed simulation environment, it is the output of the first processing block (Solar Position) and is needed to run the second (Optical Model) and the third processing block (Thermal Model). It is an array of 8760 elements.

Geometry Geometry contains all the characteristic dimensions of the PTC: mirror length (L_m), mirror aperture (W_m), receiver length (L_r), inner absorber diameter (D_ai), outer absorber diameter (D_ao), inner cover diameter (D_ci), outer cover diameter (D_co), focal distance (f). All these variables are scalar elements.

Material This category includes all the thermophysical properties of materials: mirror specular reflectance (r), extinction coefficient of the cover (K), conductivity of the cover (λ_c), emissivity of the cover (ϵ_c), absorptance of the absorber at normal incidence (α_n), conductivity of the absorber (λ_a), emissivity of the absorber (ϵ_a), roughness of the absorber (ξ). These parameters are scalars independent of temperature and wavelength.

Optical Efficiency It is the output of the second processing block (Optical Model) and is needed to run the third processing block (Thermal Model). Likewise θ, it is an array of 8760 elements.

Fluid This block contains all the thermophysical properties of the fluids involved in the simulation, i.e. the ambient air and the heat transfer fluid (HTF). Water at atmospheric pressure, superheated water, and other liquid HTFs such as heat transfer oils and nanofluids can be adopted for the simulation. Quantities required for the simulation are: thermal conductivity (λ_f), dynamic viscosity (μ_f), density (ρ_f), and specific heat at constant pressure ($c_{p,\mathrm{f}}$). The properties of air and nanofluids are function of temperature only, while the properties of water were evaluated with IAPWS-IF97 tables [62] and depend on both temperature and pressure.

Nanofluids need for better clarification. In fact, nanofluid density ρ_nf and nanofluid specific heat $c_{p,\mathrm{nf}}$ were calculated knowing nanoparticles density ρ_np and specific heat $c_{p,\mathrm{np}}$, and base fluid density ρ_bf and specific heat $c_{p,\mathrm{bf}}$ at each temperature, with the following correlations:

$$\rho_\mathrm{nf} = (1-\Phi)\rho_\mathrm{bf} + \Phi\rho_\mathrm{np} \tag{3.1}$$

and

$$c_{p,\mathrm{nf}} = (1-\phi)c_{p,\mathrm{bf}} + \phi c_{p,\mathrm{np}} \tag{3.2}$$

where Φ is the volume fraction of nanoparticles and ϕ is the mass fraction of nanoparticles.

Thermal conductivity and dynamic viscosity were experimentally measured as described in Section 3.2. Figure 3.2 and 3.3 report the thermal conductivity and the dynamic viscosity data of the adopted HTFs, respectively.

Process Process describes the type of heat demand and includes the variables $\dot{m}$ (mass flow rate), T_fi (inlet fluid temperature), and p (pressure). All these quantities are arrays of 8760 elements.

TMY This block includes the so-called TMY (Typical Meteorological Year), i.e., a year that is representative of the real meteorological conditions of the installation site. The TMY contains the following data: direct normal irradiance (DNI), ambient temperature (T_air), wind velocity (v_air), and relative humidity (RH). All these variables are arrays of 8760 elements.

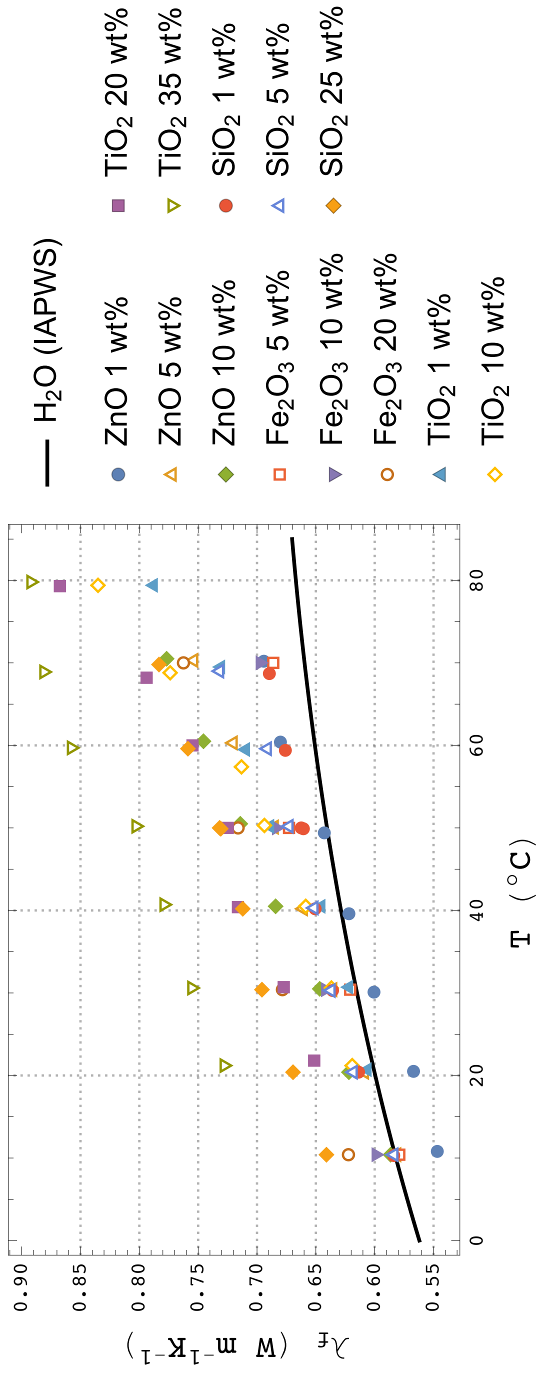

Figure 3.2: Thermal conductivity data of the HTFs adopted in the simulation.

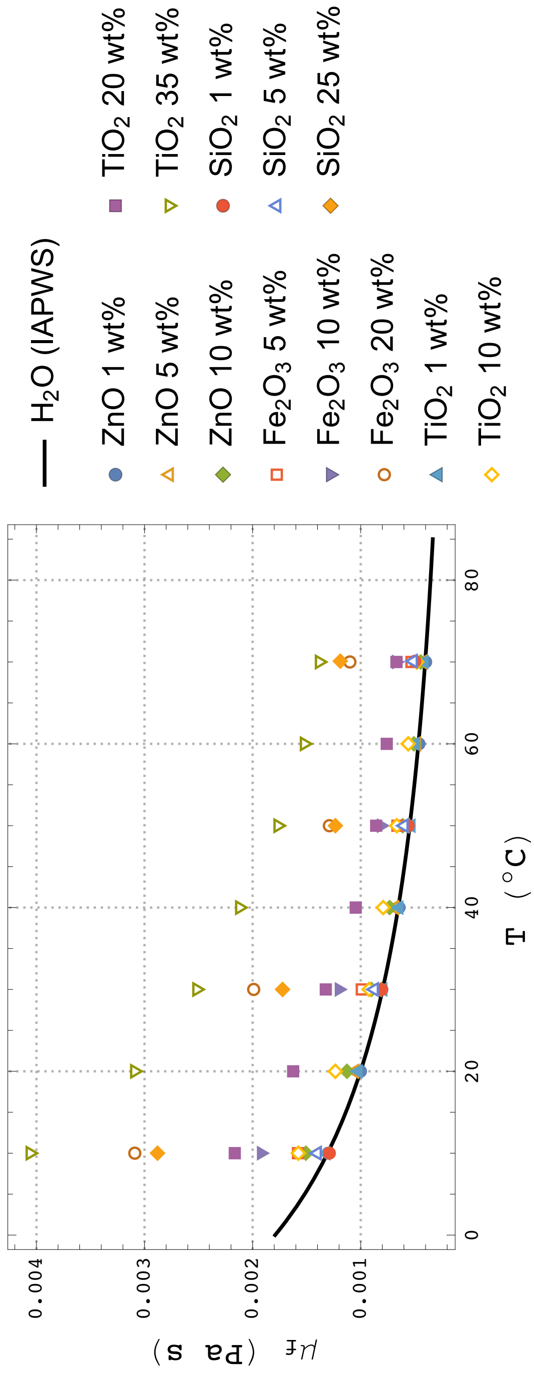

Figure 3.3: Dynamic viscosity data of the HTFs adopted in the simulation.

Evacuation Evacuation is a single boolean input and indicates if the receiver is evacuated or not.

3.3.2 Solar Position

For the present work, a solar algorithm taken from The Astronomical Almanac [97] and simplified by Michalsky [50] was used. Michalsky's algorithm has an accuracy of 0.01° until the year 2050, thus it is particularly suitable for solar collectors with high concentration ratios such as PTCs.

The algorithm needs the following block inputs (see Figure 3.1): a) Time, to establish when the sun position must be calculated; b) Site, that is fixed in each running; c) Orientation, which allows to define the position of the PTC axis. When the solar angles are calculated by the Michalsky's algorithm for each hour of the TMY, the angle of incidence, θ, can be found depending on the orientation (i.e., the tracking motion) of the PTC. For a plane rotated about a horizontal east-west axis with continuous adjustment to minimize the angle of incidence [28]:

$$\cos\theta = \sqrt{1 - \cos^2\delta \sin^2\omega} \tag{3.3}$$

where δ is the declination angle and ω is the hour angle.

On the other hand, for a plane rotated about a horizontal north-south axis with continuous adjustment to minimize the angle of incidence [28]:

$$\cos\theta = \sqrt{\cos^2\theta_\mathrm{z} + \cos^2\delta \sin^2\omega} \tag{3.4}$$

where θ_z is the zenith angle.

3.3.3 Optical Model

The Optical Model routine calculates the PTC optical performance. Geometry and Material variables are inputs, in addition to θ, which is the output of Solar Position. The optical efficiency array η_o, the output of the routine, is a function of θ and can be written as [51]:

$$\eta_\mathrm{o}(\theta) = (\tau\alpha) r \gamma \big(1 - A_\mathrm{f}\big) \tag{3.5}$$

where $(\tau\alpha)$ is the transmittance-absorptance product, r is the specular reflectance of the parabolic mirror, γ is the intercept factor, and A_f is the ratio of ineffective area due to geometrical effects to the whole aperture area of the collector [55] (e.g., shading due to blockages and the receiver, and solar rays reflected from the mirror past the end of the receiver). The transmittance of the cover, τ, was determined using Fresnel equations [5], while α, the absorptance of the absorber, was determined by the correlation reported in Beckman et al. [98] (θ is in degrees):

$$\begin{aligned} \alpha/\alpha_\mathrm{n} = 1 &- 1.5879 \times 10^{-3}\,\theta + 2.7314 \times 10^{-4}\,\theta^2 \\ &- 2.3026 \times 10^{-5}\,\theta^3 + 9.0244 \times 10^{-7}\,\theta^4 \\ &- 1.8000 \times 10^{-8}\,\theta^5 + 1.7734 \times 10^{-10}\,\theta^6 \\ &- 6.9937 \times 10^{-13}\,\theta^7 \end{aligned} \tag{3.6}$$

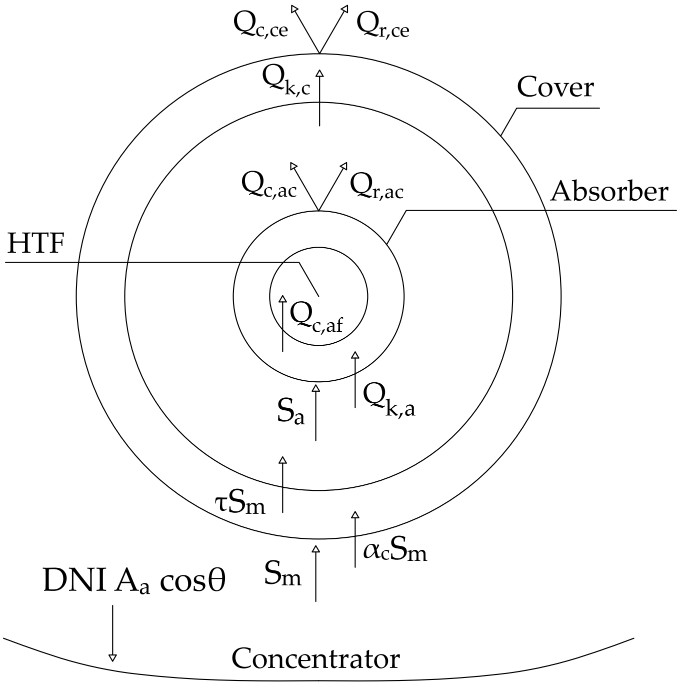

Figure 3.4: Energy balance for the cross-section of the collector.

3.3.4 Thermal Model

Thermal Model is the last processing block and solves the energy balance equations in the receiver cross-section. Thus, it allows to determine the PTC thermal efficiency and summarizes all the outputs of the simulation environment.

Four different categories of inputs are needed (see Figure 3.1): a) Fluid properties, in order to evaluate the flow regime and the convective heat transfers; b) Process variables; c) TMY; d) Evacuation, necessary to indicate the presence or absence of evacuation in the receiver. In addition, e) Geometry and f) Material properties, used in particular for the conductive and radiative heat transfers, are required. The previous outputs θ and η_{o} are also needed.

A number of simplifying assumptions were adopted to build the model: a) the thermal performances were evaluated under steady-state conditions; b) the heat transfer occurs only in the radial direction of the receiver; c) the thermophysical and optical properties of the materials are independent of temperature and wavelength (but may depend on the angle of incidence); d) the thermophysical properties of the considered heat transfer fluids (i.e., water and nanofluids) depend on temperature (and also on pressure in the case of water).

Figure 3.4 shows the steady-state energy balance for the cross-section of the collector, while Figure 3.5 shows the thermal resistance model of the receiver. When the beam radiation reflected by the mirror (S_{m}) strikes the cover, a fraction of solar energy is transmitted to the absorber (τS_{m}). Only a portion of this energy, S_{a}, is effectively conducted through the absorber ($Q_{\mathrm{k,a}}$) and transferred to the HTF by convection ($Q_{\mathrm{c,af}}$), while a significant portion is loss and transmitted back by convection ($Q_{\mathrm{c,ac}}$) and radiation ($Q_{\mathrm{r,ac}}$). The energy lost by convection and radiation is transmitted by

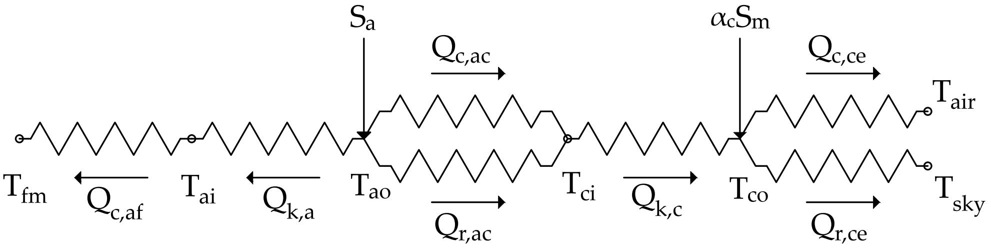

Figure 3.5: Thermal resistance model of the receiver.

conduction through the cover ($Q_{\mathrm{k,c}}$) and, along with the energy absorbed by the cover ($\alpha_{\mathrm{c}} S_{\mathrm{m}}$), is lost to the environment by convection ($Q_{\mathrm{c,ce}}$) and radiation ($Q_{\mathrm{r,ce}}$).

The system of energy balance equations is determined by applying the conservation of energy at each surface of the cross-section of the receiver in Figure 3.4:

$$\begin{cases} S_{\mathrm{a}} = Q_{\mathrm{k,a}} + Q_{\mathrm{c,ac}} + Q_{\mathrm{r,ac}} \\ Q_{\mathrm{k,a}} = Q_{\mathrm{c,af}} = Q_{\mathrm{u}} \\ Q_{\mathrm{c,ac}} + Q_{\mathrm{r,ac}} = Q_{\mathrm{k,c}} \\ Q_{\mathrm{k,c}} + \alpha_{\mathrm{c}} S_{\mathrm{m}} = Q_{\mathrm{c,ce}} + Q_{\mathrm{r,ce}} \end{cases} \tag{3.7}$$

The equations used for the heat fluxes in System (3.7) are provided in Table 3.1. Among the quantities that were not already defined in Section 3.3.1, the following were used:

- $A_{\mathrm{a}} = L_{\mathrm{m}} W_{\mathrm{m}}$ is the aperture area of the collector;
- α_{c} is the absoprtance of the cover (determined with Fresnel equations [5] in Optical Model);
- $h_{\mathrm{c,af}}$ is the convective heat transfer coefficient between the absorber tube and the fluid;
- λ_{eff} is the effective conductive coefficient used to evaluate the convective heat transfer between the absorber tube and the cover;
- σ is the Stefan-Boltzmann constant;
- $h_{\mathrm{c,ce}}$ is the convective heat transfer coefficient between the cover and the environment.

System (3.7) is a forth order system of algebraic equations with four unknown temperatures: T_{ai}, T_{ao}, T_{ci}, and T_{co}, which are, respectively, the temperatures relative to the internal and external surfaces of the absorber tube and the cover. The system is not linear as there are two radiative heat transfers, $Q_{\mathrm{r,ac}}$ and $Q_{\mathrm{r,ce}}$.

When the energy balance system is solved, the useful heat gain of the fluid, Q_{u}, is determined, and the PTC thermal efficiency can be calculated as:

$$\eta = \frac{Q_{\mathrm{u}}}{DNI\, A_{\mathrm{a}} \cos\theta} = \frac{\dot{m}\, c_{p,\mathrm{f}} (T_{\mathrm{fo}} - T_{\mathrm{fi}})}{DNI\, A_{\mathrm{a}} \cos\theta} \tag{3.8}$$

where T_{fo} is the outlet fluid temperature.

Table 3.1: Heat fluxes involved in the energy balance of the receiver.

Description	Equation
Rad. reflected towards the receiver	$S_{\mathrm{m}} = r\gamma(1 - A_{\mathrm{f}})DNI\,A_{\mathrm{a}}\cos\theta$
Rad. absorbed by the cover	$\alpha_{\mathrm{c}}S_{\mathrm{m}}$
Rad. collected by the absorber	$S = (\tau\alpha)r\gamma(1 - A_{\mathrm{f}})DNI\,A_{\mathrm{a}}\cos\theta$
Conduction through the absorber	$Q_{\mathrm{k,a}} = \frac{2\pi\lambda_{\mathrm{a}}L_{\mathrm{r}}(T_{\mathrm{ao}}-T_{\mathrm{ai}})}{\ln(D_{\mathrm{ao}}/D_{\mathrm{ai}})}$
Convection from the abs. to the fluid	$Q_{\mathrm{c,af}} = h_{\mathrm{c,af}}\pi D_{\mathrm{ai}}L_{\mathrm{r}}(T_{\mathrm{ai}} - T_{\mathrm{fm}})$
Useful heat gain of the fluid	$Q_{\mathrm{u}} = \dot{m}\,c_{p,\mathrm{f}}(T_{\mathrm{fo}} - T_{\mathrm{fi}})$
Conv. loss from the abs. to the cover	$Q_{\mathrm{c,ac}} = \frac{2\pi\lambda_{\mathrm{eff}}L_{\mathrm{r}}}{\ln(D_{\mathrm{ci}}/D_{\mathrm{ao}})}(T_{\mathrm{ao}} - T_{\mathrm{ci}})$
Radiation loss from the abs. to the cover	$Q_{\mathrm{r,ac}} = \frac{\pi D_{\mathrm{ao}}L_{\mathrm{r}}\sigma(T_{\mathrm{ao}}^4-T_{\mathrm{ci}}^4)}{1/\epsilon_{\mathrm{a}}+(1-\epsilon_{\mathrm{c}})(D_{\mathrm{ao}}/D_{\mathrm{ci}})/\epsilon_{\mathrm{c}}}$
Conduction loss through the cover	$Q_{\mathrm{k,c}} = \frac{2\pi\lambda_{\mathrm{c}}L_{\mathrm{r}}(T_{\mathrm{ci}}-T_{\mathrm{co}})}{\ln(D_{\mathrm{co}}/D_{\mathrm{ci}})}$
Conv. loss from the cover to the env.	$Q_{\mathrm{c,ce}} = h_{\mathrm{c,ce}}\pi D_{\mathrm{co}}L_{\mathrm{r}}(T_{\mathrm{co}} - T_{\mathrm{air}})$
Rad. loss from the cover to the env.	$Q_{\mathrm{r,ce}} = \epsilon_{\mathrm{c}}\pi D_{\mathrm{co}}L_{\mathrm{r}}\sigma(T_{\mathrm{co}}^4 - T_{\mathrm{sky}}^4)$

Finally, it should be noted that the convective heat transfers require to evaluate the properties of the fluids at temperatures that are initially unknown. Therefore, a iterative process was developed in Mathematica to overcame this instance: stopping criteria were set to guarantee a precision of 0.1 °C of the unknown temperatures. Convergence is generally obtained after 3 or 4 iteration cycles.

3.3.5 Environment Validation

The simulation environment was validated through the experimental results obtained from two PTC prototypes installed on the roof of DIISM (Department of Industrial Engineering and Mathematical Sciences). The latitude and the longitude of the installation site are 43.5867 north and 13.5150 east, respectively. Tests were carried out using water as HTF and with both prototypes axes oriented in the east-west direction.

The prototypes are called UNIVPM.01 and UNIVPM.02. Detailed information on the design, manufacture and testing of UNIVPM.01 are available in Coccia et al. [43], while the UNIVPM.02 characterization was presented in Chapter 2. The inputs of the two prototypes used for the validation of the simulation environment are provided in Table 3.2. These inputs are the geometrical characteristics of the prototypes and the thermo/optical properties of the adopted materials.

The main difference between the prototypes lies in the geometry of the mirror and the receiver: in fact, UNIVPM.02 has a greater concentration ratio (19.89) respect to UNIVPM.01 (9.25). It addition, UNIVPM.02 has an unshielded receiver.

A comparison between simulated and experimental results for UNIVPM.01 and UNIVPM.02 is provided in Figure 3.6 and Figure 3.7, respectively, where the thermal efficiency η is plotted against the the operative parameter $(T_{\mathrm{fi}} - T_{\mathrm{air}})/DNI$.

For the both of prototypes, the experimental η was measured according to the ANSI/ASHRAE Standard 93-2010 [51], which requires that the thermal efficiency is obtained through measurements of the quantities reported in Equation (3.8), in particular: mass flow rate, inlet and outlet fluid temperatures, and direct normal solar irradiance. The operative parameter $(T_{\mathrm{fi}} - T_{\mathrm{air}})/DNI$, which is also required by the Standard, allows to compare solar collectors tested in different environmental conditions; moreover, the parameter can be derived by a global energy balance of the receiver and is proportional to the thermal losses of the collector [99].

Table 3.2: Inputs used for the validation of the simulation environment.

Input	Symbol	UNIVPM.01	UNIVPM.02
Mirror length (m)	L_m	2.000	2.570
Mirror aperture (m)	W_m	0.925	2.500
Receiver length (m)	L_r	2.100	2.570
Inner abs. diam. (m)	D_ai	0.025	0.035
Outer abs. diam. (m)	D_ao	0.030	0.040
Inner cover diam. (m)	D_ci	0.046	-
Outer cover diam. (m)	D_co	0.048	-
Focal distance (m)	f	0.250	0.550
Mirr. specular reflectance	r	0.94	0.94
Extinction coeff. (1/m)	K	4	-
Cover cond. (W/(m K))	λ_c	1.40	-
Cover emissivity	ϵ_c	0.30	-
Norm. abs. absorptance	α_n	0.95	0.90
Abs. cond. (W/(m K))	λ_a	237	60
Abs. emissivity	ϵ_a	0.95	0.30
Abs. roughness (µm)	ξ	1.5	50
Mass flow rate (kg/s)	$\dot{m}$	0.045	0.13

Table 3.3: Deviations between calculated and experimental efficiencies for UNIVPM.01 and UNIVPM.02 PTC prototypes.

Quantity	UNIVPM.01	UNIVPM.02
$AAD = 100/n \sum_{i=1}^{n} \lvert\eta_{\mathrm{calc},i} - \eta_{\mathrm{exp},i}\rvert/\eta_{\mathrm{exp},i}$ (%)	5.512	2.044
$RMSE = \sqrt{1/n \sum_{i=1}^{n} (\eta_{\mathrm{calc},i} - \eta_{\mathrm{exp},i})^2}$	0.039	0.011
$MAD = \mathrm{Max}\lvert\eta_{\mathrm{calc},i} - \eta_{\mathrm{exp},i}\rvert$	0.073	0.016

Table 3.3 reports the percentage absolute average deviation AAD, the root-mean-square error $RMSE$, and the maximum absolute deviation MAD between calculated and experimental points. For both the prototypes, the model tends to be conservative underestimating the thermal efficiency.

Since the key parameter which influences a nanofluid-based PTC efficiency is the convective heat transfer coefficient, an accurate measurement of this quantity was carried out by means of a dedicated experimental apparatus. The details of the apparatus are provided in [93]. The geometry of the apparatus consists of a pipe, which is suitable to reproduce a PTC receiver. Furthermore, the measurements of the convective heat transfer coefficient for the considered nanofluids are predicted quite well by the equations of the literature, in particular by the Gnielinski's correlation [60], with an AAD of about 5%. Thus, this equation was used in the simulation environment to calculate the convective heat transfer coefficient of the proposed nanofluids.

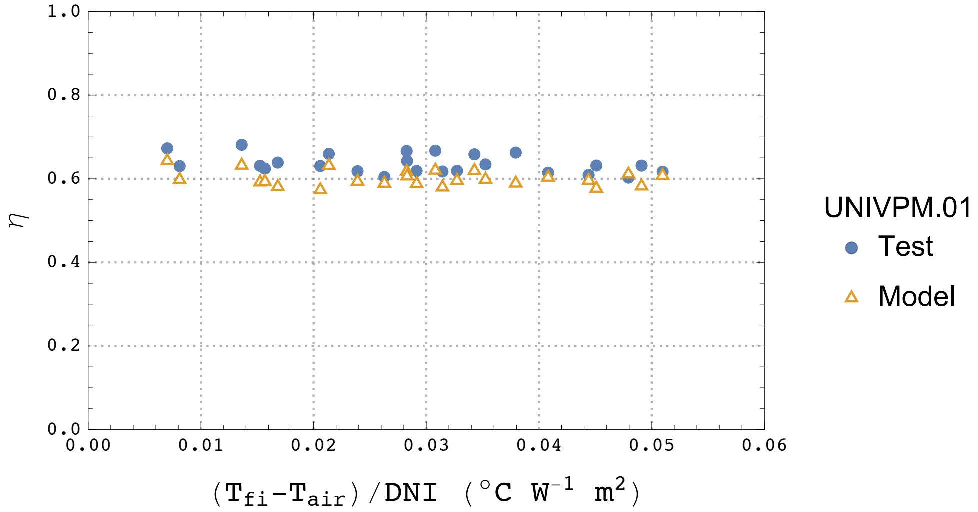

Figure 3.6: Calculated and experimental results for UNIVPM.01.

3.4 Simulation Initialization

The amount of useful energy that can be produced by a PTC for the entire simulated period of one year was calculated by: 1) defining a meteorological database that contains the necessary environmental inputs; 2) defining a profile of the heat demand load; 3) calculating the amount of energy that a PTC field can produce in a given location at different environmental and working conditions.

The employment of a steady-state model implies that a simulation for a certain time period will be the succession of several simulations on fractions of this period: time steps were considered equal to one hour. Variables affected by potential errors due to the assumption of steady-state conditions are mainly heat demand characteristics and meteorological data. Referring to the former, time periods of one hour are substantially correct since the heat demand profile is practically constant in the selected heat demand curve (as will be discussed in Section 3.4.3).

On the other hand, it is not possible to easily reach the same conclusion about meteorological data. However, time resolution of available meteorological databases is limited (the best available databases present steps of fifteen minutes [100]), therefore transient phenomena could not be represented in a proper way with a more sophisticated model. Thus, a one-hour-resolution model can be considered acceptable and a yearly simulation consists of a sequence of 8760 one-hour-steady-state simulations.

3.4.1 Typical Meteorological Year

Historical hourly measurements of ambient temperature, wind velocity, and relative humidity in the form of multi-year collections exist for a lot of Italian locations measured by several networks of weather stations. On the other hand, solar radiation data, and in particular direct normal radiation data, are available for a very limited set of locations: in fact, the collection of this kind of measurements is not a simple task due to the extreme complexity and variability of the radiative phenomenon.

To overcome the lack of ground measured data, collections of historical series of satellite images were used for the purpose of this work. In particular, to have a

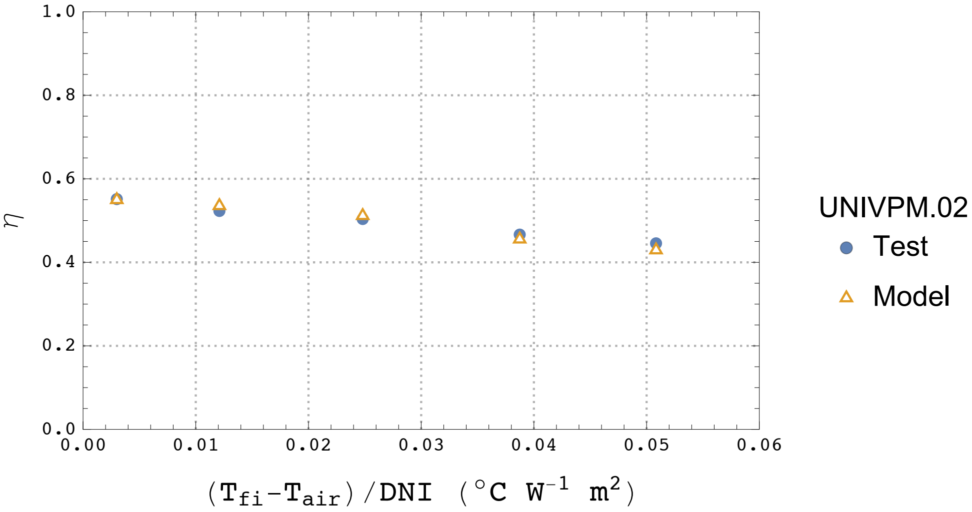

Figure 3.7: Calculated and experimental results for UNIVPM.02.

reasonable statistical validity, it is not possible to collect data for one year only, but it is necessary to build a so-called TMY (Typical Meteorological Year), i.e., a year that is representative of the real conditions in terms of their variability, irregularity, and unpredictability. Given these assumptions, a TMY can be obtained only when several years of data have been collected (usually periods longer than six years [100]).

For the city of Ancona (eastern coast of central Italy), the TMY was composed based on solar radiation data prepared by ENEA (Italian National Agency for New Technologies, Energy and Sustainable Economic Development). The most representative months in terms of *DNI* were chosen from a six-years database. The other meteorological variables (ambient temperature, wind velocity, and relative humidity) were collected from the Wunderground Meteorological Database [101] for a location sufficiently close to that of the present elaboration. Therefore, the meteorological input for the simulation environment consists of a table with 8760 rows, where each row represents a hour of the TMY for the chosen location.

The main characteristics of the TMY used for the simulation are provided in Table 3.4. The TMY months are chosen based on the analysis of *DNI* only because this quantity is strictly related to the energy that will be collected by the PTC.

3.4.2 PTC Field Arrangement

To define the amount of exploitable energy that a PTC field can deliver to a process, it is necessary to know the PTC field characteristics, the process heat demand profile, and the way the former and the latter are connected. Starting from the former, the choice of the dimensions of the PTC field is driven by two aspects [44]:

1. the discontinuity of the solar source is such that it is generally impossible to satisfy a heat load with the solar source only;

2. in the case of process heat demand loads, solar plants are likely to be positioned on building roofs, therefore the amount of surface that can be dedicated to the PTC field is generally limited.

Table 3.4: Composition of the TMY for Ancona (Italy). The monthly values of the global radiation on horizontal plane, H, and of the beam normal radiation, H_{bn}, are referred to the average day. The total values indicate the overall yearly energy calculated for the TMY.

Month	Year (TMY)	H (kWh/m^2)	H_{bn} (kWh/m^2)	$T_{\mathrm{air,m}}$ (°C)	$v_{\mathrm{air,m}}$ (m/s)
January	2009	1.18	1.00	5.36	2.61
February	2011	2.31	2.76	6.34	3.31
March	2008	3.37	3.70	10.31	3.30
April	2011	5.23	5.54	14.26	2.60
May	2006	6.06	5.79	17.57	2.06
June	2006	6.66	6.50	21.35	2.24
July	2007	7.12	7.56	25.16	2.59
August	2010	5.98	6.43	23.43	2.75
September	2007	4.23	4.46	18.45	2.76
October	2009	2.72	3.14	14.78	2.80
November	2008	1.76	2.17	10.33	2.61
December	2008	1.18	1.29	6.44	2.80
Total		1457	1534		

Given these two conditions, if the base load of the heat demand profile is large enough, a smart choice is to dimension the PTC field to a value smaller than the heat demand base load. Thus, no thermal storage is needed. This condition generally matches with the second observation, i.e., that a PTC field which uses the entire available roof or a large part of it will probably have a size close to that defined by the base load of the heat demand profile.

A possible connection scheme that satisfies the aforementioned conditions is reported in Figure 3.8. This scheme has three important advantages:

- The mass flow rate across the PTC field can be set to any value lower than that of the total flow. Also, no flow can be sent to the field in the moments of absence of solar source simply using the diverter valve.

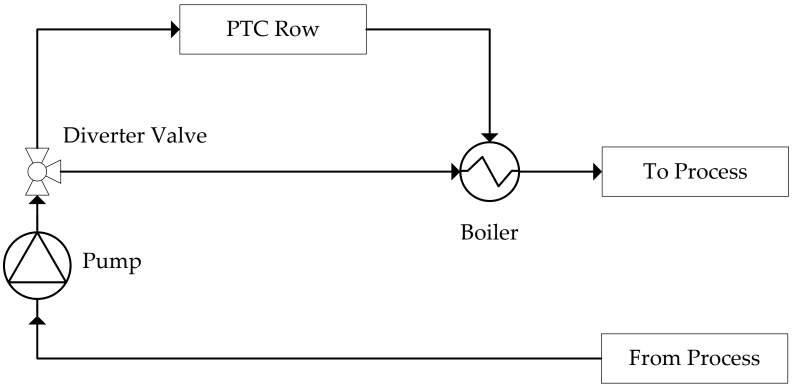

Figure 3.8: A possible connection scheme for the PTC field.

Table 3.5: Geometry and properties of the PTC field materials used in the simulation.

Input	Symbol	Value
Mirror length (m)	L_{m}	12.85
Mirror aperture (m)	W_{m}	2.500
Receiver length (m)	L_{r}	13.25
Inner abs. diam. (m)	D_{ai}	0.035
Outer abs. diam. (m)	D_{ao}	0.040
Inner cover diam. (m)	D_{ci}	0.046
Outer cover diam. (m)	D_{co}	0.048
Focal distance (m)	f	0.550
Mirr. specular reflectance	r	0.94
Extinction coeff. (1/m)	K	10
Cover cond. (W/(m K))	λ_{c}	1.40
Cover emissivity	ϵ_{c}	0.86
Norm. abs. absorptance	α_{n}	0.90
Abs. cond. (W/(m K))	λ_{a}	60
Abs. emissivity	ϵ_{a}	0.30
Abs. roughness (µm)	ξ	50

- It allows a certain modularity of the plant. In fact, it will be possible to increase the dimensions of the PTC field by simply adding one or more rows.

- There are less tight requirements on delivery temperature respect to other possible connection schemes. If the fraction of energy produced by the PTC field is limited, then an increase or a decrease in the temperature of the fluid reintroduced in the main circuit will be automatically corrected by the boiler.

Referring again to Figure 3.8, one row having an aperture area equal to $32.125\,\mathrm{m}^2$ was considered. This row was obtained by allying 5 collectors having a mirror length of 2.570 m, for a total mirror length of 12.85 m. All remaining parameters necessary to completely define the PTC field used in the simulation environment are provided in Table 3.5. It is also worth noting that: a) the PTC axis has a horizontal north-south orientation (i.e., there is a east-west tracking); b) a selective coating was used to reduce radiative thermal losses from the absorber tube; c) the receiver is shielded but not evacuated.

3.4.3 Heat Demand Profile

Once the TMY and the characteristics of the PTC have been defined, the remaining necessary data regard the heat demand curve description. Both in the case of a plant with a thermal storage or not, the basis of the simulation is the knowledge of the process characteristics: the adopted HTF, its inlet temperature T_{fi} and pressure p, and the mass flow rate $\dot{m}$.

The set of the inlet fluid temperature requires the definition of a precise thermal process. For the simulation presented in this work, a low-temperature process was considered, using water and water-based nanofluids as HTFs at atmospheric pressure and at a fixed inlet temperature. To evaluate how the temperature influences the

Table 3.6: An extract of the heat demand profile. This example is valid for water as HTF.

Day-Month	Year (TMY)	Hour (GMT)	T_{fi} (°C)	p (bar)	$\dot{m}$ (kg/s)
01-01	2009	00:30	70	1	0.50
01-01	2009	01:30	70	1	0.50
01-01	2009	02:30	70	1	0.50
31-12	2008	21:30	70	1	0.50
31-12	2008	22:30	70	1	0.50
31-12	2008	23:30	70	1	0.50

performance of nanofluids respect to water, the simulation was carried out for 5 different inlet fluid temperatures: 40, 50, 60, 70, and 80 °C.

The mass flow rate was kept constant and equal to 0.50 kg/s. This value guarantees that:

- a turbulent regime is ensured in the absorber tube in the worst condition, i.e., when the HTF is TiO_2+H_2O 35 wt% which presents the highest dynamic viscosity and density;
- vaporization is avoided in the absorber tube in the worst condition, i.e., when the HTF is, again, TiO_2+H_2O 35 wt%, as it presents the lowest specific heat at constant pressure.

Even though the thermophysical properties of the considered fluids are not influenced by the mass flow rate, additional simulations were carried out in order to evaluate the effect of the mass flow rate on the yearly yield. To achieve this goal, the inlet fluid temperature was kept constant at 80 °C; in fact this temperature, among those considered, is the most relevant for thermal applications. Therefore, in addition to 0.5 kg/s, other two mass flow rate values were analyzed at 80 °C: 1 kg/s and 1.5 kg/s.

The adopted PTC field works 24 hours a day throughout the TMY. Although the model is able to take into account the effect of stops and/or maintenance works, they were not considered in this work. The heat demand profile of the input block Process (Section 3.3.1) is, therefore, a matrix such as that provided in Table 3.6.

3.5 Results and Discussion

Once all the inputs discussed in the previous sections are well-defined and the simulation is complete, every unknown quantity involved in the physical-mathematical model is known. In this work, we are interested in evaluating and comparing the yearly energy for unit of aperture area, E, produced by the PTC field when the investigated nanofluids are adopted as HTF. In particular, the main aim of this analysis is to find nanofluids with yearly yields greater than water; thus, water was considered as a baseline.

For a mass flow rate fixed at 0.5 kg/s, Table 3.7 and 3.8 report the yearly energy deliverable by the PTC field for an inlet fluid temperature equal to 40 °C and 80 °C, which are the minimum and the maximum temperature investigated, respectively. For an entire TMY:

$$\Delta E\% = 100\,\frac{E_{\text{nf}} - E_{\text{H}_2\text{O}}}{E_{\text{H}_2\text{O}}} \tag{3.9}$$

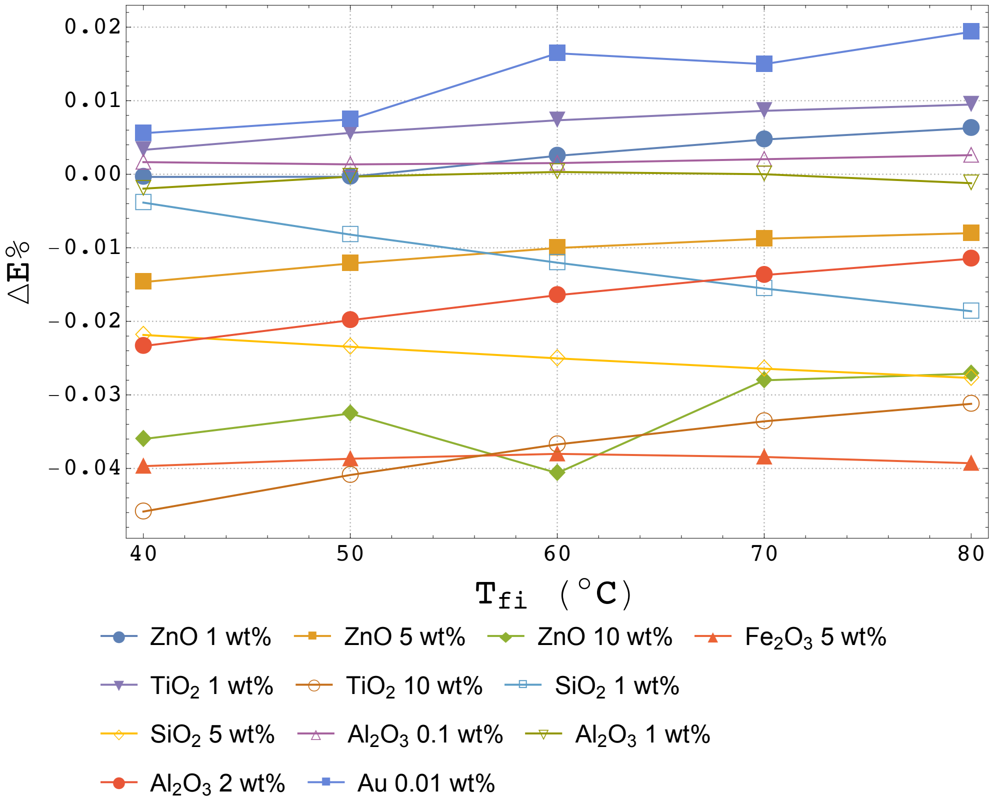

Figure 3.9: Yearly energy difference $\Delta E\%$ as a function of the inlet fluid temperature T_{fi} for the best concentrations of investigated nanofluids. The mass flow rate is equal to 0.5 kg/s.

where E_{nf} and $E_{\mathrm{H_2O}}$ are the yearly yields delivered by nanofluids and water, respectively. Furthermore, Figure 3.9 depicts the yearly energy difference $\Delta E\%$ as a function of the inlet fluid temperature T_{fi} for the best investigated nanofluids ($\dot{m} = 0.5\,\mathrm{kg/s}$). Figure 3.10, instead, shows how the same quantity varies at $T_{\mathrm{fi}} = 80\,^{\circ}\mathrm{C}$ for different mass flow rate values.

The results are quite disconcerting. Only four reduced concentrations give a yearly yield better than that of water: ZnO at 1 wt%, TiO_2 at 1 wt%, Al_2O_3 at 0.1 wt%, and Au at 0.01 wt%. However, improvements in terms of yearly yield are very low.

The obtained results could be explained by considering several aspects. Firstly, we have to focus our attention to the convective heat transfer coefficient $h_{\mathrm{c,af}}$, which regulates the corresponding heat transfer between the absorber and the heat transfer fluid $Q_{\mathrm{c,af}}$. Since the Gnielinski's correlation [60] was found to predict with good accuracy the measurements of the convective heat transfer coefficient of the proposed nanofluids (with an AAD of about 5% [93]), this equation was used to evaluate the convective heat transfer coefficient. The Gnielinski's correlation is:

$$h_{\mathrm{c,af}} = \frac{\lambda_{\mathrm{f}}}{D_{\mathrm{ai}}} Nu = \frac{\lambda_{\mathrm{f}}}{D_{\mathrm{ai}}} \left[\frac{(\zeta/8)\,(Re - 1000)\,Pr}{1 + 12.7(\zeta/8)^{1/2}\left(Pr^{2/3} - 1\right)} \right] \tag{3.10}$$

where λ_{f} is the thermal conductivity of the fluid, Nu is the Nusselt number, Re is the

Table 3.7: Monthly and yearly yield for the investigated heat transfer fluids at an inlet fluid temperature of 40 °C and mass flow rate of 0.5 kg/s.

HTF	Monthly yield (MJ/m^2)												Total	ΔE%
	1	2	3	4	5	6	7	8	9	10	11	12	(MJ/m^2)	
H_2O	25.80	96.87	197.00	326.77	382.28	425.81	511.09	414.68	247.39	143.65	66.36	29.03	2866.72	
TiO_2 1 wt%	25.80	96.88	197.01	326.78	382.30	425.82	511.10	414.70	247.39	143.65	66.36	29.03	2866.82	0.003
TiO_2 10 wt%	25.79	96.82	196.91	326.61	382.11	425.62	510.87	414.50	247.27	143.58	66.32	29.01	2865.41	-0.046
TiO_2 20 wt%	25.77	96.74	196.75	326.66	381.82	425.31	510.50	414.19	247.09	143.47	66.27	28.99	2863.56	-0.110
TiO_2 35 wt%	25.71	96.53	196.33	325.67	381.06	424.47	509.52	413.36	246.59	143.17	66.13	28.93	2857.48	-0.323
SiO_2 1 wt%	25.80	96.87	196.99	326.76	382.27	425.79	511.07	414.67	247.38	143.64	66.35	29.03	2866.61	-0.004
SiO_2 5 wt%	25.80	96.85	196.96	326.69	382.20	425.72	510.98	414.59	247.33	143.62	66.34	29.02	2866.10	-0.022
SiO_2 25 wt%	25.75	96.66	196.59	326.09	381.52	424.98	510.12	413.86	246.89	143.36	66.22	28.97	2861.01	-0.199
Fe_2O_3 5 wt%	25.79	96.83	196.92	326.63	382.13	425.65	510.90	414.52	247.29	143.59	66.33	29.02	2865.58	-0.040
Fe_2O_3 10 wt%	25.78	96.78	196.83	326.48	381.96	425.46	510.68	414.34	247.18	143.52	66.30	29.00	2864.31	-0.084
Fe_2O_3 20 wt%	25.74	96.65	196.56	326.05	381.48	424.93	510.06	413.82	246.86	143.34	66.21	28.96	2860.67	-0.211
ZnO 1 wt%	25.80	96.87	196.99	326.76	382.27	425.80	511.07	414.67	247.38	143.64	66.35	29.03	2866.62	-0.004
ZnO 5 wt%	25.80	96.86	196.97	326.72	382.23	425.75	511.02	414.62	247.35	143.63	66.35	29.02	2866.30	-0.015
ZnO 10 wt%	25.79	96.83	196.93	326.65	382.15	425.66	510.91	414.54	247.30	143.59	66.33	29.02	2865.69	-0.036
Al_2O_3 0.1 wt%	25.80	96.88	197.01	326.77	382.29	425.82	511.10	414.69	247.39	143.65	66.36	29.03	2866.77	0.002
Al_2O_3 1 wt%	25.80	96.87	196.99	326.75	382.27	425.79	511.07	414.67	247.37	143.64	66.35	29.03	2866.60	-0.004
Al_2O_3 2 wt%	25.80	96.86	196.97	326.72	382.23	425.75	511.02	414.62	247.35	143.62	66.35	29.02	2866.29	-0.015
Au 0.01 wt%	25.80	96.88	197.01	326.79	382.30	425.83	511.11	414.71	247.40	143.66	66.36	29.03	2866.88	0.006

Table 3.8: Monthly and yearly yield for the investigated heat transfer fluids at an inlet fluid temperature of 80 °C and mass flow rate of 0.5 kg/s.

HTF	Monthly yield (MJ/m^2) 1	2	3	4	5	6	7	8	9	10	11	12	Total (MJ/m^2)	ΔE%
H_2O	20.96	86.71	183.94	309.13	361.91	404.31	487.74	393.32	231.89	132.19	57.02	23.67	2692.80	
TiO_2 1 wt%	20.96	86.72	183.96	309.16	361.95	404.35	487.79	393.36	231.92	132.20	57.02	23.67	2693.06	0.010
TiO_2 10 wt%	20.95	86.69	183.89	309.03	361.80	404.19	487.59	393.20	231.82	132.15	57.00	23.66	2691.96	-0.031
TiO_2 20 wt%	20.94	86.62	183.76	308.81	361.55	403.91	487.26	392.92	231.66	132.05	56.96	23.65	2690.08	-0.101
TiO_2 35 wt%	20.90	86.46	183.41	308.23	360.90	403.18	486.39	392.20	231.24	131.81	56.86	23.60	2685.17	-0.283
SiO_2 1 wt%	20.95	86.70	183.91	309.07	361.85	404.24	487.65	393.25	231.85	132.16	57.01	23.67	2692.30	-0.018
SiO_2 5 wt%	20.95	86.69	183.89	309.04	361.82	404.20	487.61	393.21	231.83	132.15	57.00	23.67	2692.06	-0.027
SiO_2 25 wt%	20.91	86.52	183.54	308.45	361.14	403.45	486.71	392.47	231.40	131.90	56.90	23.62	2687.02	-0.215
Fe_2O_3 5 wt%	20.95	86.68	183.87	309.00	361.77	404.16	487.55	393.16	231.80	132.14	57.00	23.66	2691.75	-0.039
Fe_2O_3 10 wt%	20.94	86.64	183.78	308.85	361.60	403.97	487.33	392.98	231.70	132.07	56.97	23.65	2690.48	-0.086
Fe_2O_3 20 wt%	20.92	86.55	183.60	308.55	361.26	403.59	486.88	392.60	231.48	131.95	56.91	23.63	2687.92	-0.181
ZnO 1 wt%	20.96	86.72	183.96	309.15	361.94	404.34	487.77	393.35	231.91	132.20	57.02	23.67	2692.97	0.007
ZnO 5 wt%	20.96	86.71	183.93	309.10	361.89	404.28	487.70	393.29	231.88	132.18	57.01	23.67	2692.59	-0.008
ZnO 10 wt%	20.95	86.69	183.89	309.04	361.82	404.21	487.61	393.21	231.83	132.15	57.00	23.67	2692.07	-0.027
Al_2O_3 0.1 wt%	20.96	86.72	183.95	309.13	361.92	404.33	487.75	393.33	231.90	132.19	57.02	23.67	2692.87	0.003
Al_2O_3 1 wt%	20.96	86.71	183.94	30912	361.90	404.30	487.73	393.31	231.89	132.19	57.02	23.67	2692.73	-0.003
Al_2O_3 2 wt%	20.96	86.71	183.93	309.11	361.90	404.29	487.71	393.30	231.88	132.18	57.0	23.67	2692.65	-0.005
Au 0.01 wt%	20.96	86.73	183.98	309.19	361.98	404,39	487.83	393.40	231.94	132.21	57.03	23.68	2693.33	0.020

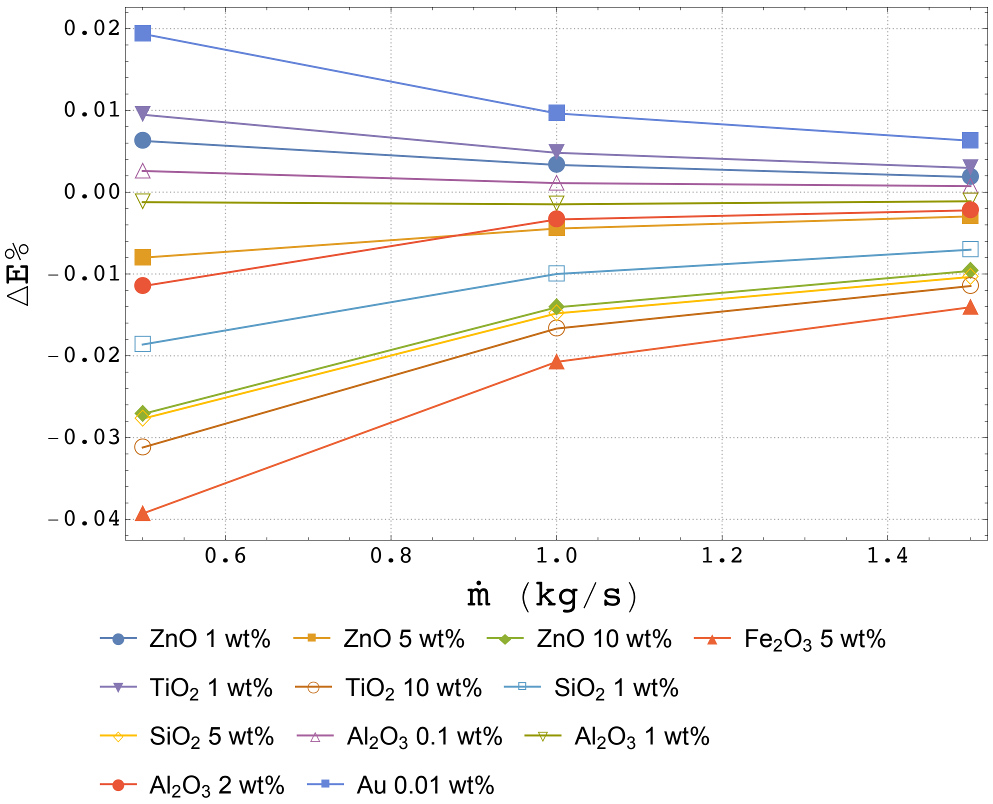

Figure 3.10: Yearly energy difference $\Delta E\%$ as a function of the mass flow rate for the best concentrations of investigated nanofluids. The inlet fluid temperature is 80 °C.

Reynolds number and Pr is the Prandtl number. The friction factor ζ was calculated with the Colebrook's iterative formula [61]:

$$\frac{1}{\sqrt{\zeta}} = -2\log\left(\frac{\xi/D_{\mathrm{ai}}}{3.71} + \frac{2.51}{Re\sqrt{\zeta}}\right) \tag{3.11}$$

where ξ is the absorber roughness. For the proposed heat transfer fluids, Figure 3.11 shows the trend of $h_{\mathrm{c,af}}$ as a function of the inlet fluid temperature (at a fixed mass flow rate of 0.5 kg/s). Looking at Figure 3.11 and reminding the concentrations that gave positive results, it is possible to note that a larger number of fluids show a $h_{\mathrm{c,af}}$ higher than that of water, at least for the highest temperatures. This unexpected behavior depends on the mathematical model structure of the simulation environment.

In Section 3.3.4, we said that an iterative process was necessary to correctly evaluate the convective heat transfers in the receiver. At the first iteration, the mean fluid temperature, T_{mf}, is considered equal to the inlet fluid temperature, T_{fi}. Thus, if a nanofluid presents a convective heat transfer coefficient larger than water, the useful heat gain, Q_{u}, will be higher respect to water (see Figure 3.4 and System (3.7): $Q_{\mathrm{c,af}}$ corresponds to Q_{u}). Since the specific heat at constant pressure c_p of the proposed nanofluids is always lower than that of water, then, from Equation (3.8), the outlet fluid temperature T_{fo} will be greater respect to water. Therefore, at the second iteration the new T_{mf} will be greater for the aforementioned nanofluids and, as a consequence, there

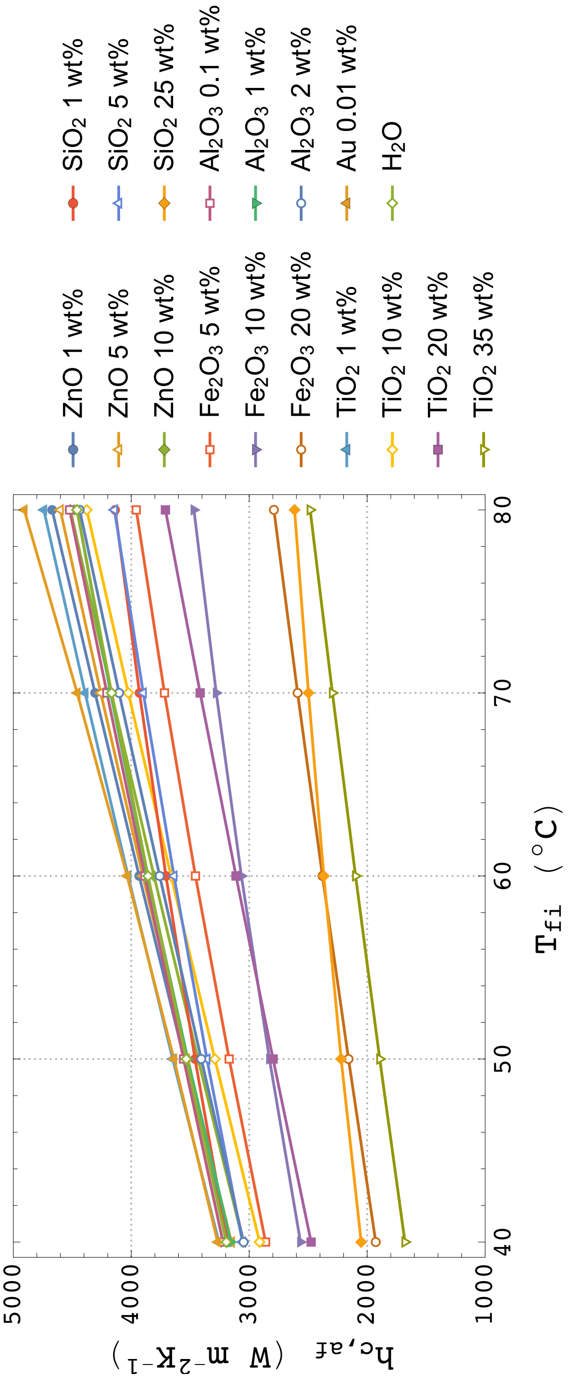

Figure 3.11: Convective heat transfer coefficient $h_{\mathrm{c,af}}$ as a function of the inlet fluid temperature T_{fi} for the investigated HTFs. The mass flow rate is equal to 0.5 kg/s.

will be greater thermal losses from the receiver to the environment. This explains why several nanofluids have a $h_{\mathrm{c,af}}$ higher than water, but show a worse yearly yield, as depicted in Figure 3.9: the small increase in $h_{\mathrm{c,af}}$ is not able to balance the greater thermal losses.

On the other hand, the value assumed by the convective heat transfer coefficient is crucial to obtain higher thermal efficiencies and depends on the thermo-physical properties of the considered HTFs. To better understand how the fluid properties influence $h_{\mathrm{c,af}}$, a simplified analysis will be carried out. Let us consider the Dittus-Boelter equation [102], which is simpler to manipulate respect to Gnielinski (Equation (3.10)) and Colebrook (Equation (3.11)) correlations actually used in the model of the this work:

$$h_{\mathrm{c,af}} = \frac{\lambda_{\mathrm{f}} Nu}{D_{\mathrm{ai}}} = \frac{0.023\, \lambda_{\mathrm{f}} Re^{0.8} Pr^{0.4}}{D_{\mathrm{ai}}} \tag{3.12}$$

We also have $Re = (\rho_{\mathrm{f}} v_{\mathrm{f}} D_{\mathrm{ai}})/\mu_{\mathrm{f}}$ and $Pr = (\mu_{\mathrm{f}} c_{p,\mathrm{f}})/\lambda_{\mathrm{f}}$, where v_{f} is the fluid velocity in the absorber tube. Since the geometry (D_{ai}) is fixed in the simulation, we obtain from the mass conservation:

$$v_{\mathrm{f}} = \frac{\dot{m}}{\frac{\pi D_{\mathrm{ai}}^2}{4} \rho_{\mathrm{f}}} \propto \frac{\dot{m}}{\rho_{\mathrm{f}}} \tag{3.13}$$

Therefore, Equation (3.12) becomes:

$$h_{\mathrm{c,af}} \propto \lambda_{\mathrm{f}} \left(\frac{\dot{m}}{\mu_{\mathrm{f}}}\right)^{0.8} \left(\frac{\mu_{\mathrm{f}}\, c_{p,\mathrm{f}}}{\lambda_{\mathrm{f}}}\right)^{0.4} = \frac{\dot{m}^{0.8}\, \lambda_{\mathrm{f}}^{0.6}\, c_{p,\mathrm{f}}^{0.4}}{\mu_{\mathrm{f}}^{0.4}} \tag{3.14}$$

We found that the convective heat transfer coefficient increases with the mass flow rate, the specific heat and the thermal conductivity, and decreases with dynamic viscosity. Considering that the specific heat of the proposed nanofluids is always lower than that of water, for a fixed mass flow rate high thermal conductivities and low dynamic viscosities are required to obtain convective heat transfer coefficients larger than those of water. This condition is satisfied only at high temperatures. In fact, when the temperature increases, the thermal conductivity grows (Figure 3.2) while the dynamic viscosity drops (Figure 3.3). This trend is confirmed by referring to Figure 3.9: the convenience in adopting nanofluids seems to enlarge for higher temperatures.

The role of the weight concentration should also be taken into account. The dynamic viscosity tends to enlarge significantly with weight concentration (Figure 3.3), more than the thermal conductivity (Figure 3.2). This behavior explains why enhancements were obtained only for reduced quantities of nanoparticles. In addition, it is worth noting that a larger viscosity does not only penalize the thermal efficiency, but also contributes to increase the work required by the pumping system. However, this effect was not considered in the simulation.

The effect of the mass flow rate on the yearly yield is a bit more complex to explain. Nanofluids with higher concentrations of nanoparticles are more viscous (the convective heat transfer is lower than that of water) and present a lower thermal capacity compared to water; thus, they have higher mean fluid temperature and thermal losses. The combined effect of lower convective heat transfer coefficients and greater thermal losses explain their reduced yearly yield respect to water. If the mass flow rate increases, the mean fluid temperature (and then thermal losses) tends to decrease. Even though the convective heat transfer coefficient worsens (respect to water) because of the lower temperature, in any case the yearly yield, compared to water, increases as the reduction of thermal losses is more significant than that of the convective heat transfer coefficient.

This explains the trend reported in Figure 3.10 for all the nanofluids with higher concentrations.

On the contrary, nanofluids with lower concentration of nanoparticles have a smaller dynamic viscosity (the convective heat transfer coefficient is higher), and their thermal capacity is similar to that of water; therefore, the mean fluid temperature and thermal losses are comparable to those of water. In this case, when the mass flow rate is increased, thermal losses decrease as the mean fluid temperature drops, but the convective heat transfer coefficient considerably worsens respect to water: this explains why these nanofluids have a lower yield (compared to water) when the mass flow rate enlarges (Figure 3.10).

Finally, Figure 3.12 shows how the inlet fluid temperature influences the yearly yield of TiO_2+H_2O at 1 wt%, one of the four concentrations that showed the best results. When the HTF temperature increases, the yearly yield falls off because the thermal losses between the receiver and the environment are greater. This situation could represent a potential advantage for nanofluids since, as depicted in Figure 3.9, the performances of such fluids tend to improve at higher temperatures respect to water.

In addition, for each considered case, Table 3.9 and 3.10 report the maximum temperature reached by the studied HTFs and the corresponding thermal efficiency. Results are referred to May 28, 2006 at 09:30 GMT, which is the TMY hour with the best environmental conditions ($T_{\text{air}} = 28\,°\text{C}$, $DNI = 846.06\,\text{W/m}^2$, $\theta = 18.92°$, $RH = 48\,\%$, and $w_{\text{air}} = 1.56\,\text{m/s}$). As can be noted in Table 3.10, for each HTF the thermal efficiency increases with the mass flow rate: this occurs because the convective heat transfer coefficient is proportional to the mass flow rate (Equation (3.14)). It is also possible to note that the relative difference in thermal efficiency between nanofluids and water worsens for low-concentration nanofluids and improves for high-concentration nanofluids for higher mass flow rates, as explained above and visible in Figure 3.10: e.g., from 0.5 kg/s to 1.5 kg/s, the Au 0.01 wt% efficiency varies from 0.0091% to 0.0031% respect to water, while for a high-concentration nanofluid such as TiO_2 35 wt%, the variation is from -0.2654% to -0.0948%.

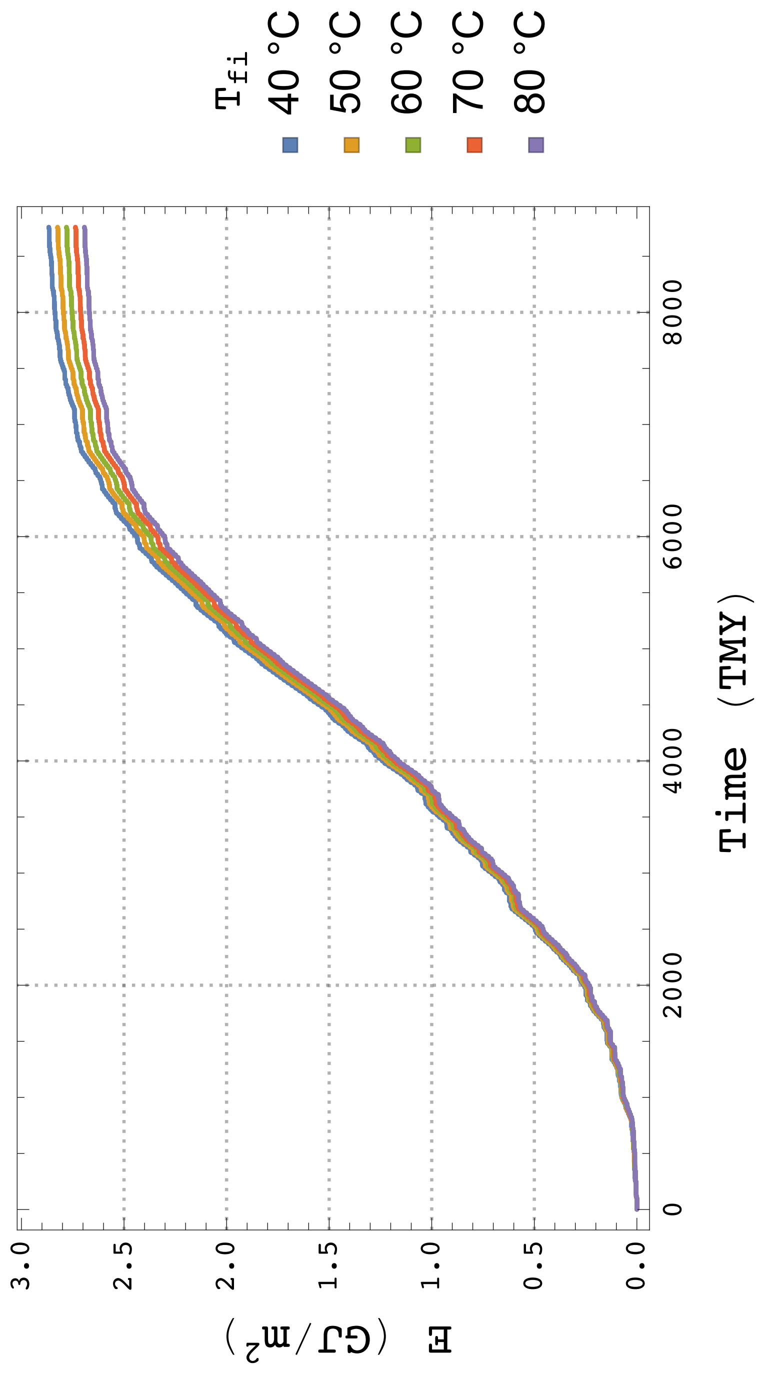

Figure 3.12: Yearly yield of TiO_2+H_2O at 1 wt% for the investigated inlet fluid temperatures ($\dot{m} = 0.5\,\mathrm{kg/s}$).

Table 3.9: Maximum outlet fluid temperature and corresponding thermal efficiency for the cases 40, 50, 50 and 70 °C at 0.5 kg/s. Results are referred to 28/05/2006 at 09:30 GMT.

HTF	40 °C		50 °C		60 °C		70 °C	
	$T_{\mathrm{fo,max}}$(°C)	$\eta(T_{\mathrm{fo,max}})$	$T_{\mathrm{fo,max}}$(°C)	$\eta(T_{\mathrm{fo,max}})$	$T_{\mathrm{fo,max}}$(°C)	$\eta(T_{\mathrm{fo,max}})$	$T_{\mathrm{fo,max}}$(°C)	$\eta(T_{\mathrm{fo,max}})$
H_2O	47.79	63.14%	57.73	62.73%	67.67	62.30%	77.61	61.85%
TiO_2 1 wt%	47.85	63.14%	57.80	62.74%	67.74	62.30%	77.67	61.85%
TiO_2 10 wt%	48.49	63.12%	58.43	62.71%	68.36	62.28%	78.29	61.83%
TiO_2 20 wt%	49.33	63.07%	59.26	62.67%	69.19	62.24%	79.11	61.79%
TiO_2 35 wt%	50.94	62.96%	60.87	62.55%	70.78	62.13%	80.69	61.68%
SiO_2 1 wt%	47.85	63.14%	57.79	62.73%	67.73	62.29%	77.66	61.84%
SiO_2 5 wt%	48.09	63.13%	58.04	62.72%	67.97	62.29%	77.90	61.83%
SiO_2 25 wt%	49.60	63.03%	59.53	62.61%	69.45	62.18%	79.37	61.73%
Fe_2O_3 5 wt%	48.13	63.12%	58.07	62.71%	68.01	62.28%	77.94	61.83%
Fe_2O_3 10 wt%	48.50	63.09%	58.44	62.68%	68.38	62.25%	78.30	61.80%
Fe_2O_3 20 wt%	49.36	63.02%	59.30	62.62%	69.22	62.19%	79.14	61.74%
ZnO 1 wt%	47.86	63.14%	57.80	62.73%	67.74	62.30%	77.67	61.85%
ZnO 5 wt%	48.14	63.13%	58.08	62.73%	68.02	62.29%	77.95	61.84%
ZnO 10 wt%	48.53	63.12%	58.47	62.71%	68.40	62.28%	78.33	61.83%
Al_2O_3 0.1 wt%	47.79	63.14%	57.74	62.73%	67.68	62.30%	77.61	61.85%
Al_2O_3 1 wt%	47.85	63.14%	57.79	62.73%	67.73	62.30%	77.67	61.85%
Al_2O_3 2 wt%	47.91	63.13%	57.85	62.73%	67.79	62.30%	77.73	61.85%
Au 0.01 wt%	47.79	63.15%	57.73	62.74%	67.67	62.31%	77.61	61.86%

Table 3.10: Maximum outlet fluid temperature and corresponding thermal efficiency for the cases 0.5, 1, and 1.5 kg/s at 80 °C. Results are referred to 28/05/2006 at 09:30 GMT.

HTF	0.5 kg/s		1 kg/s		1.5 kg/s	
	$T_{\mathrm{fo,max}}(^{\circ}\mathrm{C})$	$\eta(T_{\mathrm{fo,max}})$	$T_{\mathrm{fo,max}}(^{\circ}\mathrm{C})$	$\eta(T_{\mathrm{fo,max}})$	$T_{\mathrm{fo,max}}(^{\circ}\mathrm{C})$	$\eta(T_{\mathrm{fo,max}})$
H_2O	87.54	61.38%	83.78	61.53%	82.52	61.58%
TiO_2 1 wt%	87.60	61.39%	83.81	61.53%	82.54	61.58%
TiO_2 10 wt%	88.21	61.37%	84.12	61.52%	82.75	61.57%
TiO_2 20 wt%	89.03	61.33%	84.53	61.50%	83.02	61.56%
TiO_2 35 wt%	90.59	61.22%	85.32	61.44%	83.55	61.52%
SiO_2 1 wt%	87.58	61.37%	83.80	61.52%	82.54	61.57%
SiO_2 5 wt%	87.82	61.37%	83.92	61.52%	82.62	61.57%
SiO_2 25 wt%	89.27	61.26%	84.65	61.46%	83.11	61.53%
Fe_2O_3 5 wt%	87.86	61.36%	83.94	61.52%	82.63	61.57%
Fe_2O_3 10 wt%	88.22	61.33%	84.12	61.50%	82.75	61.56%
Fe_2O_3 20 wt%	89.05	61.28%	84.54	61.47%	83.03	61.54%
ZnO 1 wt%	87.61	61.39%	83.82	61.53%	82.55	61.58%
ZnO 5 wt%	87.89	61.38%	83.95	61.53%	82.64	61.58%
ZnO 10 wt%	88.26	61.37%	84.14	61.52%	82.76	61.57%
Al_2O_3 0.1 wt%	87.54	61.38%	83.78	61.53%	82.52	61.58%
Al_2O_3 1 wt%	87.60	61.38%	83.81	61.53%	82.54	61.58%
Al_2O_3 2 wt%	87.66	61.38%	83.84	61.53%	82.56	61.58%
Au 0.01 wt%	87.54	61.39%	83.78	61.53%	82.52	61.58%

Chapter 4

Solar Box Cooker Prototype: Design, Manufacture, and Test

Since solar cooking is considered as one of the simplest and attractive ways of the utilization of solar energy, a solar box cooker prototype was manufactured and tested in DIISM (Department of Industrial Engineering and Mathematical Sciences). The prototype, based on a freeware design, was modified to improve its most relevant optical elements: booster mirrors, double glass cover, absorbing paint, and thermal insulation. The solar box cooker characteristics and manufacturing process are described in detail. Then, a test bench used to characterize the cooker performance is presented. Experimental tests with and without load were carried out. While the latter allowed to find the maximum temperature achievable by the solar oven, the former are necessary to determine its thermal efficiency. Different load combinations were tested: black-painted and non-painted vessels, one and two vessels, water and peanut oil. Results show that the cooker is able to cook at high temperature and its performance is aligned with other cookers in literature.

4.1 Solar Box Cookers in Literature

In the last thirty years, research involving solar box cookers has focused on the optimization of geometrical parameters, as they seem to have a relevant effect on performance [6]. Booster mirrors can be utilized to increase the efficiency of solar box cookers as they provide additional solar radiation; their effectiveness depends on the angle of the mirrors. Rao et al. [103] proved that the total energy falling on the the cooking aperture of a solar box cooker was enhanced at all hours of the day by intermittent, continuous, and fixed adjustment of the supporting mirror. Rectangular apertures were found to be more effective than square ones. In addition, the contribution of the booster mirror became more and more significant with an increase in latitude [104]. Habeebullah et al. [105] proposed an oven type concept in order to minimize the amount of heat losses and found that if the box cooker is augmented with four booster mirrors, heat losses due to wind will reduce as this one will be obstructed by the mirrors.

Various glazing materials such as glass, fiberglass, and acrylic are commonly used in solar box cookers. Optimization of the gap between panes is an important matter as large air gaps may cause convective heat losses. Transparent insulating materials

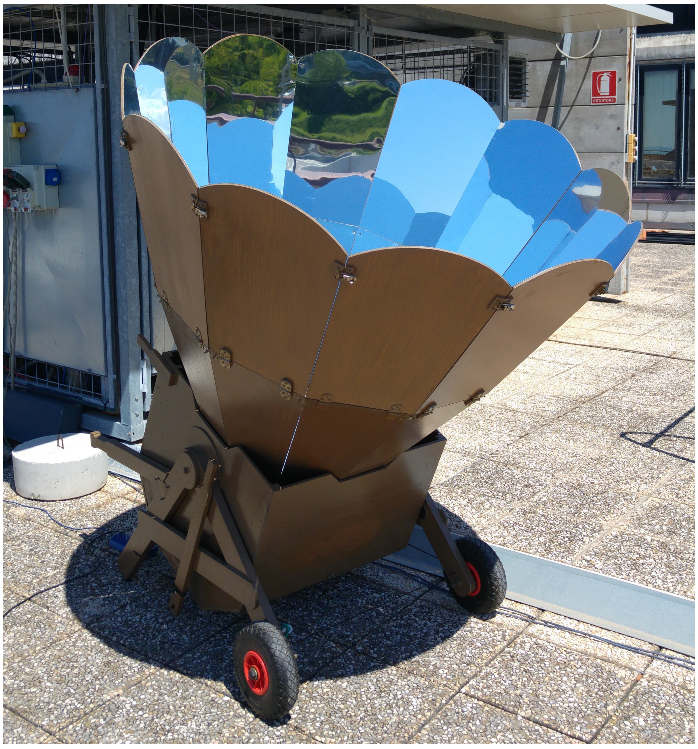

Figure 4.1: A picture of the solar box cooker prototype.

(TIMs) have been studied in order to improve the efficiency of solar box cookers [4].

The absorber tray is another important component of a solar cooker. This element should have a high absorptivity in the solar spectrum to allow an efficient transfer of radiant energy to the food in the cooking pot. Harmim et al. [106] carried out tests on an experimental box-type solar cooker with a finned absorber plate and found that it was about 7% more efficient than a conventional type. Shrestha [107] proved that if the external surface of an absorber plate is painted with selective coating, a better performance can be obtained respect to a simple black coated absorber.

Solar box cookers can be used with any type of cooking vessels, but usually cylindrical or rectangular pots made of aluminum, copper, and stainless steel are adopted. Reddy and Rao [108] compared the performance of a standard solar box cookers and a modified cooker having a cooking vessel with a central annular cavity. The results showed that when the latter is placed on lugs, the hot air circulation through the gap between the bottom of the vessel and the floor of the cooker and through the central annular cavity improves the performance.

Intensive efforts have been performed on solar box cookers in order to allow late evening cooking. Most of research has been focused on solid-liquid phase change materials (PCMs), substances able to store and release a large amount of latent heat. Buddhi and Sahoo [109] designed and tested a PCM made of commercial stearic acid filled below the absorbing plate of a solar box cooker. They reported that the heat transfer rate from the PCM to the cooking vessel during the discharging phase of the PCM was slow and more time was required to cook food in the evening. Domanski et al. [110] investigated two concentric cylindrical vessels made of aluminum and connected together at their tops using four screws to form a double-walled vessel with a gap between the outer (diameter 18 cm) and the inner (diameter 14 cm) walls. The gap was filled with 1.1 kg of stearic acid or 2 kg of magnesium nitrate hexahydrate, leaving sufficient space for expansion of the PCMs during melting. They found that the overall cooker efficiency during the discharging of the PCM was 3–4 times greater than that of steam and heat-pipe solar cookers, which can be used for indoor cooking, but the heat transfer rate from the PCM to the cooking vessel was slow and more time was needed in order to cook evening meal.

Insulation is a crucial element to increase the thermal efficiency of a solar cooker. In a box-type solar cooker, insulation should not be limited to the walls of the box and the absorber as it has been noticed that relevant heat losses can occur through the glazing [111]. Nahar et al. [112] carried out some tests on TIMs used in solar box cookers. Under an indoor solar simulator, they found that the stagnation temperature with a 40 mm thick TIM was 158 °C, while it was 117 °C without TIM. Mishra and Sabberwal Prakash [113] tested four different insulation materials available in rural areas and compared their performance with that of glass wool.

4.2 Design and Optical Analysis

The solar box cooker presented in this work is a prototype realized in DIISM and based on a design developed by Eng. Gianni Crovatto [114]. In his website, Eng. Crovatto shows different types of solar cookers, classified according to their efficiency. Each type is described in detail and several manufacturing plans are available. In order to test the performance of a high-efficiency solar cooker, we decided to realize a prototype following Eng. Crovatto's high-efficiency solar cooker schematics.

The resulting cooker, shown in Figure 4.1, 4.2 and 4.3, is composed by a large box with the function of cooking chamber. This cooker part is also referred to as absorber. The box has a glass cover on the top, which allows solar radiation to be transmitted to the absorber. In the higher part of the box, there is a double row of booster mirrors. These mirrors allow an additional amount of solar radiation to be reflected and, then, concentrated towards the glass and the cooking chamber. Each row includes 12 mirrors and has a different inclination angle respect to the horizontal plane. In the upper row, each mirror is 63 cm long, has a rounded top and can be reclined to reduce the space occupied by the cooker when it is not used and to facilitate its transportation. The lower row mirrors, instead, have a trapezoidal shape and are 61.6 cm long; one of the lower mirrors includes a fissure which allows solar radiation to be projected on an indicator. This indicator is used to evaluate the correct cooker alignment with the sun. The total area of the mirror surface is equal to about $4.2\,\mathrm{m}^2$. Figure 4.4 shows some booster mirror details and how solar radiation is concentrated.

The sum of the glass cover surface area and the booster mirror surface area projected on the glass surface plane is referred to as cooker aperture area. In the case of perfect cooker alignment with the sun, the aperture area is perpendicular to solar radiation. Therefore, it is an important parameter to be considered in the calculation of the cooker ideal exploitable energy. Referring to Figure 4.4, the cooker aperture area, A_a, is equal to:

$$A_\mathrm{a} = A_\mathrm{g} + (A_\mathrm{m1}\cos\theta_1 + A_\mathrm{m2}\cos\theta_2) = 0.17 + 1.79 = 1.96\,\mathrm{m}^2 \tag{4.1}$$

where A_g is the glass cover surface area, A_m1 and A_m2 are, respectively, the lower and upper row surface area, and θ_1 and θ_1 are, respectively, the lower and upper row

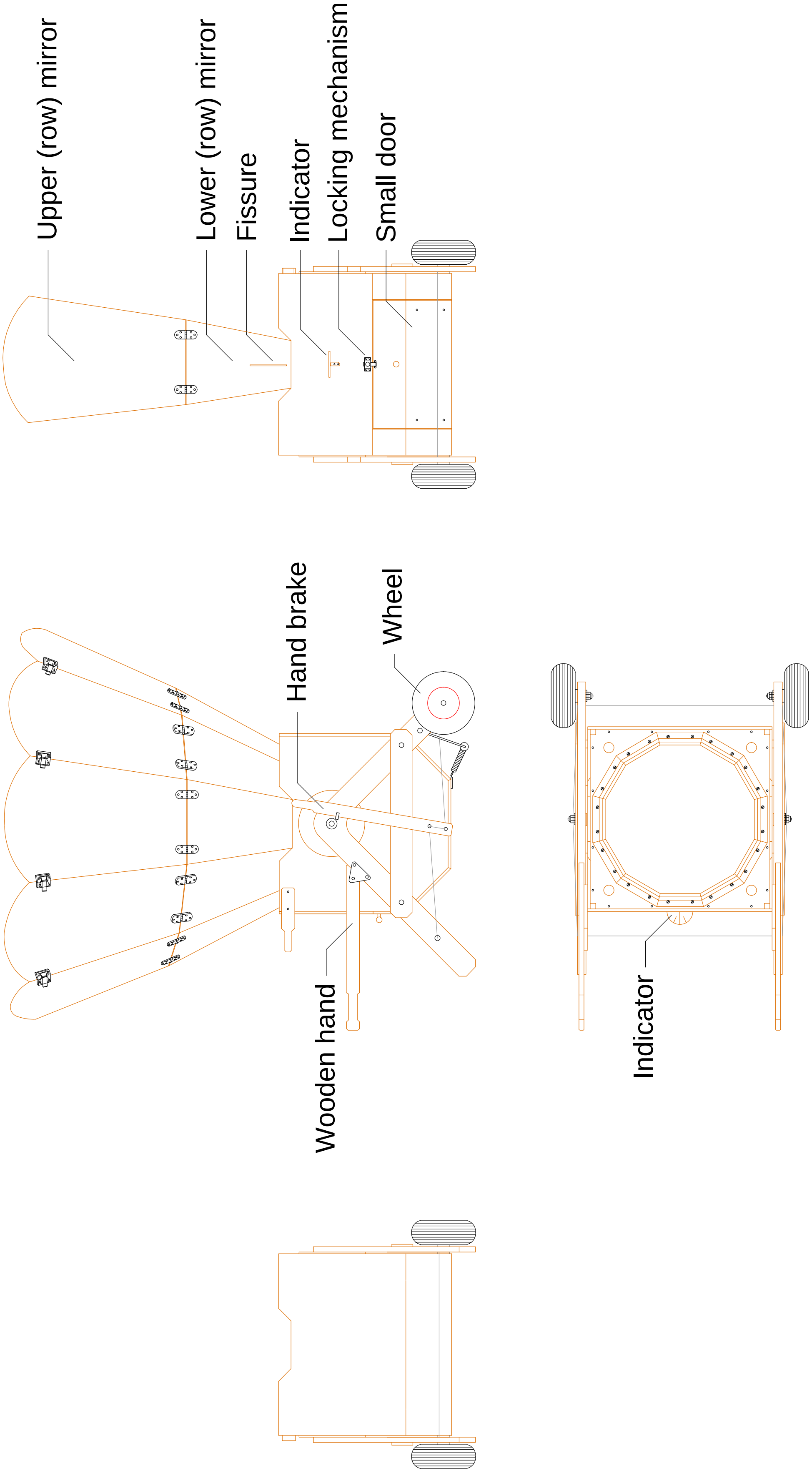

Figure 4.2: Solar box cooker prototype views.

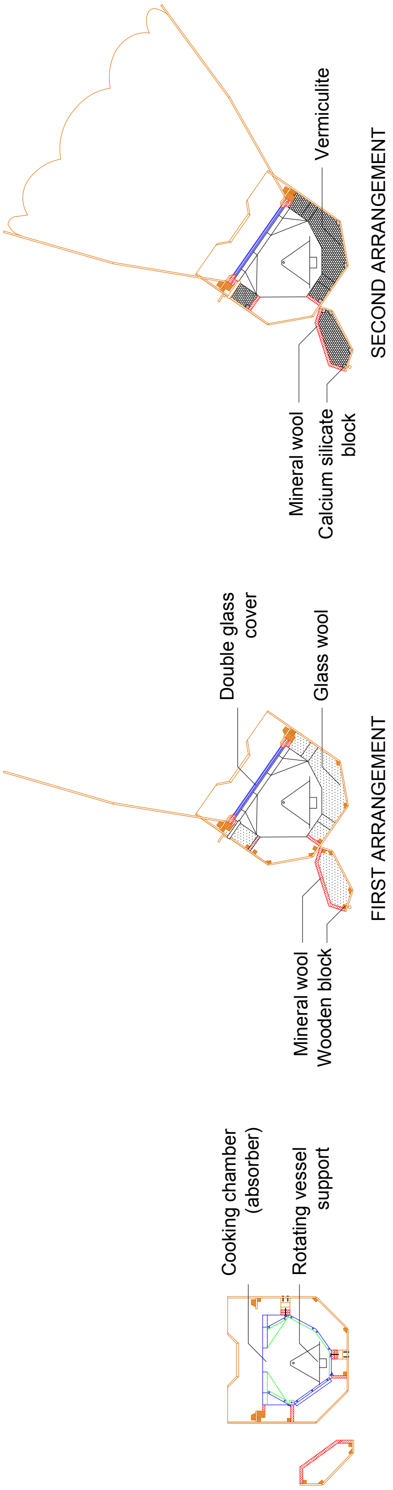

Figure 4.3: Solar box cooker prototype sections. The second arrangement is the actual prototype arrangement.

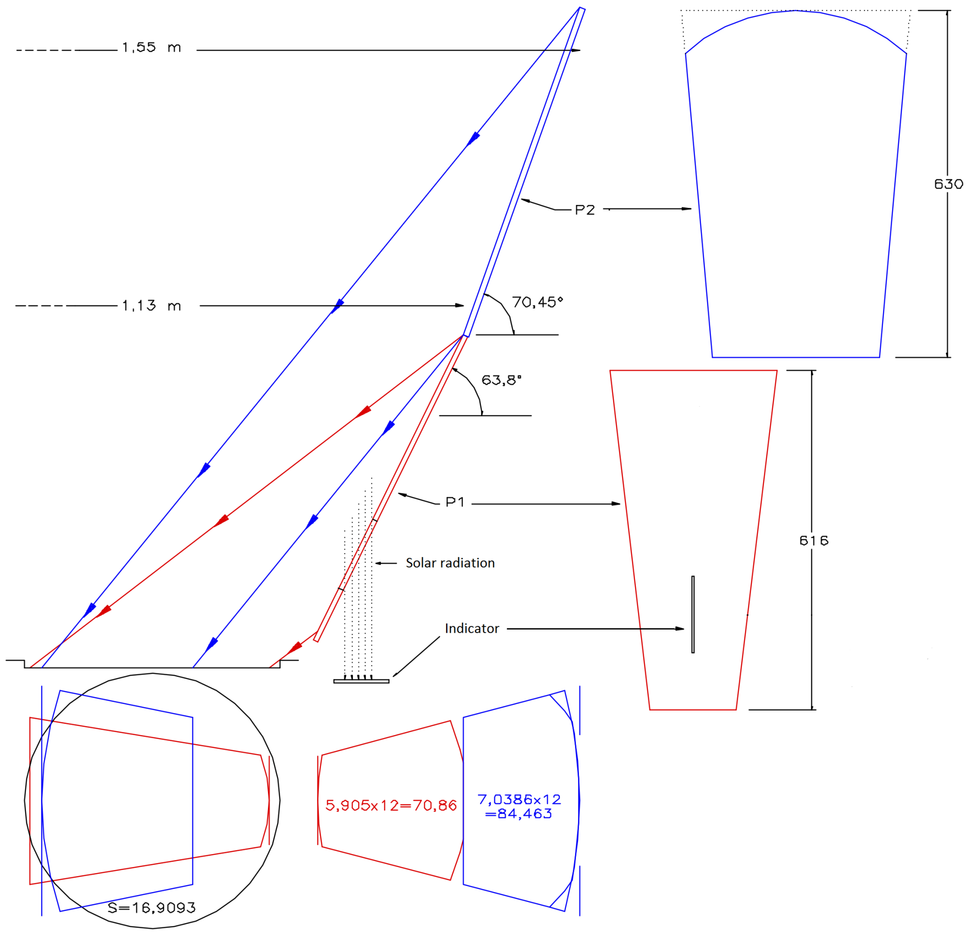

Figure 4.4: Solar box cooker optical scheme [114].

inclination angle. The cooker concentration ratio is:

$$C = \frac{A_{\mathrm{a}}}{A_{\mathrm{g}}} = \frac{1.96}{0.17} = 11.57 \tag{4.2}$$

The concentration ratio value is rather high for a solar box cooker and allows to classify the prototype between box and concentrating cookers. In fact, although the general concept is based on a box cooker type, the particular booster mirror geometry makes the prototype almost completely dependent on direct solar radiation. In other words, the cooker is not able to exploit diffuse solar radiation, thus it requires clear-sky conditions in order to work properly and reach high temperatures. This condition also explains why only a pyrheliometer was used to measure solar radiation, as it will be explained in the following sections.

The cooker has two border wooden hands and two wheels that allow both its movement and its azimuth orientation. A zenith orientation is also possible as the main structure (cooking chamber, glass cover, and booster mirrors) is able to rotate around the horizontal axis. A removable hand brake keeps the cooker fixed when the zenith tracking is not necessary. A small door (35x70 cm) allows food to be inserted in

Table 4.1: Geometrical dimensions of the cooker.

Dimension	Value
Overall volume (m^3)	2.6
Area occupied (closed mirrors) (m^2)	1.03
Area occupied (open mirrors) (m^2)	1.93
Aperture area (m^2)	1.96
Glass surface area (m^2)	0.17
Maximum diameter (m)	1.2
Maximum height (m)	1.8
Mirror overall area (m^2)	4.2
Aperture maximum diameter (m)	1.55
Lower row mirror height (cm)	61.2
Upper row mirror height (cm)	63
Lower row inclination angle (°)	63.8
Upper row inclination angle (°)	70.5
Rotating support surface area (m^2)	0.09
Small door (cm)	35x70

the cooking chamber, which is realized with zinc metal sheets painted with a special black coating. In the chamber, there is a vessel support able to rotate of 360°, so that it can maintain in balance the pots put on it when the zenith orientation changes.

The prototype has a maximum diameter of 1.2 m and a maximum height of 1.8 m. Its mass is about 84 kg and its volume is equal to 2.6 m^3. Table 4.1 summarizes the main geometrical dimensions of the oven.

4.3 Manufacture and Materials

The cooker manufacturing process consisted of 4 consecutive phases:

1. cooking chamber realization and painting;
2. external structure realization;
3. insulating material installation;
4. booster mirror assembly.

4.3.1 Cooking Chamber Realization and Painting

The first manufacturing process involved the cooking chamber, which is the central and innermost part of the cooker. The cooking chamber walls were obtained starting from a stainless steel frame 6/10 mm thick. Following the instructions reported in the Eng. Crovatto design plans [114], the frame was bended and drilled where required. Once all the walls were obtained, they were welded to assume the cooking chamber final shape. The box structure is open on two sides: one side is necessary to introduce food, while the second one to let solar radiation reaching the absorber.

The small door was the second element to be realized. Then, the vessel support was manufactured using a stainless steel frame 10/10 mm thick. The support was

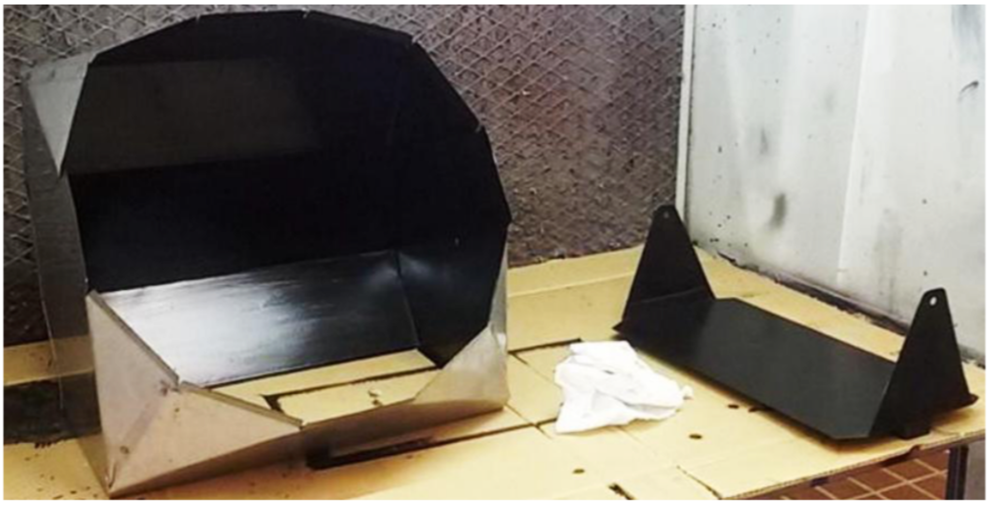

Figure 4.5: Painted cooking chamber and vessel support.

bended with an inclination angle of 90° along the shortest sides and includes two holes and two pivots in order to allow its oscillation when the cooker is moved and rotated. A steel ballast with a mass of 2 kg was attached to the support to improve its balance.

The original design provided by Eng. Crovatto consisted of a cooking chamber painted with common black paint. In order to enhance the absorption coefficient of the cooking chamber surface, in this work a special selective coating usually adopted in solar thermal applications was used. Respect to a common black paint, the selective coating is resistant to high temperature, moisture, and UV degradation. Its absorptance in the solar spectrum is higher and its emissivity is lower. Figure 4.5 shows the cooking chamber and the vessel support once painted.

4.3.2 External Structure Realization

The external structure was realized starting from the side walls, which were obtained by wooden foils 0.7 mm thick. The upper frame has a dodecagonal shape used to support the two booster mirror rows. Several batons were cut and wedged one another to form the dodecagon (Figure 4.6).

An insulated glazing, composed by two tempered glasses 4 mm thick, was inserted in the upper frame. The lower glass was glued to the cooker insulating material with high-temperature-resistant silicone, while the upper one was simply placed on the insulating material and blocked by metal clips. The tempered glass is high resistant (about four times more than a traditional glass with the same thickness) and suitable for solar thermal applications: its declared transmittance in the solar spectrum is about 90%, while its reflection coefficient is 8%.

The cooker truck consists of two border hands and four legs made of phenolic compound. Two of these legs are provided with wheels which allow the cooker to be moved and to realize an azimuth tracking. The truck was connected to the cooker by means of two pivots.

A simple mechanism (Figure 4.7) based on a spring, a stretcher, a lever, and a nylon wire was also adopted to allow a manual block of the cooker rotation around its horizontal axis, necessary to fix its zenith orientation.

Figure 4.6: Dodecagonal upper frame.

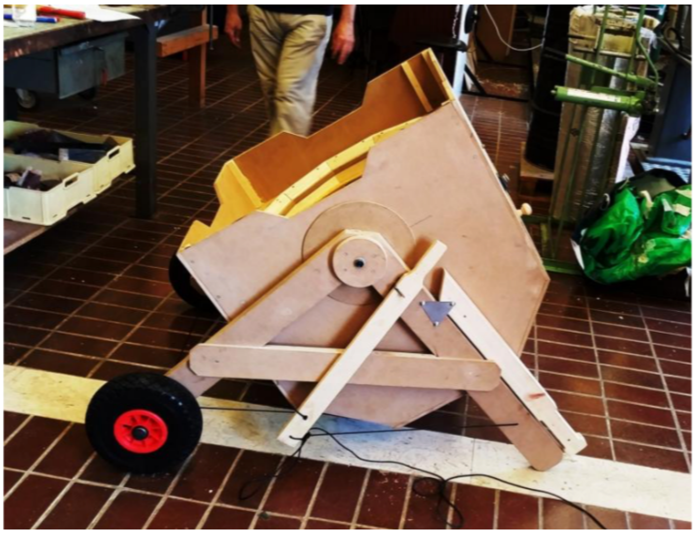

Figure 4.7: External structure.

Finally, the cooking chamber was placed inside the external structure. Its correct alignment respect to the external structure was guaranteed thanks to spacers made of mineral wool and phenolic compound.

4.3.3 Insulating Material Installation

The cooking chamber metal walls were thermally insulated in order to reduce heat losses and obtain higher cooking temperatures. A glass wool layer 10 cm thick was therefore inserted between the metal frame and the external wooden structure. Some cooker parts were also insulated using mineral wool. However, during experimental tests some glass wool pieces emitted smoke, probably due to very high temperatures reached in some points of the cooking chamber.

Thus, several modifications were carried out to avoid smoke. Glass wool was replaced with silicate blocks and vermiculite (Figure 4.3), obtaining good results in terms of thermal insulation. Calcium silicate sheets with hydrate mineral matrix are usually obtained with special productive systems and have a density of about

Figure 4.8: Silicate blocks installed in the small door cavity.

Table 4.2: Silicate properties.

Property	Value
Dimensions (mm)	1200x2500
Thickness (mm)	$8 \div 25$
Long. elastic modulus (MPa)	2500
Tran. elastic modulus (MPa)	2700
Long. bending resistance (MPa)	6
Tran. bending resistance (MPa)	4
Long. tensile resistance (MPa)	2
Tran. tensile resistance (MPa)	1.7
Compressive resistance (MPa)	9
Thermal conductivity (W/(m K))	$0.10 \div 0.20$

875 kg/m^3, so they can be also used for structural purposes. Their main properties are: lightness, fire stability, A1 class incombustibility, and environmental resistance.

The silicate blocks adopted in the solar box cooker also include special additives to further enhance fire protection and lightness. This kind of blocks is generally used in slabs and false ceilings. The picture reported in Figure 4.8 shows two silicate blocks installed in the cooker small door cavity, while Table 4.2 reports the properties of silicates.

Vermiculite is a natural product, very widespread thanks to its mechanical and physical properties: it is used in the building sector as insulating material and in the finishings, in agriculture as draining material and fertilizing/pesticide carrier, and in other industries as fireproof material and lubricant. Standard vermiculite used in the building industry looks like unrefined gravel and is very light, presenting irregular fragments of 1–2 cm diameter. Each fragment has a shining grey-yellow color and consists of a large number of stacked layers, which can be squashed with a reduced force.

From a chemical point of view, vermiculite is a kind of hydromica, i.e. a compound belonging to the phyllosilicate class. In particular, it is the hydrate laminar form of a common phyllosilicate based on iron, magnesium, and aluminum. Phyllosilicates and hydromicas are mineral categories which can result in high complexity, although they share a certain structural type and some chemical features. When quickly heated at a temperature up to 300 °C, vermiculite layers lose water which transforms into steam; the layers peel off and grow (up to 25 times their starting volume) in a direction

Figure 4.9: Vermiculite inserted in the small door cavity.

Table 4.3: Vermiculite properties.

Property	Value
Density (kg/m^3)	90
Thermal conductivity (W/(m K))	0.049
Heat capacity (J/(kg K))	800 ÷ 1100
Weight water retention capacity (%)	220 ÷ 235
Volume water retention capacity (%)	60 ÷ 90

perpendicular to the peeling planes, assuming the typical twisted shape and color of common vermiculite.

Vermiculite is a mineral of great importance in the industrial sector. In fact, if partially heated, it results in a very light product, that can be used stand-alone or mixed with cementive substances as thermal and acoustic insulating material. Vermiculite is also diffused in the plastic, color, paper, and agrarian industry. It can be utilized in the form of powder to cool down weld joints over 700 °C, in order to avoid the formation of cracks and thermal shocks. Finally, it can be adopted as fireproof material.

Figure 4.9 shows the vermiculite inserted in the cooker small door cavity, while Table 4.3 reports its physical properties.

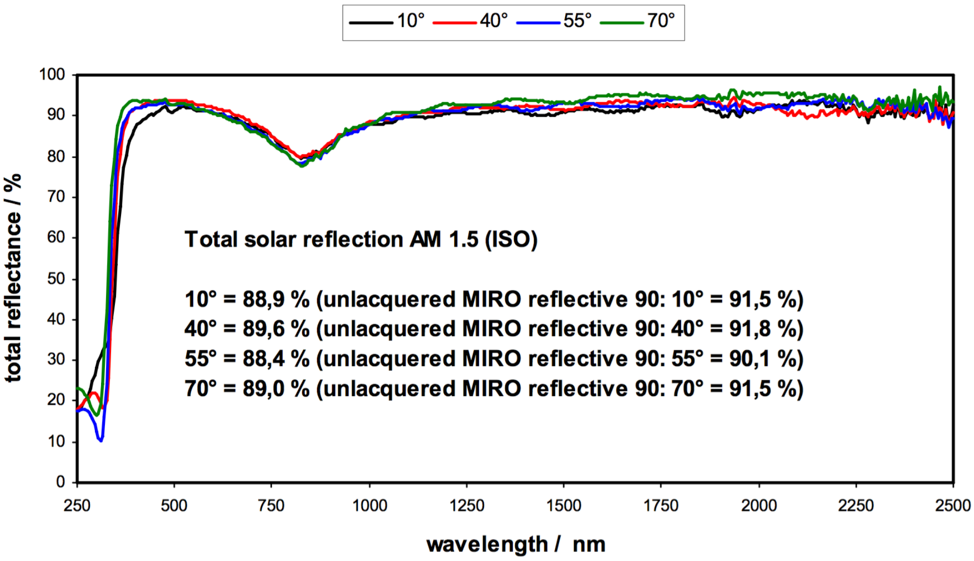

Figure 4.10: Overall spectral reflectance of the booster mirrors in the solar region.

4.3.4 Booster Mirror Assembly

The booster mirrors were realized using aluminum mirrors glued on phenolic compound elements. Special aluminum-based reflective foils (MIRO-SUN Weatherproof Reflective 90 [49]) were adopted to increment the amount of solar radiation collected by the absorber. Respect to standard aluminum foils, these mirrors can better withstand atmospherical agents and guarantee an overall reflection of about 94% in the solar spectrum with a negligible dependence on the incident angle (Figure 4.10).

For the solar reflection efficiency, where wavelengths between 300 nm and 2500 nm have to be considered, the absorption area of aluminum around 800 nm needs a clarification. Unfortunately, this reflectivity dip is unavoidable not only with anodized aluminum, but also with multi-layer coated aluminum.

4.4 Test Bench

The test bench is a measurement system aimed to characterize the solar box cooker, in particular its cooking power and thermal efficiency. The system is schematized in Figure 4.11 and is based on four main elements:

- K-type thermocouples, to measure temperature of ambient and in different points of the solar box cooker;
- a pyrheliometer, to measure direct normal irradiance (*DNI*);
- a data logger, for the signal acquisition;
- a laptop, used to acquire, visualize, and elaborate measurements and results.

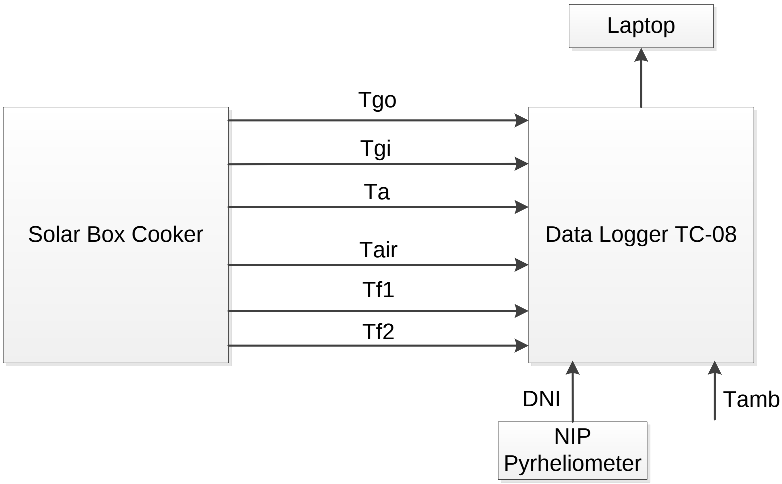

Figure 4.11: Solar box cooker test bench.

4.4.1 K-type Thermocouples and Pyrheliometer

K-type thermocouples were adopted to measure temperature of ambient and in different points of the cooker prototype. These thermocouples are cheap and intended for general purpose. Their measurement interval goes from $-200\,°\mathrm{C}$ to $1260\,°\mathrm{C}$. The sensibility is about $41\,\mu\mathrm{V}/°\mathrm{C}$. They are made of chromel (nickel and chromium alloy) and alumel (nickel, manganese, aluminum, and silicon alloy).

The direct normal irradiance, *DNI*, was measured through a first-class [52] normal-incidence pyrheliometer (NIP) mounted on a solar tracker [53], the same used for the PTC prototype UNIVPM.02 (Chapter 2). The pyrheliometer has a 1 second time response, a temperature dependence of ±1% in the range from -20 to $40\,°\mathrm{C}$, and shows a linear relationship of ±0.5% in the range 0–1400 $\mathrm{W/m^2}$. Global (and diffuse) solar radiation was not measured as the solar box cooker in this work has a high concentration ratio and its optical behavior is more similar to a concentrating cooker than a box one (as explained in Section 4.2).

4.4.2 Laptop and Data Logger

The signals provided by the K-type thermocouples and the pyrheliometer are acquired and elaborated by a Pico Technology TC-08 thermocouple data logger having 8 direct thermocouple inputs. The logger can measure and record temperatures ranging from $-270\,°\mathrm{C}$ to $1820\,°\mathrm{C}$, and is compatible with all popular thermocouples (B, E, J, K, N, R, S, T) offering high accuracy without compromising acquisition speed. The logger is provided with built-in cold junction compensation (CJC) and draws power from the USB port, so no external power supply is necessary. The TC-08 specifications are reported in Table 4.4.

The pyrheliometer was connected to the data logger using an optional terminal board PP624. The board screw terminals allow wires to be attached to the data logger without soldering and enable the TC-08 to measure voltages from 0 to 5 V, or 4–20 mA loop current.

The remaining 7 channels were used to connect 7 K-type thermocouples: one thermocouple was used to measure ambient temperature, while the other thermocouples

Table 4.4: TC-08 data logger specifications.

Specification	Value
Number of channels	8
Conversion time	100 ms per thermocouple channel + 100 ms for CJC
Temperature accuracy	The sum of ±0.2% and ±0.5 °C
Voltage accuracy	The sum of ±0.2% and ±10 µV
Overvoltage protection (V)	±30
Input impedance (MΩ)	2
Voltage input (mV)	±70
Resolution (bit)	20
Reading rate	Up to 10 per second
Operating temperature (°C)	0 to 50
Input connectors	Miniature thermocouple
PC connection	USB
Dimensions (mm)	201x104x34

were located in different points of the cooker. The complete channel list is:

- Channel 1: direct normal irradiance, DNI;
- Channel 2: ambient temperature, T_{amb};
- Channel 3: outer glass temperature, T_{go};
- Channel 4: inner glass temperature, T_{gi};
- Channel 5: absorber temperature, T_{a}, detected on the lower metal wall;
- Channel 6: internal air temperature, T_{air};
- Channel 7: fluid 1 temperature, T_{f1};
- Channel 8: fluid 2 temperature, T_{f2}.

The temperature and solar radiation evolution was visualized in real-time on the laptop through the PicoLog data acquisition program. This software can analyze and display data over long or short time periods. Data can be viewed both during and after data collection in spreadsheet or graphical format, and can be easily exported to other applications.

4.5 Testing Parameters and Procedures

In order to characterize the cooker performance, several parameters were calculated and several procedures were accomplished, using the obtained experimental data. The first and simplest parameter was the time required to reach the fluid evaporation, Δt, also referred to as cooking time. This time is usually calculated starting from a reference fluid temperature. The cooking time was used to derive the specific boiling time, defined as [115]:

$$t_{\mathrm{s}} = \frac{\Delta t A_{\mathrm{a}}}{m} \tag{4.3}$$

where A_a is the cooker aperture area and m is the mass of fluid. The specific boiling time represents the time required to boil 1 kg of fluid using a solar cooker of $1\,\mathrm{m}^2$ aperture area.

Another parameter is the characteristic boiling time [115]:

$$t_\mathrm{c} = t_\mathrm{s} \frac{DNI_\mathrm{av}}{DNI_\mathrm{ref}} \tag{4.4}$$

where DNI_av is the average direct normal irradiance during the time interval Δt, while DNI_ref is a reference direct normal irradiance equal to $900\,\mathrm{W/m^2}$. The characteristic boiling time can be used as a parameter for making comparisons between various solar cooker designs under different solar insolation levels.

The average overall solar cooker thermal efficiency is [115]:

$$\eta_\mathrm{av} = \frac{m\,c\,\Delta T}{DNI_\mathrm{av} A_\mathrm{a} \Delta t} \tag{4.5}$$

where c is the fluid specific heat and ΔT is the temperature difference between the maximum cooking fluid temperature and the ambient temperature.

Mullick et al. [116] introduced the first figure of merit, F_1, which is defined as:

$$F_1 = \frac{T_\mathrm{a,max} - T_\mathrm{amb}}{DNI} \tag{4.6}$$

where $T_\mathrm{a,max}$ is the maximum temperature reached by the absorber, while T_amb and DNI are, respectively, the corresponding ambient temperature and direct normal irradiance measured when the stagnation temperature is reached.

In addition to the first figure of merit, Mullick et al. [116] introduced a second figure of merit, F_2, which involves the temperature increase measurement with time of a known amount of fluid placed in the cooker. It is defined as:

$$F_2 = \frac{F_1 m\,c}{A_\mathrm{a} \Delta t} \ln \left[\frac{1 - \frac{1}{F_1}(T_1 - T_\mathrm{amb,av})/DNI_\mathrm{av}}{1 - \frac{1}{F_1}(T_2 - T_\mathrm{amb,av})/DNI_\mathrm{av}} \right] \tag{4.7}$$

where Δt is the time interval during which the fluid temperature rises from T_1 to T_2, while DNI_av and $T_\mathrm{amb,av}$ are, respectively, the average direct normal irradiance and the average ambient temperature over the time interval Δt.

To calculate the useful fluid heat gain, Funk [117] proposed a testing procedure which allowed to derive the solar cooker cooking power. This procedure requires to divide the obtained acquisition into 10-minute time intervals, and calculate for each interval the average fluid temperature, ambient temperature, and solar radiation. The initial and final fluid temperature of each interval have to be determined, too. In this way, for each interval it is possible to calculate the cooking power as:

$$P = \frac{m\,c\,\Delta T}{\Delta t} \tag{4.8}$$

where, for each 10-minute time interval, ΔT is the fluid temperature difference and Δt is equal to 600 s. Taking into account the cooking power, Funk [117] also presented a term called standard (or adjusted) cooking power which is given as follows:

$$P_\mathrm{s} = P \frac{DNI_\mathrm{ref}}{DNI_\mathrm{av}} \tag{4.9}$$

where DNI_{av} is the average direct normal irradiance for each time interval. DNI_{ref} is a reference illumination intensity level equal to $700\,\text{W/m}^2$.

Lahkar et al. [118] illustrated a procedure similar to the cooking power one to determine the cooker thermal efficiency, η. The difference lies in the fact that this second procedure requires a division in 5-minute time intervals. The thermal efficiency is then calculated, for each time interval, according to Equation (4.5), where Δt is equal to 300 s. If thermal efficiency is plotted against the term $(T_{\text{f}} - T_{\text{amb}})/DNI$, where T_{f}, T_{amb} and DNI are, respectively, the average fluid temperature, ambient temperature, and direct normal irradiance, the coefficients obtained through the thermal efficiency linear fitting are the most relevant parameters to characterize the solar box cooker as they have a direct physical significance. From a comparison with the Hottel–Whillier–Bliss (HWB) equation for solar cookers, which is:

$$\eta = F^{'}\eta_{\text{o}} - \left(\frac{F^{'}U_{\text{L}}}{C}\right)\frac{T_{\text{f}} - T_{\text{amb}}}{DNI} \tag{4.10}$$

it is possible to note that the intercept and slope of the thermal efficiency equation give, respectively, the parameters $F^{'}\eta_{\text{o}}$ and $F^{'}U_{\text{L}}/C$, where $F^{'}$ is the heat exchange efficiency factor, η_{o} is the optical efficiency, and U_{L} is the heat loss factor.

The regression coefficients can be used to determine the cooker opto-thermal ratio, COR, which is defined as the ratio of the optical efficiency–concentration ratio product and the heat loss factor [118]:

$$COR = \frac{\eta_{\text{o}}C}{U_{\text{L}}} \tag{4.11}$$

The cooker opto-thermal ratio appears to be similar to the first figure of merit, F_1 [118]. However, it differs from the other parameters into two aspects:

- it is derived analytically from the HWB equation for concentrating collectors, therefore, unlike other parameters, can be used to denote the performance of any cooker design;
- it indicates the performance of the devices used to augment solar radiation.

The last parameter which can be obtained from experimental results is the maximum achievable fluid temperature, T_{fx}. Under steady-state conditions, η in the HWB Equation (4.10) is equal to zero. Replacing T_{f} by T_{fx} and rearranging the resultant equation, the expression for the maximum achievable temperature is:

$$T_{\text{fx}} = T_{\text{amb}} + \frac{F^{'}\eta_{\text{o}}\,DNI}{F^{'}U_{\text{L}}/C} \tag{4.12}$$

The parameter T_{fx} characterizes the highest achievable temperature of a standard fluid kept in a solar cooker for a given location, and facilitates the selection of the type of cooking (boiling, frying, baking, or roasting) [118].

4.6 Experimental Tests and Results

Experimental tests were carried out in May, June, and July 2016 on the DIISM roof (latitude 43.5867 N, longitude 13.5150 E). The cooker orientation was adjusted about every 5 minutes taking the solar ray indicator as a reference, in order to guarantee a correct alignment with the sun. Two kinds of experimental tests were conduced: with

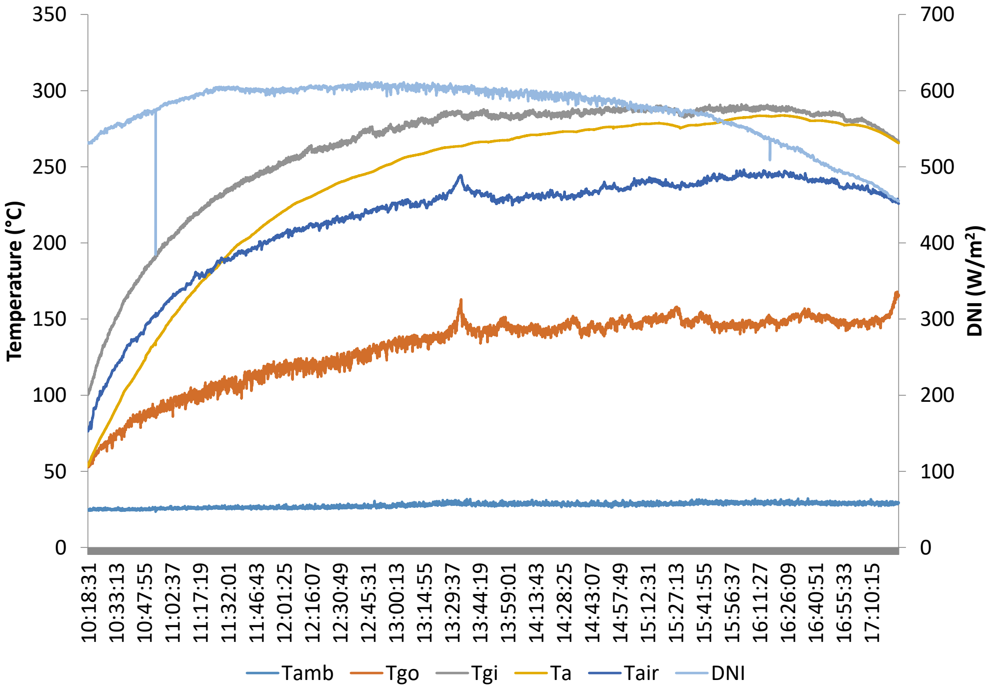

Figure 4.12: Test without load (23/06/2016).

and without load. Tests without load allowed to evaluate the maximum temperature reachable by the solar box cooker.

Tests with load, instead, were accomplished inserting in the cooker a certain amount of fluid contained in cylindrical aluminum vessels having 18 cm diameter and 16 cm height. Each vessel could contain about 4 liters of fluid and was provided with a lid having a small hole, used to let the insertion of a thermocouple. Load tests were necessary to evaluate the cooker cooking power and thermal efficiency. Different load test combinations were carried out:

- with standard and black painted vessels;
- with one and two vessels;
- with water and peanut oil.

Water was the first choice as it is the most common fluid and its physical and chemical properties are well-known. In addition, most of solar cookers available in technical literature are tested using this fluid, thus it is the proper choice to compare experimental results. The main drawback of water is that at atmospheric pressure (which is a condition generally valid for all solar cookers), its boiling temperature is equal to 100 °C. Thus, the useful testing range before the fluid evaporation is rather low. This limits a solar cooker characterization, especially if the cooker is intended to work at high temperatures.

For this reason, we decided to use an additional substance to better characterize the solar box cooker. Peanut oil was finally chosen as it is a fluid with a boiling temperature higher than 200 °C and is, at the same time, a diffused cooking oil. Peanut oil is a vegetable oil that can be obtained by peanut seeds through mechanical pressure

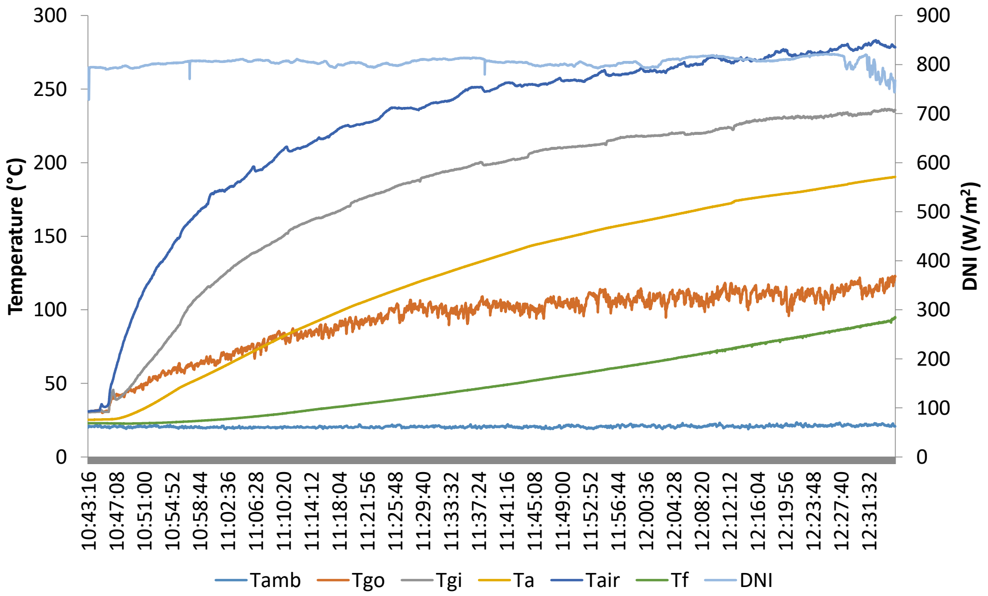

Figure 4.13: Water load test (18/05/2016, standard vessel).

or solvents. The physical-chemical features of vegetable oils can vary depending on the refining process. If highly refined, with free fatty acids $< 0.05\%$, peanut oil smoke point can exceed 220 °C. Its specific heat ranges from 2045 to 2342 J/(kg K) in the interval between 35 and 165 °C [119]. At ambient temperature, peanut oil is liquid and has a vivid yellow color.

4.6.1 Test without Load

A test without load was conduced on June 23, 2016. The test started at 10:18 and ended at 17:25. The average direct solar irradiance and ambient temperature were, respectively, 572 $\mathrm{W/m^2}$ and 27 °C.

Figure 4.12 shows the temperatures and the solar radiation detected during the test. According to the measurements, the maximum absorber temperature was reached at 16:23 and was 283.73 °C. The corresponding ambient temperature was 29.10 °C, while the *DNI* was equal to 529.38 $\mathrm{W/m^2}$. These values allowed to determine the first figure of merit, F_1, which resulted equal to 0.48 $\mathrm{°C/(W/m^2)}$.

4.6.2 Water Load Tests

The first load test was carried out on May 18, 2016, from 10:43 to 12:44. The average direct normal irradiance was 802.70 $\mathrm{W/m^2}$ and the average ambient temperature was 20.78 °C. A standard aluminum vessel was filled with 3.82 kg of water, which took about 2 hours to reach evaporation. Figure 4.13 shows the temperatures and the solar radiation detected during the test.

Other load tests were executed on different days. Since the qualitative trend shown in Figure 4.13 resulted the same, it was decided not to report the remaining graphs. Instead, the overall water temperature trend detected during the load tests is shown in Figure 4.14, while a summary of all the measurements is reported in Table 4.5.

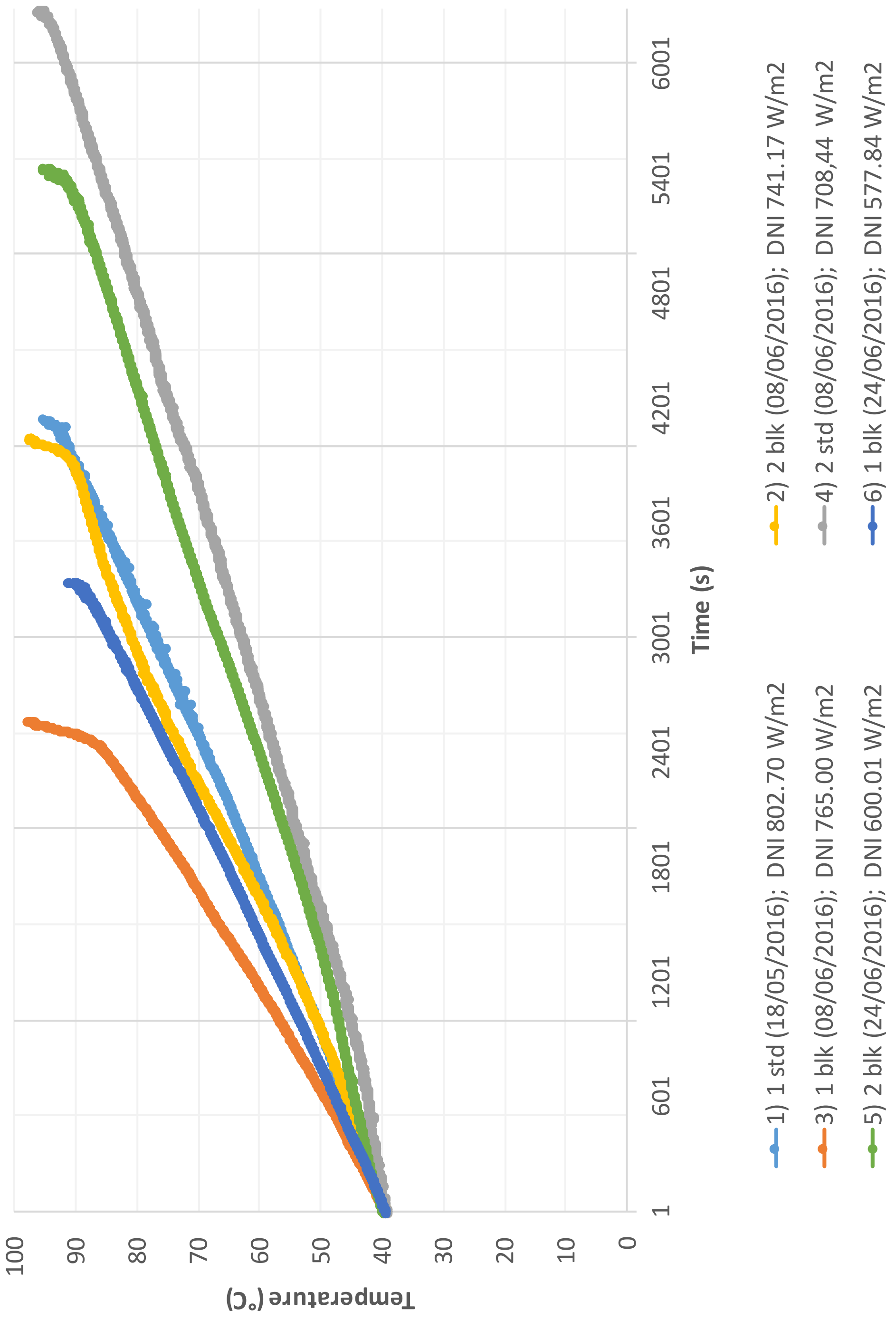

Figure 4.14: Water temperature trend.

Table 4.5: Water load test summary. Testing parameters are referred to a time interval during which water temperature rose from 40 to 90 °C.

Quantity	Test 1	Test 2	Test 3	Test 4	Test 5	Test 6
Date	18/05/2016	08/06/2016	08/06/2016	08/06/2016	24/06/2016	24/06/2016
Start	10:43	09:36	11:46	13:06	13:02	14:54
End	12:44	11:33	12:56	15:18	14:39	16:13
Vessel type	Standard	Black	Black	Standard	Black	Black
Vessel number	1	2	1	2	2	1
$T_{\mathrm{amb,av}}$ (°C)	20.78	24.71	27.00	28.96	30.63	31.54
DNI_{av} ($\mathrm{W/m^2}$)	802.70	725.20	764.91	725.70	599.70	579.06
m_1 (kg)	3.82	3.64	3.77	3.76	3.87	3.84
m_2 (kg)	-	3.67	-	3.76	3.86	-
Δt (s)	3849	3805	2441	5695	5268	3205
t_{s} ($\mathrm{min\,m^2/kg}$)	32.89	17.00	21.12	24.71	22.24	27.26
t_{c} ($\mathrm{min\,m^2/kg}$)	29.25	14.11	18.04	20.66	14.87	17.34
η_{av}	0.13	0.27	0.22	0.19	0.26	0.23
F_2	0.15	0.31	0.24	0.21	0.30	0.26

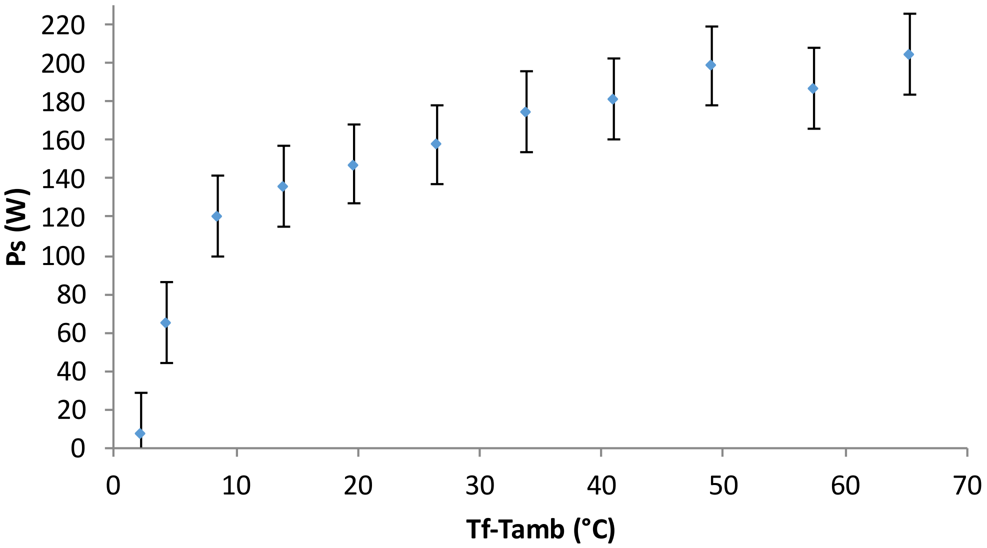

Figure 4.15: Standard cooking power as a function of temperature difference. The fluid is water.

From Figure 4.14 and Table 4.5, several considerations can be outlined.

- When environmental conditions are comparable, the time required to boil water is considerably less when a black-painted vessel is adopted. A black-painted vessel is able to perform better than a standard vessel also when average solar radiation is lower. This trend is clear from test 1, 3, and 6 in Figure 4.14.
- Under comparable environmental conditions, two vessels (standard or black-painted) always require more time to boil water than one similar vessel. However, with two black-painted vessels, water evaporation can be as fast as one standard vessel (compare test 1 and 2 in Figure 4.14).
- Under comparable environmental conditions, two vessels (standard or black-painted) generally exhibit better average thermal efficiency and F_2 respect to only one vessel. This trend was confirmed in other works [120–122]. In solar box cookers, it was proved that the more the number of pots, the better the optical efficiency.
- Average solar radiation is a critical parameter for the cooker performance, while ambient temperature has a less important role.

Looking at Figure 4.13 or Figure 4.14, it is possible to note that the fluid temperature is described by a convex function. Plotting a P_s vs. $(T_\mathrm{f} - T_\mathrm{amb})$ graph, where P_s is the standard cooking power defined by Funk [117] while T_f and T_amb are, respectively, the average fluid and ambient temperature in each time interval, the result is as reported in Figure 4.15.

The trend visible in Figure 4.15 is somewhat unexpected, as a correct trend would have been linearly decreasing with the temperature difference: the cooking power should be lower when the fluid temperature is higher, as thermal losses with the environment are greater. Other water load tests, executed with a higher starting inner cooker temperature and larger water masses, gave comparable results. In literature, other

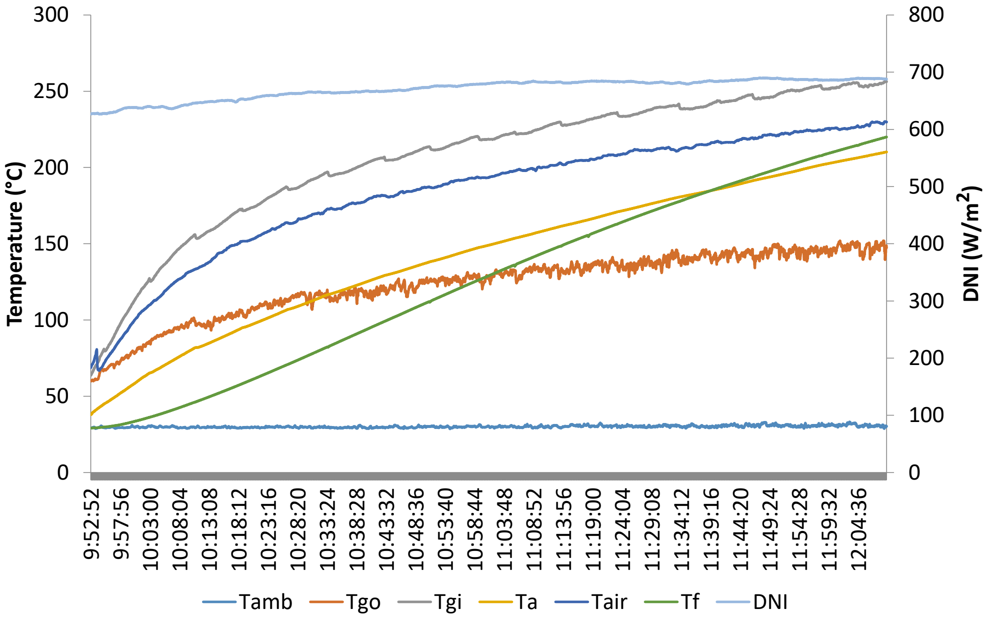

Figure 4.16: Peanut oil load test (01/07/2016, black-painted vessel).

works reported a similar trend [123], although they do not provide any explanation of this behavior.

A phenomenon physical interpretation could be that, at the tested temperatures, the cooker thermal losses are too low to influence the useful fluid gain. In other words, the cooker is not able to reach a steady (or quasi-steady) state condition during tests, as its thermal load is too low to represent a significant contribution. The standard cooking power trend in Figure 4.15 could be predicted, as it is a direct consequence of the fluid temperature trend in Figure 4.13. In fact, the fluid convex trend implies that, in successive equal time intervals, the delta temperature increases continuously, and so behaves the cooking power.

Since water load tests did not allow to correctly characterize the solar box cooker, peanut oil load tests were carried out to verify how the cooker works at high temperatures.

4.6.3 Peanut Oil Load Tests

The first peanut oil load test was carried out on July 1, 2016, from 09:52 to 12:09. A black-painted vessel was filled with 3 kg of oil. The average ambient temperature and direct solar irradiance were, respectively, 30.80 °C and 677.13 W/m^2. The test was interrupted when the oil reached a temperature of about 220 °C, which is equal to its smoke point, in order to avoid degradation. Figure 4.16 shows the temperatures and the solar radiation detected during the test.

Comparing Figure 4.16 to Figure 4.13, it is possible to see that the oil temperature trend is different respect to water. In fact, the oil temperature curve is initially convex then, starting from about 90 °C, concave. As discussed for water tests, the concave fluid behavior is what we expected for a correct cooker characterization. Thus, the standard cooking power procedure [117] was repeated for the peanut oil and a linear

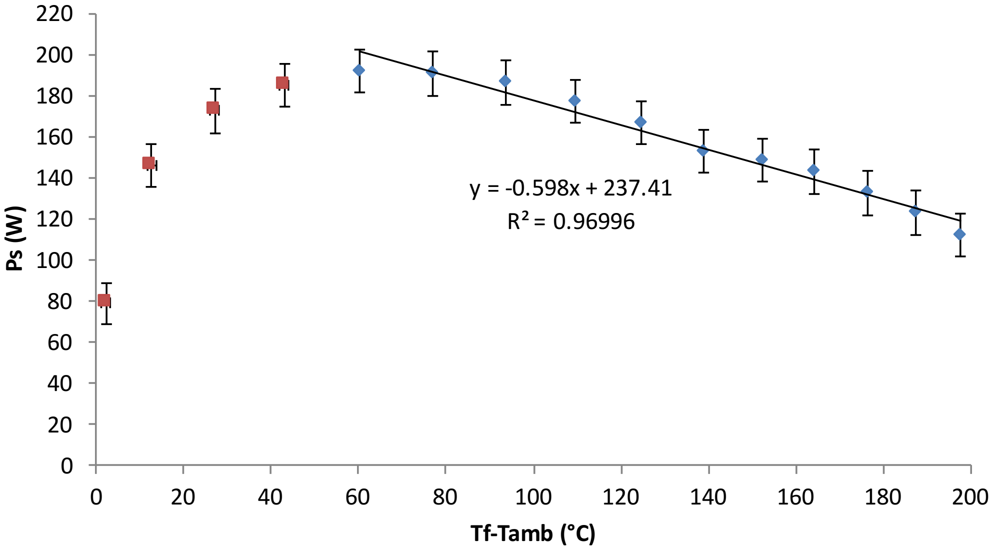

Figure 4.17: Standard cooking power using peanut oil.

regression was fitted for the points having a decreasing linear trend. The peanut oil specific heat values were taken from the experimental measures made by Fasina and Colley [119].

The results of the procedure are visible in Figure 4.17, which shows the curve fitting equation and the coefficient of determination R^2. The slope of the cooking power regression line correlates to the heat loss coefficient and is independent of the intercept area. It is possible to prove that where the heat loss coefficient influence is zero (i.e. at the intercept, where the temperature difference is zero), cookers with the same intercept area have roughly the same standard cooking power [117].

If the thermal efficiency defined by Lahkar et al. [118] is plotted against the term $(T_\mathrm{f} - T_\mathrm{amb})/DNI$, where T_f, T_amb and DNI are, respectively, the average fluid temperature, ambient temperature, and direct normal irradiance, the result is as reported in Figure 4.18. In addition to the experimental points, this figure also shows the thermal efficiency curve fitting equation and the coefficient of determination R^2.

As explained in Section 4.5, the slope and the intercept coefficients obtained through the thermal efficiency curve fitting correspond to the parameters $F^{'}\eta_\mathrm{o}$ and $F^{'}U_\mathrm{L}/C$, where $F^{'}$ is the heat exchange efficiency factor, η_o is the optical efficiency, and U_L is the heat loss factor.

The coefficients can also be used to determine the cooker opto-thermal ratio and the maximum achievable fluid temperature, T_fx. A summary of the load tests carried out with peanut oil is reported in Table 4.6.

From the analysis of Table 4.6, the following considerations can be made.

- As outlined for water, two vessels exhibit better parameters respect to only one vessel when the solar radiation availability is comparable. This is due to the fact that the cooking chamber is better employed, resulting in a higher $F^{'}$.
- Respect to water, η_av is lower, as the delta temperature under consideration is much higher and, hence, thermal losses. F_2, instead, seems to be less dependent on the temperature range, especially when two vessels are considered.

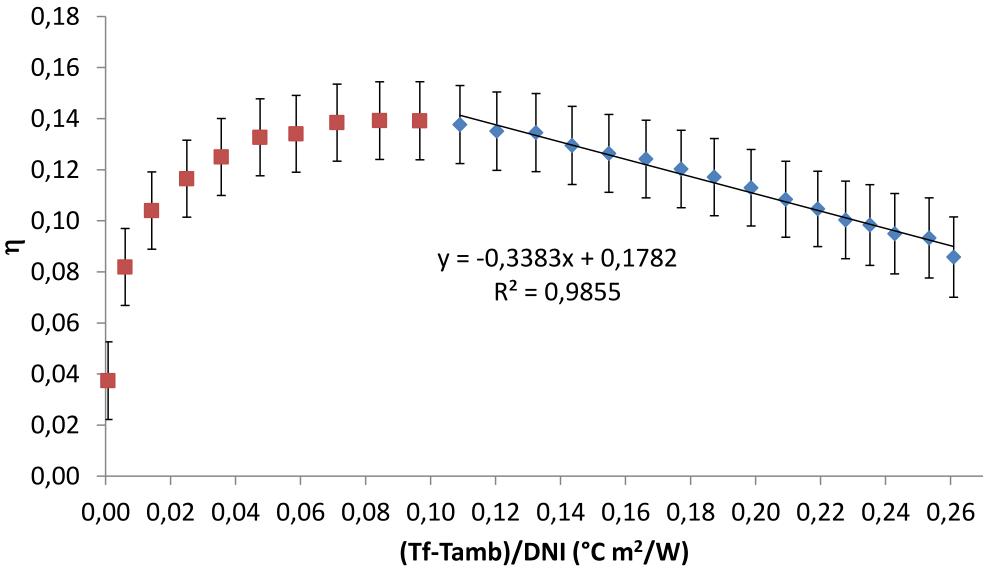

Figure 4.18: Thermal efficiency. The fluid is peanut oil.

- Comparing the standard cooking power coefficients obtained during the tests, it is possible to note that the case with two vessels shows a higher intercept. Since the aperture area is constant in both the cases, the difference is entirely due to a better use of the cooking chamber: two vessels are able to collect much more solar radiation than one. Instead, the cooking power slope is higher for two vessels as heat losses are more prominent. These considerations are also valid for the thermal efficiency coefficients.
- The parameters COR and T_{fx} appear to be very similar in both the cases, resulting almost independent of cooking load.

4.6.4 Comparison with Literature

A comparison with solar cooker prototypes available in literature is not a simple task as the absence of a reference standard makes each test different from the others. An attempt of comparison is provided in Table 4.7, where data reported in experimental works concerning solar box cookers were gathered. As can be noted, all the considered works used water as testing fluid and non-painted vessels.

We can try to analyze the data reported in Table 4.7 to determine how the prototype presented in this work behaves respect to the other works. Some considerations are reported in the following list.

- The number of vessels is an important variable for a cooker cooking power and thermal efficiency. As can be observed from the results obtained in this work and from El-Sebaii and Ibrahim [122], when the number of pots increases the cooking times reduce, while η_{av} and F_2 improve. The standard cooking power intercept tends to enhance as $F^{'}$ assumes a higher value: the cooking chamber is utilized in a better way. Instead, the standard cooking power slope worsens because thermal losses are proportional to the the vessel number. The same conclusions can be extended to thermal efficiency.

Table 4.6: Peanut oil load test summary. Testing parameters are referred to a time interval during which the oil temperature rose from 40 to 220 °C.

Quantity	Test 1	Test 2
Date	01/07/2016	12/07/2016
Start	09:52	10:05
End	12:09	13:17
Vessel type	Black	Black
Vessel number	1	2
$T_{\mathrm{amb,av}}$ (°C)	30.80	33.02
DNI_{av} (W/m^2)	677.13	659.68
m_1 (kg)	3.00	3.00
m_2 (kg)	-	3.00
Δt (s)	7402	9926
t_{s} (min m^2/kg)	80.47	53.95
t_{c} (min m^2/kg)	59.23	39.55
η_{av}	0.12	0.19
F_2	0.19	0.29
P_{s} intercept (W)	237.41	378.04
P_{s} slope (W/°C)	0.598	1.016
$F^{'}\eta_{\mathrm{o}}$	0.178	0.288
$F^{'}U_{\mathrm{L}}/C$ (W/(m^2 °C))	0.338	0.556
COR (°C/(W/m^2))	0.527	0.518
T_{fx}	387.65	374.73

- The testing fluid assumes, of course, a certain importance in the evaluation of a solar cooker performance. For example, a comparison between water and peanut oil cannot be direct as the former has a specific heat higher than that of peanut oil (i.e., water temperature rises slower than peanut oil one).

- The standard cooking power intercept is correlated to a solar cooker aperture area. In the case of cookers having a similar design, this parameter can be used to assess which cooker has a greater intercept surface. The thermal efficiency intercept, instead, is not correlated to the aperture area and is generally used to assess which design has a better optical performance: e.g., in the work by Lahkar et al. [118], the parabolic cooker has a better optical performance respect to the box one.

- The standard cooking power slope is related to the cooker thermal losses and it depends on the cooker insulation and aperture area. In addition, it strongly depends on the vessel number and type. On the other hand, the thermal efficiency slope is independent of the concentration ratio and is particularly sensitive to the cooker type. For example, in the work by Lahkar et al. [118], the parabolic design shows higher thermal losses due to the absence of a cooking chamber.

- The cooker opto-thermal ratio is a good parameter which summarizes the cooker performance, considering both its optical efficiency and insulation level, and can be used to compare different cooker designs.

Table 4.7: Comparison with literature. Some parameters were elaborated averaging the data provided in the different works.

Quantity	This work	This work	[117]	[122]	[122]	[118]	[118]
Date	01/07/2016	12/07/2016	1997–1998	07/2002	07/2002	NA	NA
Cooker type	Box	Box	Box	Box (Model I)	Box (Model II)	Box	Parabolic
Vessel type	Black	Black	Standard	Standard	Standard	Standard	Standard
Vessel number	1	2	5	1	4	4	1
Fluid	Peanut oil	Peanut oil	Water	Water	Water	Water	Water
$T_{\mathrm{amb,av}}$ (°C)	30.80	33.02	NA	31.1	NA	30	30
DNI_{av} (W/m^2)	677.13	659.68	-	-	-	-	-
$G_{\mathrm{t,av}}$ (W/m^2)	-	-	NA	902.5	NA	906	906
A_{a} (m^2)	1.96	1.96	NA	0.594	0.594	0.492	1.545
C	11.57	11.57	1	NA	NA	2.09	8.88
m (kg) (per vessel)	3.00	3.00	0.424	1	1	0.37	4.751
t_{s} (min m^2/kg)	80.47	53.95	NA	NA	16.5	NA	NA
t_{c} (min m^2/kg)	59.23	39.55	NA	76.7	14.9	NA	NA
η_{av}	0.12	0.19	NA	NA	0.267	NA	NA
F_1	0.48	0.48	NA	0.14	0.14	NA	NA
F_2	0.19	0.29	NA	0.197	0.407	NA	NA
P_{s} intercept (W)	237.41	378.04	120	58.70	99.87	NA	NA
P_{s} slope (W/°C)	0.598	1.016	1.57	0.758	1.575	NA	NA
$F^{'}\eta_{\mathrm{o}}$	0.178	0.288	NA	NA	NA	0.213	0.348
$F^{'}U_{\mathrm{L}}/C$ (W/(m^2 °C))	0.338	0.556	NA	NA	NA	1.576	2.260
COR (°C/(W/m^2))	0.527	0.518	NA	NA	NA	0.136	0.155
T_{fx}	387.65	374.73	NA	NA	NA	147.75	161.82

Chapter 5

Conclusions

The main objective of the work presented in this thesis was to investigate the thermal performance of two concentrating solar prototypes: a parabolic trough collector (PTC) and a solar box cooker. Being two examples of solar thermal systems, these two devices share a great number of problems and possibilities, which will be discussed in this final chapter.

Firstly, let us consider the PTC prototype, UNIVPM.02. Although a concentration ratio of 19.89 is not one of the highest available in literature, experimental tests showed that thermal efficiency is comparable with that of other similar collectors. The slope of the linear thermal-efficiency equation, which can be associated with thermal losses, is rather low when released from the concentration ratio term: this means that the receiver has been well designed and built. On the other hand, the intercept thermal efficiency coefficient, which is representative of the optical performance, is good but no as the previous prototype, UNIVPM.01.

This difference could be due to the different manufacturing process of the two prototypes. UNIVPM.01 was realized by a hand lay-up method, which guaranteed a final low weight and good resistance properties. On the contrary, UNIVPM.02 was manufactured through a VARTM (Vacuum Assisted Resin Transfer Molding) technique which ensured great mechanical properties, but also presented an unexpected drawback: a weight larger than the one estimated. This inconvenient was due to an error occurred during the manufacturing process, which leaded the fiberglass to shrink and the concentrator profile to distort. In order to correct this distortion, three fiberglass ribs were added to the parabola external surface, but this leaded the overall weight to rise. Unfortunately, assisted manufacturing processes for the construction of PTC concentrators are not widespread and the corresponding know-how needs to be improved in order to make these processes reliable and cost-effective for industrial heat applications. At the moment, hand lay-up methods seem to be more advisable for small-scale productions.

A way to improve a PTC thermal efficiency lies in the adoption of novel heat transfer fluids, such as nanofluids. Despite most of literature results, the six water-based nanofluids studied in this work, in the range of temperature and concentration investigated, seem not to induce an improvement in the efficiency respect to water. The improvements in thermal efficiency relate to low concentrations of nanoparticles. This is due to the fact that dynamic viscosity tends to considerably increase with weight concentration. However, since dynamic viscosity decreases with temperature, while thermal conductivity increases, it could be of some interest evaluating the nanofluid potential at higher temperatures. This could be achieved by conducing further experimental investigations at high temperature on reduced concentrations of nanoparticles such as TiO_2, ZnO, Al_2O_3, and Au, which did not give negative results in the investigated temperature range. Metal oxides at reduced concentration are cost-effective, therefore this kind of nanoparticles could be suitable for the aforementioned experimental investigations. In addition, there are still different nanoparticles, e.g. carbon nanotubes and nanohorns, and other metals such as copper, that could be worthy of investigations.

Another promising field of investigation concerning nanofluids includes the utilization of direct absorption solar collectors (DASCs) [124]. In common solar thermal collectors, the absorber transfers heat to a fluid flowing in tubes embedded within or fused onto the surface. In this case, the efficiency is limited by not only by how effective the absorber captures solar energy, but also how effectively the heat is transferred to the heat transfer fluid. In order to enhance the efficiency of collectors while simplifying the system, DASCs were proposed as they are able to directly absorb the solar energy within the fluid volume. Nanoparticles offer the potential of improving the radiative properties of liquids leading to an increase in DASC efficiency. However, in this field experimental works are still scarce, while numerical simulations employ complicated equations which require additional validation.

The experimental characterization carried out on the solar box cooker proved that the prototype is able to cook any kind of food, since cooking is fast and at high temperature. An unavoidable drawback of high temperature cooking is that requires a high degree of solar concentration. Hence, only direct solar radiation can be used for the purpose. This condition limits the usability range of the cooker, which is limited to clear-sky days. In addition, evening cooking is difficult to be accomplished, particularly on the winter season during which solar radiation availability is limited to a few hours in the afternoon.

These restrictions could be removed by taking into account a cooker thermal storage system. In technical literature, several solutions were proposed for the purpose [6]. One of the most promising seems to consist of a unit composed by two metal concentric cylindrical vessels. These are connected together to form a double-walled vessel with its gap filled with a certain amount of phase change material (PCM) [27]. The adoption of a PCM thermal storage system could allow both the opportunity of evening cooking and the possibility to better stabilize the cooker temperature when sky conditions are variable. Several molten salt and nanofluid based PCMs were studied in literature [125–128], which seem to guarantee optimal performance at high temperature. A thermal storage unit of the aforementioned kind is currently under study in DIISM (Department on Industrial Engineering and Mathematical Sciences).

Appendix A

Mathematical Model of a PTC

This appendix presents a detailed PTC mathematical model. It is divided into three sections: tracking of the sun, optical analysis, and thermal analysis. The first section is an overview of equations and relationships used in solar geometry to determine the position of the sun and, hence, the slope and the angle of incidence that in each instant must be assumed by a PTC to correctly follow the sun. Since PTCs usually have one degree of freedom, correlations valid for east-west and north-south axis with continuous adjustment are discussed. The optical analysis starts by introducing the concentration ratio and continues presenting a thorough description of the geometry of a PTC. Optical errors and geometrical effects are also presented. Then, the optical analysis is concluded by taking into account the optical properties of the materials generally adopted in PTCs: the mirror, the cover, and the absorber. The last section involves a PTC thermal analysis, i.e. the receiver energy balance. Each heat flux is described in detail, in order to determine the thermal efficiency of a PTC.

A.1 Tracking of the Sun

This section shows the essential equations to calculate the position of the sun. Specific equations to be used with PTCs will be also given.

A.1.1 Solar Time

With the term *solar time*, we intend the time based on the apparent angular motion of the sun across the sky. The time the sun crosses the meridian of the observer is called *solar noon*. Solar time does not coincide with local clock time. It is necessary to convert standard time to solar time by applying two corrections [28]:

1. the first correction is for the difference in longitude between the observer's meridian and the meridian on which the local standard time is based;
2. the second correction derives from the equation of time, which accounts for the perturbations in the earth rate of rotation that affects the time the sun crosses the observer's meridian.

The difference expressed in minutes between solar time and standard time is [28]:

$$\text{Solar Time} - \text{Standard Time} = 4\left(L_{\text{st}} - L_{\text{loc}}\right) + E \tag{A.1}$$

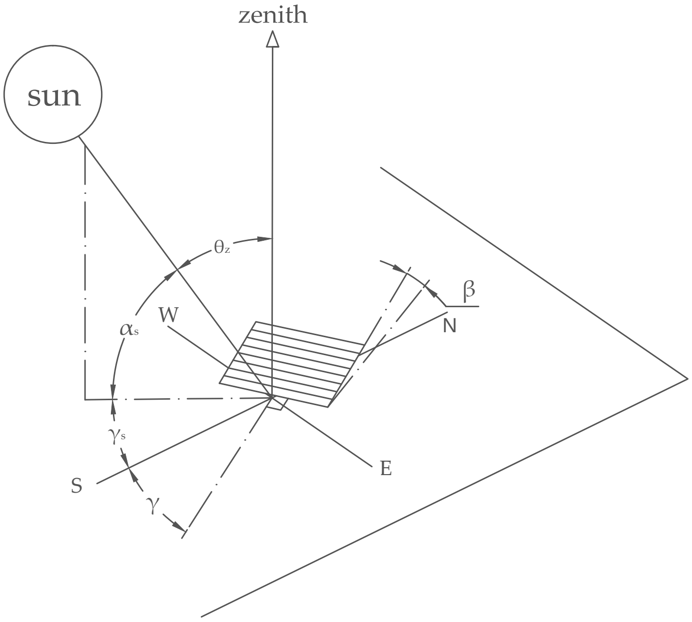

Figure A.1: Solar angles for a tilted surface. Adapted from Duffie and Beckman [28].

where L_{st} is the standard meridian for the local time zone and L_{loc} is the longitude of the site (longitudes are in degrees west). The symbol E denotes the equation of time, expressed in minutes [28]:

$$\begin{aligned} E = 229.2\,(&0.000075 + 0.001868\cos B - 0.032077\sin B \\ &- 0.014615\cos 2B - 0.04089\sin 2B) \end{aligned} \tag{A.2}$$

where

$$B = (n-1)\,\frac{360}{365} \tag{A.3}$$

In Equation (A.3), n is the nth day of the year. Note that Equation (A.2) and all the equations in the following use degrees and not radians. Time is assumed to be solar time unless indication is given otherwise.

A.1.2 Solar Angles

The sun position respect to a plane of any particular orientation to the earth at any time can be described in terms of several angles, reported in Figure A.1. The angles and their sign conventions are as follows [28].

- Latitude (ϕ): it is the angular location of a terrestrial site with reference to the Equator. It is north positive: $-90° < \phi < 90°$.
- Declination (δ): it is the angular position of the sun at solar noon respect to the plane of the Equator. It is north positive: $-23.45° < \delta < 23.45°$. The declination can be found with the following equation [28]:

$$\begin{aligned} \delta = (180/\pi)(&0.006918 - 0.399912\cos B + 0.070257\sin B \\ &- 0.006758\cos 2B + 0.000907\sin 2B - 0.002697\cos 3B \\ &+ 0.00148\sin 3B) \end{aligned} \tag{A.4}$$

where B was defined in Equation (A.3).

- Slope (β): it is the angle between the plane of a surface and the horizontal. If it is greater than 90°, the surface has a downward-facing component: $0° < \beta < 180°$.
- Surface azimuth angle (γ): it is the deviation of the projection on a horizontal plane of the normal to the surface from the local meridian. It is zero due south, east negative and west positive: $-180° < \gamma < 180°$.
- Hour angle (ω): it is the angular displacement of the sun east or west of the local meridian due to rotation of the earth on its axis at 15° per hour. It is negative in the morning and positive in the afternoon.
- Angle of incidence (θ): it is the angle between the beam radiation on a surface and the normal to that surface. The angle of incidence is related to the above mentioned angles through the expression:

$$\begin{aligned}\cos\theta &= \sin\delta\sin\phi\cos\beta - \sin\delta\cos\phi\sin\beta\cos\gamma \\ &+ \cos\delta\cos\phi\cos\beta\cos\omega + \cos\delta\sin\beta\sin\gamma\sin\omega \\ &+ \cos\delta\sin\phi\sin\beta\cos\gamma\cos\omega\end{aligned} \tag{A.5}$$

  The angle of incidence may exceed 90°, meaning that the sun is behind the surface. Equation (A.5) implies that the hour angle is between sunrise and sunset.
- Zenith angle (θ_z): it is the angle between the vertical and the line of the sun. If the surface is horizontal ($\beta = 0$), θ_z corresponds to the angle of incidence and Equation (A.5) becomes:

$$\cos\theta_z = \sin\delta\sin\phi + \cos\delta\cos\phi\cos\omega \tag{A.6}$$

- Solar altitude angle (α_s): it is the angle between the horizontal plane and the beam radiation. It is the complementary angle of the zenith.
- Solar azimuth angle (γ_s): it is the angular displacement from south of the projection of the line of the sun on the horizontal plane. Displacements east of south are negative and west of the south are positive. The solar azimuth angle can be found with:

$$\gamma_s = \mathrm{sgn}(\omega)\left|\cos^{-1}\left(\frac{\cos\theta_z\sin\phi - \sin\delta}{\sin\theta_z\cos\phi}\right)\right| \tag{A.7}$$

  where the sign function is equal to $+1$ if ω is positive and to -1 if ω is negative.

A.1.3 Angles for Tracking Surfaces

Solar collectors such as PTCs track the sun by moving in prescribed ways to minimize the angle of incidence of beam radiation on their surface and therefore maximize the incident direct radiation. In particular, PTCs can rotate about their axis that could have any orientation, but in practice this is usually horizontal east-west or horizontal north-south.

For a plane rotating around a horizontal east-west axis with continuous adjustment to minimize the angle of incidence [28]:

$$\cos\theta = \sqrt{1 - \cos^2\delta\sin^2\omega} \tag{A.8}$$

The slope of the surface can be calculated from:

$$\tan\beta = \tan\theta_z \left|\cos\gamma_s\right| \tag{A.9}$$

If the solar azimuth angle passes through ±90°, the surface azimuth angle of orientation will change between 0° and 180°; otherwise:

$$\gamma = \begin{cases} 0^\circ, & \text{if } \left|\gamma_s\right| < 90^\circ \\ 180^\circ, & \text{if } \left|\gamma_s\right| \geq 90^\circ \end{cases} \tag{A.10}$$

The shadowing effects of this arrangement are minimal; the principal shadowing is caused when the collector is tipped to a maximum degree south ($\delta = 23.5^\circ$) at winter solstice. In this case, the sun casts a shadow toward the collector at the north. This configuration has the advantage to approximate the full tracking in summer; however, the winter performance is depressed relative to the summer one [5].

For a plane rotating around a horizontal north-south axis with continuous adjustment to minimize the angle of incidence [28]:

$$\cos\theta = \sqrt{\cos^2\theta_z + \cos^2\delta\sin^2\omega} \tag{A.11}$$

The slope is:

$$\tan\beta = \tan\theta_z \left|\cos\left(\gamma - \gamma_s\right)\right| \tag{A.12}$$

In this arrangement, γ will be 90° or −90° depending on the sign of γ_s:

$$\gamma = \begin{cases} 90^\circ, & \text{if } \gamma_s > 0^\circ \\ -90^\circ, & \text{if } \gamma_s \leq 0^\circ \end{cases} \tag{A.13}$$

The greatest advantage of this arrangement is that very small shadowing effects are encountered when more than one collector is used. These occur only at the first and last hours of the day [5].

A.1.4 Beam Radiation on Tilted Surfaces

According to the instrument used to measure solar radiation, different relationships should be considered to identify the beam radiation which falls on a tilted surface.

Pyrheliometers are instruments able to measure the normal beam radiation, G_{bn} (also referred to as *DNI*, Direct Normal Irradiance). Therefore, if G_{bn} measurements are available, the beam radiation on a tilted surface is (see Figure A.2):

$$G_{bt} = G_{bn}\cos\theta \tag{A.14}$$

On the other hand, pyranometers measure global (i.e, direct and diffuse) solar radiation referred to the horizontal plane, G. The same quantity is generally considered in estimates of solar radiation given by empirical equations. If we only consider the direct fraction G_b, from Figure A.2 we obtain that:

$$G_{bt} = G_{bn}\cos\theta = G_b\frac{\cos\theta}{\cos\theta_z} \tag{A.15}$$

A.2 Optical Analysis

The optical analysis quantifies the amount of solar energy that actually reaches a PTC receiver. In the following sections, the parameters that influence a PTC optical efficiency will be analyzed.

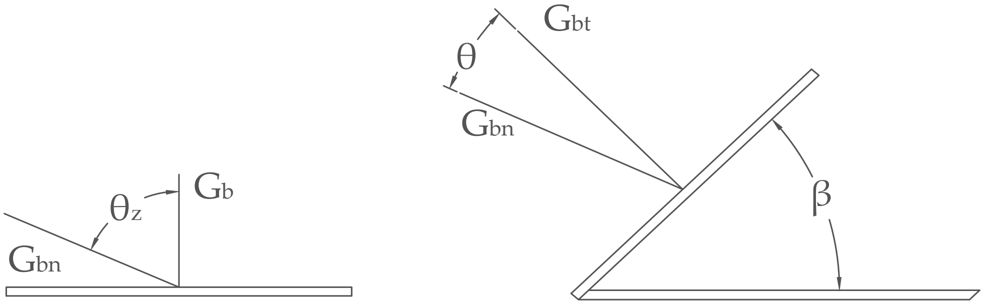

Figure A.2: Beam radiation on horizontal and tilted surfaces. Adapted from Duffie and Beckman [28].

A.2.1 Concentration Ratio

In PTCs, the concentration of solar radiation is achieved by reflecting the solar flux incident on the concentrator of aperture area A_a onto the receiver of area A_r. The concentration ratio, C, is referred to as the ratio of the aperture area to that of the receiver:

$$C = \frac{A_\mathrm{a}}{A_\mathrm{r}} \tag{A.16}$$

Generally, the higher the temperature at which energy is to be delivered, the higher should be the concentration ratio. This ratio has also an upper limit that depends on the second law of thermodynamics. Since PTCs are two-dimensional concentrating collectors, it is possible to demonstrate that the maximum achievable concentration ratio is [129]:

$$C_\mathrm{max} = \frac{1}{\sin\theta_\mathrm{m}} \tag{A.17}$$

where θ_m is the acceptance half-angle the sun subtends as seen from the earth. For tracking collectors, θ_m is limited by the size of the sun disk, small-scale errors, irregularities of the reflector surface, and tracking errors [5]. For a perfect PTC, C_max depends only on the sun disk. In this case, the half-acceptance angle is 0.267° and we get:

$$C_\mathrm{max} \simeq 215 \tag{A.18}$$

A.2.2 Geometry of a PTC

The cross-section of a PTC is shown in Figure A.3. If x is the horizontal axis and y is the vertical axis, the equation of the parabola is:

$$y = \frac{1}{4f}x^2 \tag{A.19}$$

where f is the focal length of the parabola, the distance from the focal point to the vertex.

The radiation beam of Figure A.3 is incident at the rim of the concentrator. The angle ϕ_r, made by the reflected beam radiation with the center line, is called rim angle:

$$\phi_\mathrm{r} = \tan^{-1}\left[\frac{8(f/W_\mathrm{a})}{16(f/W_\mathrm{a})^2 - 1}\right] = \sin^{-1}\left(\frac{W_\mathrm{a}}{2r_\mathrm{r}}\right) \tag{A.20}$$

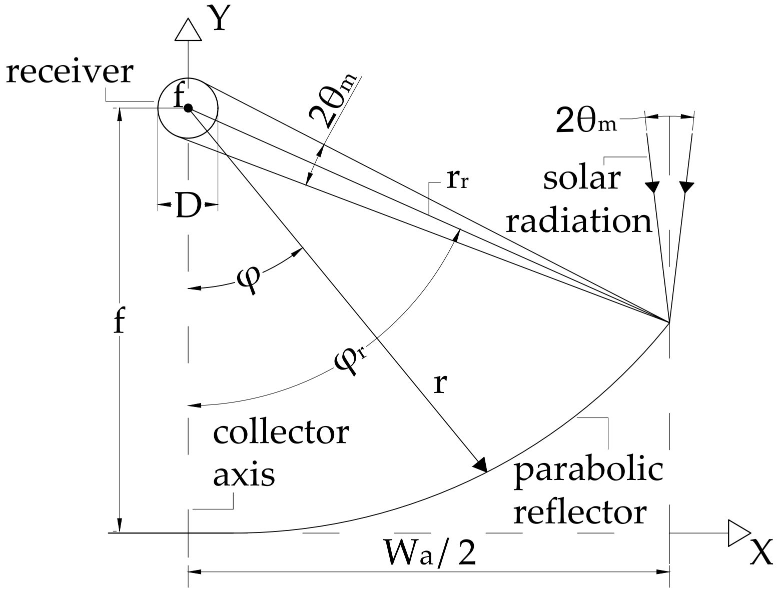

Figure A.3: Cross-section of a PTC. Adapted from Kalogirou [5].

where W_a is the aperture of the parabola and r_r is the maximum mirror radius:

$$r_\mathrm{r} = \frac{2f}{1+\cos\phi_\mathrm{r}} \tag{A.21}$$

Equation (A.20) can be rearranged to find an expression for the aperture:

$$W_\mathrm{a} = 2r_\mathrm{r}\sin\phi_\mathrm{r} = \frac{4f\sin\phi_\mathrm{r}}{1+\cos\phi_\mathrm{r}} = 4f\tan\frac{\phi_\mathrm{r}}{2} \tag{A.22}$$

The equation of the parabola can be integrated from 0 to $W_\mathrm{a}/2$ (or from 0 to ϕ_r) to find its arc length:

$$L_\mathrm{p} = \frac{f}{2}\left[\tan\frac{\phi_\mathrm{r}}{2}\sec\frac{\phi_\mathrm{r}}{2} + \ln\left(\tan\frac{\phi_\mathrm{r}}{2} + \sec\frac{\phi_\mathrm{r}}{2}\right)\right] \tag{A.23}$$

For specular reflectors of perfect alignment, the minimum size of the receiver of diameter D necessary to intercept all the reflected radiation is:

$$D = 2r_\mathrm{r}\sin\theta_\mathrm{m} \tag{A.24}$$

The proper value of the half-acceptance angle θ_m used in Equation (A.24) depends on the accuracy of the tracking mechanism and the irregularities of the reflector surface. The smaller these two effects, the closer is θ_m to the sun disk angle, resulting in a smaller image and higher concentration. In Figure A.3, the incident beam of solar radiation is a cone with an angular width of 0.53° (a half-angle θ_m of 0.267°); it leaves the concentrator at the same angle. This situation occurs only with a perfect PTC. With a real PTC, the half-acceptance angle should be increased to include the presence of errors [5]. All these are accounted for by the intercept factor, which will be discussed in Section A.2.3.

For a tubular receiver of the same length of the reflector, the concentration ratio is:

$$C = \frac{W_\mathrm{a}}{\pi D} \tag{A.25}$$

Substituting Equations (A.22) and (A.24) into Equation (A.25):

$$C = \frac{\sin\phi_\mathrm{r}}{\pi \sin\theta_\mathrm{m}} \tag{A.26}$$

C is maximum when $\sin\phi_\mathrm{r} = 1$ (i.e., when $\phi_\mathrm{r} = 90°$). Therefore, Equation (A.26) becomes:

$$C_\mathrm{max} = \frac{1}{\pi \sin\theta_\mathrm{m}} \tag{A.27}$$

The difference between this equation and Equation (A.17) is that the former applies to a PTC with a circular receiver, while the latter refers to the idealized case. In comparison with Equation (A.18), and using the same half-acceptance angle of 0.267°, the maximum concentration ratio is $C_\mathrm{max} = 1/(\pi \sin 0.267°) = 68.3$.

Finally, it can be demonstrated that, with $\phi_\mathrm{r} = 90°$, the mean focus-to-reflector distance and the reflected beam are minimized, so that the slope and tracking errors are less pronounced [30]. The collector surface area, however, decreases as the rim angle decreases. Thus, there is a temptation to use smaller rim angles because the reduction in optical efficiency is small in comparison with the saving in reflective material cost [5].

A.2.3 Optical Errors

The upper limit to the concentration ratio which can be achieved by a PTC is set by the sun width, as seen in Section A.2.1. However, in practical use, the concentration ratio is degraded below to this upper limit due to several factors:

- apparent changes in sun width and incidence angle effects;
- physical properties of the materials used in the construction;
- imperfections that may result from manufacture and/or assembly, imperfect tracking of the sun, and poor operating procedures.

A depth study of all potential errors in PTCs was presented by Güven and Bannerot [54]. Errors can be divided into two groups: random errors and non-random errors (Figure A.4). Random errors are defined as truly random natural errors and, therefore, can be represented by normal distributions with mean equal to zero. They are treated statistically and are the origin of spreading of the reflected energy distribution. Random errors are:

- scattering effects associated with the optical material used in the reflector;
- scattering effects caused by random slope errors (e.g., waviness of the reflector due to distortions occurred during manufacturing and/or assembly);
- misalignment of the PTC with the sun due to random tracking errors (which last only a very short period of time).

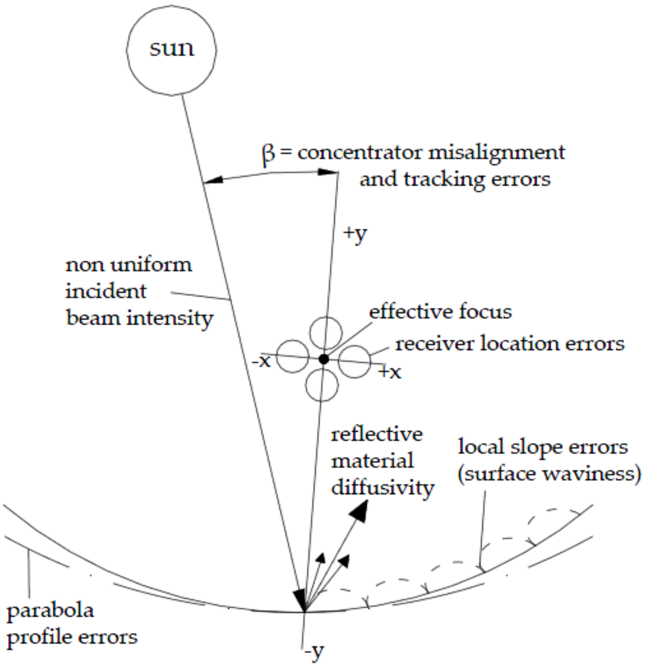

Figure A.4: Optical errors in a PTC. Adapted from Güven and Bannerot [54].

These errors can be modeled statistically by introducing a total reflected energy distribution standard deviation at normal incidence, $\sigma_{\text{tot,n}}$, which is given by:

$$\sigma_{\text{tot,n}} = \sqrt{\sigma^2_{\text{sun,n}} + \sigma^2_{\text{mirror,n}} + 4\sigma^2_{\text{slope,n}}} \tag{A.28}$$

In this equation:

- $\sigma_{\text{sun,n}}$ is the energy distribution standard deviation of the solar rays at normal incidence and solar noon;
- $\sigma_{\text{mirror,n}}$ is the standard deviation of the distribution of diffusivity of the reflective material at normal incidence;
- $\sigma_{\text{slope,n}}$ is the standard deviation of the distribution of local slope errors at normal incidence.

Non-random errors have a single deterministic value and can be related directly to anticipated errors in manufacture/assembly and/or in operation. In general, these errors will cause the central ray of the reflected energy distribution to shift from the design direction. Non-random errors can be classified as:

- Reflector profile errors (e.g., due to deflection or severe waviness of the reflector surface) which cause a permanent change in the location of the focus of the reflector, thus preventing the reflected radiation to reach the receiver. They can be quantified with the distance between the actual and ideal focus measured along the optical axis of the reflector.

- Misalignment of the trough with the sun (e.g., due to a constant tracking error) so that the position of the focus is shifted from the ideal focus and the central ray of the reflected beam can miss the receiver. The distance between the ideal focus of the concentrator and the center of the receiver can be used to quantify them.
- Misalignment of the receiver with the effective focus of the concentrator, that causes the central ray to miss the receiver. This quantity can be evaluated by defining an angle between the central solar ray and the normal to the concentrator aperture plane, β, as shown in Figure A.4.

Güven and Bannerot [54] showed that the receiver mislocation along the optical axis (y axis) degrades the optical performances more than the mislocation along the x axis (Figure A.4). Thus, the receiver mislocation along the optical axis, $(d_{\mathrm{r}})_y$, can be chosen to represent the non-random receiver location errors. Since the reflector profile errors and the receiver mislocation along y axis bring about the same effect, the parameter $(d_{\mathrm{r}})_y$ can account for both. Therefore, only two independent variables, $(d_{\mathrm{r}})_y$ and β, are sufficient to model non-random errors.

In summary, there are three error parameters that characterize optical errors: one random error, described by $\sigma_{\mathrm{tot,n}}$, and two non-random errors, described by $(d_{\mathrm{r}})_y$ and β, respectively. To quantify all the errors with a single parameter, the intercept factor is introduced. This is referred to as the fraction of reflected radiation that is incident on the absorbing surface of the receiver and it is a function of both random and non-random errors as well as the geometry of the collector:

$$\gamma = \gamma\left(\phi_{\mathrm{r}}, C, D, \sigma_{\mathrm{tot,n}}, (d_{\mathrm{r}})_y, \beta\right) \tag{A.29}$$

Random and non-random errors can be combined with the geometrical parameters of the PTC to conduct an analysis valid for all PTC geometries [54]. The expression of γ derived by Güven and Bannerot [54] is:

$$\begin{aligned} \gamma = {} & \frac{1+\cos\phi_{\mathrm{r}}}{2\sin\phi_{\mathrm{r}}} \\ & \times \int_0^{\phi_{\mathrm{r}}} \left\{ \operatorname{erf}\left(\frac{\sin\phi_{\mathrm{r}}(1+\cos\phi)(1-2d^*\sin\phi) - \pi\beta^*(1+\cos\phi_{\mathrm{r}})}{\sqrt{2}\pi\sigma^*(1+\cos\phi_{\mathrm{r}})} \right) \right. \\ & \left. - \operatorname{erf}\left(- \frac{\sin\phi_{\mathrm{r}}(1+\cos\phi)(1+2d^*\sin\phi) + \pi\beta^*(1+\cos\phi_{\mathrm{r}})}{\sqrt{2}\pi\sigma^*(1+\cos\phi_{\mathrm{r}})} \right) \right\} \\ & \times \frac{\mathrm{d}\phi}{1+\cos\phi} \end{aligned} \tag{A.30}$$

where

- $\sigma^* = \sigma_{\mathrm{tot,n}}\, C$ is the universal random error parameter;
- $d^* = (d_{\mathrm{r}})_y / D$ is the universal non-random error parameter due to receiver mislocation and reflector profile errors;
- $\beta^* = \beta C$ is the universal non-random error due to angular errors.

Equation (A.29) can be therefore simplified as:

$$\gamma = \gamma\left(\phi_{\mathrm{r}}, \sigma^*, d^*, \beta^*\right) \tag{A.31}$$

A.2.4 Geometrical Effects

Several abnormal incidence factors have the effect of reducing the optical performances of a PTC. These factors are:

- end effects;
- shading by integral bulkheads;
- intra-array shading.

Jeter et al. [55] presented a technique which ascribes to these effects the purely geometrical result of reducing the effective aperture of the concentrator.

During off-normal operation of a PTC, some of the rays reflected from near the end of the concentrator cannot reach the receiver. This loss of effective aperture is called end effect. PTCs can exhibit end effects since the receiver is usually terminated near the same cross-section plane as in the concentrator. The effective area lost to end effects is represented by the ruled region in Figure A.5 and is equal to [55]:

$$A_{\mathrm{i}} = f w \tan\theta \left(1 + \frac{w^2}{48 f^2}\right) \tag{A.32}$$

where f is the focal distance, w is the parabola width and θ is the angle of incidence.

It is possible to reduce end effects by employing a receiver longer than the trough. If this solution is adopted, two cases must be considered, as Figure A.6 shows. If $S < A$ (Figure A.6a), the ineffective area is:

$$A_{\mathrm{i},1} = A_{\mathrm{i}} - Sw \tag{A.33}$$

where S is the distance between the receiver rim and the concentrator rim. Instead, if $A < S < d$ (Figure A.6b), it can be demonstrated that the ineffective area is given by:

$$A_{\mathrm{i},2} = A_{\mathrm{i}} + (Sw' - A'_{\mathrm{i}}) - Sw \tag{A.34}$$

Clearly, if $S > d$, the ineffective area is equal to zero.

Combining the end effects with the shading produced by the receiver, the ratio of ineffective area to the whole aperture area is:

$$A_{\mathrm{f}} = \frac{A_{\mathrm{i}} + D_{\mathrm{ao}} L_{\mathrm{c}}}{A_{\mathrm{a}}} \tag{A.35}$$

where D_{ao} is the cover outer diameter and L_{c} is the length of the concentrator. Thus, the effective aperture area is:

$$A_{\mathrm{ae}} = A_{\mathrm{a}}(1 - A_{\mathrm{f}}) \tag{A.36}$$

A.2.5 Optical Properties of Materials

The following sections present equations to calculate the optical properties of the materials adopted in a PTC, in particular the absorptance of the absorber and the trasmittance of the glass cover.

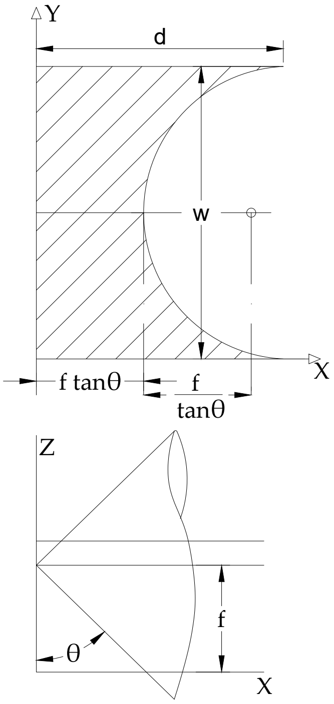

Figure A.5: Ineffective aperture area due to end effects. Adapted from Jeter et al. [55].

Specular Reflectance of the Mirror

PTCs require the use of reflecting materials to direct the beam radiation onto the receiver. Therefore, surfaces of high specular reflectance for radiation in the solar spectrum are required. Specular surfaces are usually metals or metallic coatings on smooth substrates. The specular reflectivity of such surfaces is a function of the quality of the substrate and the plating.

Specular reflectance usually depends on wavelength, so monochromatic reflectances should be integrated for the particular spectral distribution of incident beam radiation. Typical values of specular reflectance are greater than 0.90.

Glass Cover

The transmittance of the glass cover of a PTC can be obtained with adequate accuracy by considering reflection and absorption separately, and is given by the product form:

$$\tau \simeq \tau_{\mathrm{r}}\tau_{\mathrm{a}} \tag{A.37}$$

where τ_{r} is the transmittance obtained by considering only reflection losses and τ_{a} is the transmittance obtained by considering only absorption losses.

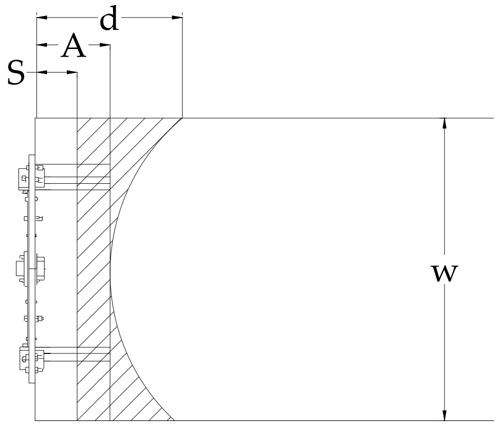

(a) $S < A$

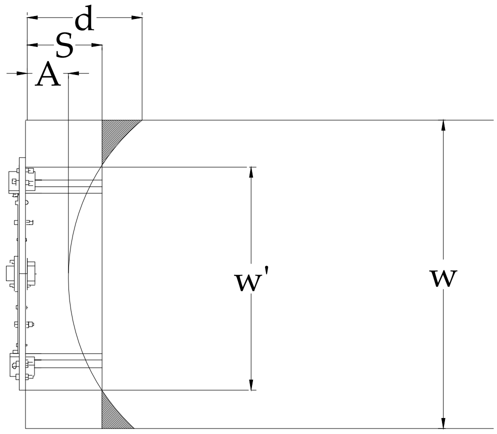

(b) $A < S < d$

Figure A.6: End effects when the receiver extends beyond the trough.

The transmittance τ_r can be evaluated from:

$$\tau_{\mathrm{r}} = \frac{1}{2}\left(\frac{1 - r_{\perp}}{1 + r_{\perp}} + \frac{1 - r_{\parallel}}{1 + r_{\parallel}}\right) \tag{A.38}$$

where $r_{\perp}$ and $r_{\parallel}$ are, respectively, the perpendicular and parallel components of the unpolarized radiation. Those components are given by the Fresnel's equations:

$$r_{\perp} = \frac{\sin^2(\theta_2 - \theta_1)}{\sin^2(\theta_2 + \theta_1)} \tag{A.39}$$

$$r_{\parallel} = \frac{\tan^2(\theta_2 - \theta_1)}{\tan^2(\theta_2 + \theta_1)} \tag{A.40}$$

In Fresnel's equations, θ_1 is the angle of incidence and θ_2 is the angle of refraction, as depicted in Figure A.7. The two angles are related by the Snell's law:

$$\frac{\sin\theta_1}{\sin\theta_2} = \frac{n_2}{n_1} \tag{A.41}$$

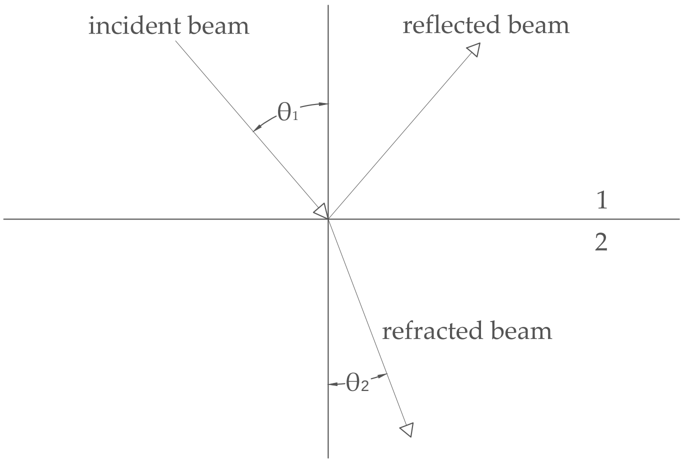

Figure A.7: Reflection and refraction at the interface of two media.

where n_1 and n_2 are the refraction indices of the two media forming the interface. Typical values of the refraction index are 1 for air and 1.526 for glass.

The absorption of radiation in a partially transparent medium is described by the Bouguer's law:

$$\tau_{\mathrm{a}} = \exp\left(-\frac{Kt}{\cos\theta_2}\right) \tag{A.42}$$

where K is the extinction coefficient, which is assumed to be a constant in the solar spectrum, and t is the thickness of the glass cover. For glass, the value of K can vary from $4\,\mathrm{m}^{-1}$ (high-quality glass) to approximately $32\,\mathrm{m}^{-1}$ (low-quality glass).

The absorptance of the cover can be calculated by the following approximate equation:

$$\alpha_{\mathrm{c}} \simeq 1 - \tau_{\mathrm{a}} \tag{A.43}$$

The reflectance of the cover can be found from:

$$\rho_{\mathrm{c}} = 1 - (\alpha_{\mathrm{c}} + \tau) \simeq \tau_{\mathrm{a}} - \tau_{\mathrm{a}}\tau_{\mathrm{r}} = \tau_{\mathrm{a}}(1 - \tau_{\mathrm{r}}) \tag{A.44}$$

Absorptance of the Absorber

The absorptance for solar radiation of ordinary blackened surfaces is a function of the angle of incidence of the radiation on the surface. However, the angular dependence of solar absorptance of most surfaces used for solar collectors is not available. An example of this dependence, valid for 0° to 90°, is [28]:

$$\begin{aligned}\alpha/\alpha_{\mathrm{n}} = 1 &- 1.5879\times10^{-3}\,\theta + 2.7314\times10^{-4}\,\theta^2 \\ &- 2.3026\times10^{-5}\,\theta^3 + 9.0244\times10^{-7}\,\theta^4 \\ &- 1.8000\times10^{-8}\,\theta^5 + 1.7734\times10^{-10}\,\theta^6 \\ &- 6.9937\times10^{-13}\,\theta^7\end{aligned} \tag{A.45}$$

where α_{n} is the solar absorptance at normal incidence and θ, the angle of incidence, is in degrees.

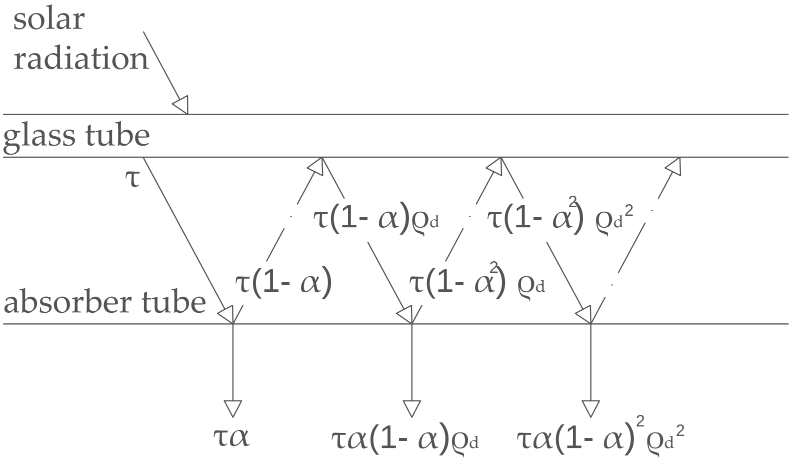

Figure A.8: Radiation transfer between the glass and the absorber.

Transmittance-Absorptance Product

Part of the radiation passing through the cover and incident on the absorber is reflected back to the cover. However, all this radiation is not lost because a portion of it is reflected back to the absorber.

The situation is shown in Figure A.8. The fraction $\tau\alpha$ of the incident beam radiation is absorbed by the absorber and the fraction $(1-\alpha)\tau$ is reflected back to the cover. This radiation, that is assumed to be diffuse and unpolarized, reaches the cover and a fraction $(1-\alpha)\tau\rho_\mathrm{d}$ is reflected back to the absorber. The term ρ_d represents the reflectance of the cover system for diffuse radiation incident from the bottom side and can be evaluated from Equation (A.44) at an angle of 60°.[1] The multiple reflection of diffuse radiation continues so that the fraction of the incident energy absorbed is

$$(\tau\alpha) = \tau\alpha\sum_{n=0}^{\infty}\big[(1-\alpha)\rho_\mathrm{d}\big]^n = \frac{\tau\alpha}{1-(1-\alpha)\rho_\mathrm{d}} \tag{A.46}$$

The term $(\tau\alpha)$ is usually referred to as the transmittance-absorptance product. It is possible to prove that a reasonable approximation of Equation (A.46) for most practical solar collectors is [28]:

$$(\tau\alpha) \simeq 1.01\tau\alpha \tag{A.47}$$

A.3 Thermal Analysis

In this section, a detailed overview of the heat transfer mechanisms participating in a PTC receiver is presented. The definition of thermal efficiency is also given.

A.3.1 Energy Balance of the Receiver

The thermal performance of a PTC can be evaluated by an energy balance that determines the fraction of the incoming radiation delivered as useful energy to the

---

[1] For a wide range of conditions encountered in solar collector applications, the equivalent angle for beam radiation, i.e. the angle which gives the same reflectance as for diffuse radiation, is 60° [28].

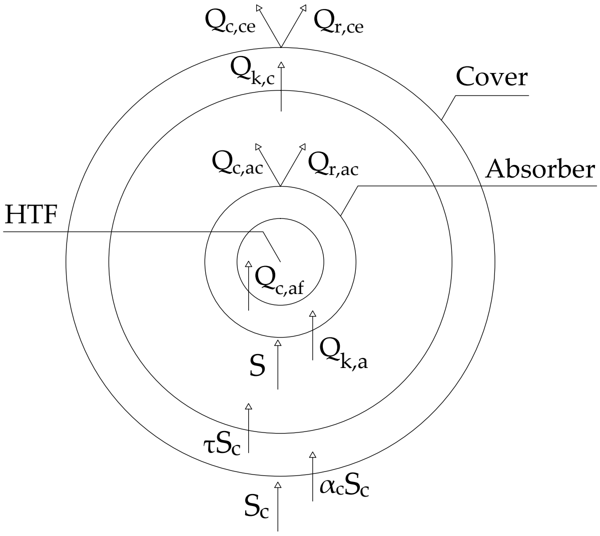

Figure A.9: Energy balance for a PTC receiver cross-section. The definition of the symbols is provided in Table A.1.

heat transfer fluid (HTF). A number of simplifying assumptions are usually adopted to model such systems [56]:

- Thermal performances are evaluated under steady-state conditions.
- Heat transfer is one-dimensional, i.e. it occurs only through the receiver radial direction. Note that the assumption of one-dimensional energy balance gives reasonable results for short receivers ($< 100\,\mathrm{m}$), but it is inadequate for longer receivers [130].
- The thermophysical and optical properties of materials are independent of temperature.
- Heat losses through support brackets are neglected.
- The sky can be considered as a blackbody at an equivalent sky temperature for long-wavelength radiation.
- The effects of dust and dirt are negligible.

Figure A.9 shows the one-dimensional steady-state energy balance for the receiver cross-section of a PTC, while Figure A.10 shows the thermal resistance model. When the beam radiation reflected by the concentrator (S_c) strikes the cover, a fraction of solar energy is transmitted to the absorber (τS_c). Only a portion of this energy, S, is effectively conducted through the absorber ($Q_\mathrm{k,a}$) and transferred to the HTF by convection ($Q_\mathrm{c,af}$), while a significant portion is loss and transmitted back by convection ($Q_\mathrm{c,ac}$) and radiation ($Q_\mathrm{r,ac}$). The energy lost by convective and radiative heat transfers is transmitted by conduction through the cover ($Q_\mathrm{k,c}$) and, along with the energy absorbed by the cover ($\alpha_\mathrm{c} S_\mathrm{c}$), is lost to the environment by convection ($Q_\mathrm{c,ce}$) and radiation ($Q_\mathrm{r,ce}$).

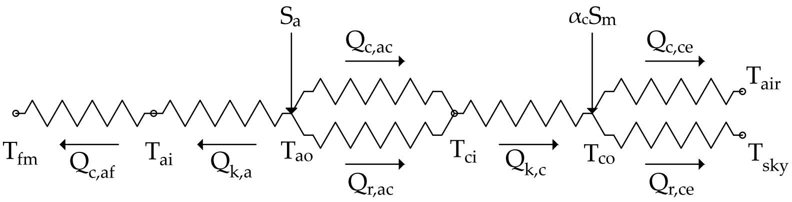

Figure A.10: Thermal resistance model of the receiver.

Table A.1: Heat fluxes involved in the energy balance of the receiver.

Heat flux	Description
S_c	Beam radiation reflected towards the receiver
$\alpha_\mathrm{c} S_\mathrm{c}$	Beam radiation absorbed by the cover
S	Beam radiation collected by the absorber
$Q_\mathrm{k,a}$	Conduction through the absorber
$Q_\mathrm{c,af}$	Convection from the absorber to the fluid
Q_u	Useful heat gain of the fluid
$Q_\mathrm{c,ac}$	Convection loss from the absorber to the cover
$Q_\mathrm{r,ac}$	Radiation loss from the absorber to the cover
$Q_\mathrm{k,c}$	Conduction loss through the cover
$Q_\mathrm{c,ce}$	Convection loss from the cover to the environment
$Q_\mathrm{r,ce}$	Radiation loss from the cover to the environment

The system of energy-balance equations is determined by applying the conservation of energy at each surface of the receiver cross-section in Figure A.9:

$$\begin{cases} S = Q_\mathrm{k,a} + Q_\mathrm{c,ac} + Q_\mathrm{r,ac} \\ Q_\mathrm{k,a} = Q_\mathrm{c,af} = Q_\mathrm{u} \\ Q_\mathrm{c,ac} + Q_\mathrm{r,ac} = Q_\mathrm{k,c} \\ Q_\mathrm{k,c} + \alpha_\mathrm{c} S_\mathrm{c} = Q_\mathrm{c,ce} + Q_\mathrm{r,ce} \end{cases} \tag{A.48}$$

The description of all terms in System (A.48) is provided in Table A.1.

The energy-balance system assumes the contribution of the diffuse component of solar radiation to be negligible.[2] With this assumption, the solar beam radiation reflected by the concentrator to the receiver is:

$$S_\mathrm{c} = \rho \gamma G_\mathrm{bt} A_\mathrm{ae} \tag{A.49}$$

where

- ρ is the specular reflectance of the concentrator;
- γ is the intercept factor given by Equation (A.30);
- G_bt is the beam radiation measured on the plane of aperture, it can be evaluated with Equations (A.14) and (A.15);

---

[2] This assumption is acceptable for all concentrators expect for those with low concentration ratio ($C = 10$ or below). For systems with low concentration ratio, part of the diffuse radiation will be reflected to the receiver, with the amount depending on the concentrator acceptance angle [28].

- A_{ae} is the effective aperture area defined in Equation (A.36).

Thus, the solar beam radiation collected in the absorber is:[3]

$$S = (\tau\alpha)S_{\mathrm{c}} = (\tau\alpha)\rho\gamma G_{\mathrm{bt}}A_{\mathrm{ae}} \tag{A.50}$$

where the term $(\tau\alpha)$ is the transmittance-absorptance product previously defined in Equation (A.46).

The following sections describe the involved heat fluxes in detail.

A.3.2 Conduction through the Absorber

The conductive heat transfer through the absorber is given by Fourier's law for concentric cylinders:

$$Q_{\mathrm{k,a}} = \frac{2\pi\lambda_{\mathrm{a}}L_{\mathrm{r}}(T_{\mathrm{ao}} - T_{\mathrm{ai}})}{\ln\left(D_{\mathrm{ao}}/D_{\mathrm{ai}}\right)} \tag{A.51}$$

where

- λ_{a} is the thermal conductivity of the absorber;
- L_{r} is the receiver length;
- T_{ao} is the outer absorber temperature;
- T_{ai} is the inner absorber temperature;
- D_{ao} is the outer absorber diameter;
- D_{ai} is the inner absorber diameter.

Note that λ_{a} is constant and independent of temperature.

A.3.3 Internal Convection

The heat transfer between the absorber and the HTF occurs by forced convection and can be expressed by the Newton's law:

$$Q_{\mathrm{c,af}} = h_{\mathrm{f}}\pi D_{\mathrm{ai}}L_{\mathrm{r}}(T_{\mathrm{ai}} - T_{\mathrm{fm}}) \tag{A.52}$$

where T_{fm} is the mean fluid temperature. The convective heat transfer coefficient of the fluid is defined as:

$$h_{\mathrm{f}} = \frac{Nu_{\mathrm{f}}\lambda_{\mathrm{f}}}{D_{\mathrm{ai}}} \tag{A.53}$$

where

- Nu_{f} is the Nusselt number of the HTF;
- λ_{f} is the thermal conductivity of the HTF.

---

[3] One should also consider the solar beam radiation which falls directly on the absorber tube, but this contribution can be ignored when the concentration ratio is high [11].

Note that λ_f is evaluated at the mean fluid temperature.

The Nusselt number depends on the type of flow through the absorber: laminar or transitional/turbulent. For a fluid circulating in a pipe, the flow can be considered laminar when the Reynolds number is lower than 2300. In this condition, the Nusselt number is independent of Reynolds and Prandtl numbers and assumes a constant value equal to 4.36.

On the other hand, the flow of the HTF is within turbulent flow region when $Re_\mathrm{f} > 4000$. If $Re_\mathrm{f} > 2300$, the Gnielinski's correlation [60] can be used:

$$Nu_\mathrm{f} = \frac{(f/8)\,(Re_\mathrm{f} - 1000)\,Pr_\mathrm{f}}{1 + 12.7(f/8)^{1/2}\left(Pr_\mathrm{f}^{2/3} - 1\right)} \tag{A.54}$$

Equation (A.54) is valid for $0.5 \leq Pr_\mathrm{f} \leq 2000$ and $2 \times 10^3 < Re_\mathrm{f} < 5 \times 10^6$. The Reynolds and Prandtl numbers must be evaluated at the mean fluid temperature. The friction factor f can be estimated from the Colebrook's iterative formula [61]:

$$\frac{1}{\sqrt{f}} = -2\log\left(\frac{\xi/D_\mathrm{ai}}{3.71} + \frac{2.51}{Re_\mathrm{f}\sqrt{f}}\right) \tag{A.55}$$

where ξ is the pipe roughness.

A.3.4 Convective Loss in the Annulus

The heat lost by convection between the absorber and the cover differs if the annulus is either evacuated or not. In the first case, heat transfer occurs by free-molecular convection; in the second case, heat flux is given by free convection. When the receiver annulus is under vacuum (i.e., when the pressure is lower than 1 torr), free-molecular convection can be evaluated as [131]:

$$Q_\mathrm{c,ac} = h_\mathrm{ann}\pi D_\mathrm{ao} L_\mathrm{r}(T_\mathrm{ao} - T_\mathrm{ci}) \tag{A.56}$$

and

$$h_\mathrm{ann} = \frac{\lambda_\mathrm{std}}{D_\mathrm{ao}/2\ln\left(D_\mathrm{ci}/D_\mathrm{ao}\right) + bk(D_\mathrm{ao}/D_\mathrm{ci} + 1)} \tag{A.57}$$

$$b = \frac{(2-a)(9\gamma - 5)}{2a(\gamma + 1)} \tag{A.58}$$

$$k = \frac{2.331 \times 10^{-20}\left[(T_\mathrm{ao} + T_\mathrm{ci})/2 + 273.15\right]}{p\delta^2} \tag{A.59}$$

where

- h_ann is the convective heat transfer coefficient of the annulus gas;
- T_ci is the inner cover temperature;
- λ_std is the thermal conductivity of the annulus gas at standard temperature and pressure;
- D_ci is the inner cover diameter;
- b is the interaction coefficient;

Table A.2: Constants for air as annulus gas at $T_{\mathrm{fm}} = 300\,^{\circ}\mathrm{C}$ [132].

λ_{std} $\left(\mathrm{W\,m^{-1}\,K^{-1}}\right)$	k (m)	δ (m)	b	γ
0.02551	0.8867	3.53×10^{-6}	1.571	1.39

- k is the mean-free path between collisions of a molecule;
- a is the accommodation coefficient;
- γ is the ratio of specific heats for the annulus gas;
- p is the annulus gas pressure;
- δ is the molecular diameter of the annulus gas.

Equation (A.56) can be used when $Ra_{\mathrm{ann}} < [D_{\mathrm{ci}}/(D_{\mathrm{ci}} - D_{\mathrm{ao}})]^4$, where Ra_{ann} is the Rayleigh number of the annulus gas. The constants for air as annulus gas are provided in Table A.2.

If the receiver annulus is not evacuated, heat transfer between the absorber and the cover occurs by free convection:

$$Q_{\mathrm{c,ac}} = \frac{2\pi\lambda_{\mathrm{eff}} L_{\mathrm{r}}}{\ln\left(D_{\mathrm{ci}}/D_{\mathrm{ao}}\right)}\left(T_{\mathrm{ao}} - T_{\mathrm{ci}}\right) \tag{A.60}$$

A recommended correlation for the effective conductive coefficient, λ_{eff}, is [133]:

$$\frac{\lambda_{\mathrm{eff}}}{\lambda_{\mathrm{ann}}} = 0.386\left(\frac{Pr_{\mathrm{ann}}}{0.861 + Pr_{\mathrm{ann}}}\right)\left(F_{\mathrm{cyl}} Ra_{\mathrm{ann}}\right) \tag{A.61}$$

where

- λ_{ann} is the thermal conductivity of air evaluated at mean temperature $(T_{\mathrm{ao}} + T_{\mathrm{ci}})/2$;
- Pr_{ann} is the Prandtl number of air evaluated at mean temperature $(T_{\mathrm{ao}} + T_{\mathrm{ci}})/2$;
- Ra_{ann} is the Rayleigh number of air evaluated at mean temperature $(T_{\mathrm{ao}} + T_{\mathrm{ci}})/2$ and characteristic length $(D_{\mathrm{ci}} - D_{\mathrm{ao}})/2$.

The form factor for concentric cylinders is given by:

$$F_{\mathrm{cyl}} = \frac{\left[\ln\left(D_{\mathrm{ci}}/D_{\mathrm{ao}}\right)\right]^4}{\left[(D_{\mathrm{ci}} - D_{\mathrm{ao}})/2\right]^3\left(D_{\mathrm{ci}}^{-3/5} + D_{\mathrm{ao}}^{-3/5}\right)^5} \tag{A.62}$$

Equation (A.61) is valid for $0.70 \leq Pr_{\mathrm{ann}} \leq 6000$ and for $10^2 < F_{\mathrm{cyl}} Ra_{\mathrm{ann}} < 10^7$. Note that if $F_{\mathrm{cyl}} Ra_{\mathrm{ann}} < 10^2$, convection is negligible and $\lambda_{\mathrm{eff}} = \lambda_{\mathrm{ann}}$. Finally, λ_{eff} cannot be less than λ_{ann}, so one should set the last equivalence if $\lambda_{\mathrm{eff}} < \lambda_{\mathrm{ann}}$.

A.3.5 Radiative Loss in the Annulus

The heat transfer by radiation between the absorber and the cover can be evaluated with the expression:

$$Q_{\mathrm{r,ac}} = \frac{\pi D_{\mathrm{ao}} L_{\mathrm{r}} \sigma (T_{\mathrm{ao}}^4 - T_{\mathrm{ci}}^4)}{1/\epsilon_{\mathrm{a}} + (1-\epsilon_{\mathrm{c}})(D_{\mathrm{ao}}/D_{\mathrm{ci}})/\epsilon_{\mathrm{c}}} \tag{A.63}$$

where

- σ is the Stefan-Boltzmann constant ($5.67 \times 10^{-8}\,\mathrm{W\,m^{-2}\,K^{-4}}$);
- ϵ_{a} is the emissivity of the absorber in the long-wavelength range;
- ϵ_{c} is the emissivity of the cover in the long-wavelength range.

In Equation (A.63), temperatures are in kelvin and emissivities are constant.

A.3.6 Conductive Loss through the Cover

The heat transfer mechanism described for the absorber is still valid for the cover. Equation (A.51) can be rewritten as:

$$Q_{\mathrm{k,c}} = \frac{2\pi \lambda_{\mathrm{c}} L_{\mathrm{r}} (T_{\mathrm{ci}} - T_{\mathrm{co}})}{\ln (D_{\mathrm{co}}/D_{\mathrm{ci}})} \tag{A.64}$$

where

- λ_{c} is the thermal conductivity of the cover;
- T_{co} is the outer cover temperature;
- D_{co} is the outer cover diameter.

λ_{c} is constant and independent of temperature.

A.3.7 External Convective Loss

As seen in Section A.3.3, the convective heat transfer between the cover and the environment can be expressed through the Newton's law:

$$Q_{\mathrm{c,ce}} = h_{\mathrm{air}} \pi D_{\mathrm{co}} L_{\mathrm{r}} (T_{\mathrm{co}} - T_{\mathrm{air}}) \tag{A.65}$$

where T_{air} is the ambient temperature. The convective heat transfer coefficient of air is defined as follows:

$$h_{\mathrm{air}} = \frac{Nu_{\mathrm{air}} \lambda_{\mathrm{air}}}{D_{\mathrm{co}}} \tag{A.66}$$

where

- Nu_{air} is the Nusselt number for air;
- λ_{air} is the conductive heat transfer coefficient for air, evaluated at the film temperature $(T_{\mathrm{co}} + T_{\mathrm{air}})/2$.

Convection will be forced or free depending on the presence or absence of wind. If wind is present, heat transfer occurs by forced convection and the following correlation can be employed [134]:

$$Nu_{\mathrm{air}} = 0.3 + \frac{0.62\, Re_{\mathrm{air}}^{1/2} Pr_{\mathrm{air}}^{1/3}}{\left[1 + (0.4/Pr_{\mathrm{air}})^{2/3}\right]^{1/4}} \left[1 + \left(\frac{Re_{\mathrm{air}}}{282\,000}\right)^{5/8}\right]^{4/5} \tag{A.67}$$

where

- Re_{air} is the Reynolds number for air evaluated at film temperature $(T_{\mathrm{co}} + T_{\mathrm{air}})/2$ and characteristic length D_{co};
- Pr_{air} is the Prandtl number for air evaluated at film temperature $(T_{\mathrm{co}} + T_{\mathrm{air}})/2$.

The correlation can be used for $Re_{\mathrm{air}} Pr_{\mathrm{air}} > 0.2$.

If there is no wind, the heat transfer between the cover and the environment will be by free convection. In this case, the correlation to be used is [135]:

$$Nu_{\mathrm{air}} = \left\{0.6 + \frac{0.387\, Ra_{\mathrm{air}}^{1/6}}{\left[1 + (0.559/Pr_{\mathrm{air}})^{9/16}\right]^{8/27}}\right\}^2 \tag{A.68}$$

This equation considers a long isothermal horizontal cylinder and it can be adopted for $10^5 < Ra_{\mathrm{air}} < 10^{12}$. Considerations made for Reynolds and Prandtl numbers in Equation (A.67) are still valid.

A.3.8 External Radiative Loss

The radiative heat transfer between the cover and the environment is caused by the temperature difference between the outer cover surface and the sky. This condition is approximated by considering a small convex gray object (the cover) in a large blackbody cavity (the sky). Therefore, the net exchanged radiation is:

$$Q_{\mathrm{r,ce}} = \epsilon_{\mathrm{c}} \pi D_{\mathrm{co}} L_{\mathrm{r}} \sigma (T_{\mathrm{co}}^4 - T_{\mathrm{sky}}^4) \tag{A.69}$$

Temperatures are in kelvin and emissivities are constant.

The sky temperature T_{sky} can be related to the dry bulb temperature T_{air} and the dew point ambient temperature T_{dp} as follows [136]:

$$T_{\mathrm{sky}} = \epsilon_{\mathrm{sky}}^{1/4} T_{\mathrm{air}} \tag{A.70}$$

where the sky emissivity is given by

$$\epsilon_{\mathrm{sky}} = 0.711 + 0.56 \left(\frac{T_{\mathrm{dp}}}{100}\right) + 0.73 \left(\frac{T_{\mathrm{dp}}}{100}\right)^2 \tag{A.71}$$

A.3.9 Thermal Efficiency

The thermal efficiency of a PTC is defined as the ratio of the useful heat gain of the HTF, Q_{u}, to the solar energy intercepted by the collector aperture area, S_{a}, and is given by:

$$\eta = \frac{Q_{\mathrm{u}}}{S_{\mathrm{a}}} = \frac{\dot{m}\, c_p (T_{\mathrm{fo}} - T_{\mathrm{fi}})}{G_{\mathrm{bt}} A_{\mathrm{a}}} \tag{A.72}$$

where:

- $\dot{m}$ is the mass flow rate of the HTF;
- c_p is the specific heat at constant pressure of the HTF;
- T_{fo} is the outlet fluid temperature;
- T_{fi} is the inlet fluid temperature;
- G_{bt} is the beam radiation measured on the plane of aperture (it must be properly evaluated by using Equations (A.14) and (A.15));
- A_{a} is the collector aperture area.

An energy balance alternative to System (A.48) can be extended to a control volume containing only the absorber. For a PTC of aperture area A_{a}, the energy balance on the cylindrical absorber yields:

$$S = Q_{\mathrm{u}} + Q_{\mathrm{l}} + \frac{\mathrm{d}E_{\mathrm{c}}}{\mathrm{d}t} \tag{A.73}$$

where

- S is the solar beam radiation collected in the absorber tube after reflection, defined by Equation (A.50);
- Q_{u} is the rate of useful heat gain;
- Q_{l} is the rate of heat loss from the absorber;
- $\mathrm{d}E_{\mathrm{c}}/\mathrm{d}t$ is the rate of internal energy storage in the collector.

Equation (A.73) can be rewritten in terms of an overall loss coefficient, U_{L}, by considering the expression:

$$Q_{\mathrm{l}} = U_{\mathrm{L}} A_{\mathrm{r}} (T_{\mathrm{r}} - T_{\mathrm{air}}) \tag{A.74}$$

where

- A_{r} is the area of the absorber surface (equal to $\pi D_{\mathrm{ao}} L_{\mathrm{r}}$);
- T_{r} is the average temperature of the absorber surface;
- T_{air} is the ambient temperature.

Substituting Equation (A.74) in (A.73), operating in steady state conditions (i.e., $\mathrm{d}E_{\mathrm{c}}/\mathrm{d}t = 0$) and rearranging terms, one gets:[4]

$$Q_{\mathrm{u}} = (\tau\alpha)\rho\gamma G_{\mathrm{bt}} A_{\mathrm{ae}} - U_{\mathrm{L}} A_{\mathrm{r}} (T_{\mathrm{r}} - T_{\mathrm{air}}) \tag{A.75}$$

The problem with this equation is that the average temperature of the absorber surface, T_{r}, is difficult to calculate or measure since it is a function of the collector design, the incident solar radiation and the entering fluid conditions. However, one can use T_{fi}, the inlet fluid temperature, instead of T_{r}, by introducing a heat removal factor F_{R}:

$$Q_{\mathrm{u}} = F_{\mathrm{R}} \left[(\tau\alpha)\rho\gamma G_{\mathrm{bt}} A_{\mathrm{ae}} - U_{\mathrm{L}} A_{\mathrm{r}} (T_{\mathrm{fi}} - T_{\mathrm{air}}) \right] \tag{A.76}$$

---

[4] Some authors define an effective transmittance-absorptance product which accounts for the reduced thermal losses due to absorption of solar radiation by the cover. However, this effect has been already considered in the energy balance of Equation (A.48), thus it will be not reconsidered here.

where

$$F_{\mathrm{R}} = \frac{\dot{m}\, c_p}{A_{\mathrm{r}} U_{\mathrm{L}}} \left[1 - \exp\left(- \frac{A_{\mathrm{r}} U_{\mathrm{L}} F^{'}}{\dot{m}\, c_p} \right) \right] \tag{A.77}$$

The heat removal factor is an important design parameter since it is a measure of the thermal resistance encountered by the absorbed radiation in reaching the HTF. From Equation (A.76), it is possible to define F_{R} as the ratio of the useful heat gain of the fluid to the gain which would occur if the absorber were at temperature T_{fi} everywhere. Note that F_{R} can range between 0 and 1.

The term $F^{'}$ is the collector efficiency factor and represents the ratio of the useful heat gain of the fluid to the gain which would occur if the whole absorber were at the local fluid temperature. It is given by:

$$F^{'} = \frac{1/U_{\mathrm{L}}}{1/U_{\mathrm{L}} + D_{\mathrm{ao}}/(h_{\mathrm{f}}\, D_{\mathrm{ai}}) + D_{\mathrm{ao}} \ln\left(D_{\mathrm{ao}}/D_{\mathrm{ai}}\right)/(2\lambda_{\mathrm{a}})} \tag{A.78}$$

where

- h_{f} is the fluid convective heat transfer coefficient defined in Equation (A.53);
- λ_{a} is the thermal conductivity of the absorber.

Equation (A.76) is the Hottel-Whillier-Bliss equation adapted for PTCs. Dividing this equation by the solar energy intercepted by the collector aperture area, S_{a}, one gets:

$$\eta = \frac{Q_{\mathrm{u}}}{S_{\mathrm{a}}} = F_{\mathrm{R}} \left[\eta_{\mathrm{o}} - \frac{U_{\mathrm{L}}}{C} \left(\frac{T_{\mathrm{fi}} - T_{\mathrm{air}}}{G_{\mathrm{bt}}} \right) \right] \tag{A.79}$$

where η_{o} is the optical efficiency of the PTC, the ratio of solar energy collected by the absorber to that intercepted by the concentrator. The optical efficiency can be written as:

$$\eta_{\mathrm{o}} = (\tau\alpha)\rho\gamma(1 - A_{\mathrm{f}}) \tag{A.80}$$

Equation (A.79) is an alternative form of Equation (A.72) and allows to determine the thermal efficiency of a PTC as a function of the term $(T_{\mathrm{fi}} - T_{\mathrm{air}})/G_{\mathrm{bt}}$.

As a general comment, it is worth noting that the concentration ratio has a relevant role in reducing the thermal losses of a PTC: from Equation (A.79), it is evident that the greater is the concentration ratio, the higher is the efficiency. Optical efficiency also assumes a decisive role.

Appendix B

Standards for PTC Testing

The performance of solar thermal collectors such as PTCs can be assessed by performing specific procedures described in standards. Standards generally followed in the solar energy field are the ISO 9806, the ANSI/ASHRAE 93, and the EN 12975-1, which will be briefly presented in this appendix. The measurements and the procedures required for testing PTCs will be discussed focusing the attention on the three most important solar collector parameters: time constant, thermal efficiency, and incident angle modifier. Due to its importance, uncertainty in thermal efficiency testing will be described extensively. Also, quality test methods will be briefly discussed.

B.1 Available Standards

Different standards can be adopted to evaluate the thermal performance of concentrating solar collectors such as PTCs. In this section, the international, US, and European standards dedicated to this purpose are presented. To date, the standards which should be considered are the ISO 9806:2013 and the ANSI/ASHRAE Standard 93-2010 (RA2014).

B.1.1 International Standards

The ISO 9806:2013 [137] defines procedures for testing fluid heating solar collectors for performance, reliability, durability, and safety under well-defined and repeatable conditions. It provides performance test methods for conducting tests outdoors under natural solar irradiance and natural/simulated wind, and for conducting tests indoors under simulated solar irradiance and wind.

The standard includes test methods for the steady-state and quasi-dynamic thermal performance of glazed and unglazed liquid heating solar collectors and steady-state thermal performance of glazed and unglazed air heating solar collectors. Collectors tested according to this standard represent a wide range of applications, including tracking concentrating collectors for process heat at low temperature.

The standard is not applicable to those collectors in which the thermal storage unit is an integral part of the collector to such an extent that the collection process cannot be separated from the storage process for the purpose of making measurements of these two processes.

The ISO 9806:2013 cancels and replaces the ISO 9806-1:1994, ISO 9806-2:1995, and ISO 9806-3:1995, which have been technically revised. It also replaces the EN

12975-2:2006.

B.1.2 US Standards

The ANSI/ASHRAE Standard 93-2010 (RA2014) [51] provides a test procedure for solar energy collectors which use single-phase fluids (liquids or gases, but not a mixture of the two phases) and have no significant internal energy storage. Collectors can be tested both indoors (under a simulated solar irradiance) and outdoors (under natural solar irradiance) to determine steady and quasi-steady[1] state thermal performance, time constants, and variations in efficiency with changes in the angle of incidence.

The standard defines its applicability to both liquid-cooled concentrating and non-concentrating collectors, and air collectors. It does not apply to those collectors in which the heat transfer fluid changes phase and the leaving transfer fluid contains vapor.

First published in 1986 [138], the standard was reaffirmed in 1991, in 2003, and again in 2010.

B.1.3 European Standards

The first two European standards adopted for testing solar collectors were the EN 12975-1:2000 [139] and the EN 12975-2:2001 [140]. The former specified requirements on durability, reliability, and safety for liquid heating solar collectors, while the latter specified test methods to validate those requirements and included three test methods for the thermal performance characterization for liquid heating collectors. Both the standards were not applicable to those collectors in which the thermal storage unit is an integral part of the collector and to tracking concentrating solar collectors.[2]

The EN 12975-1 and 12975-2 were reaffirmed in 2006. In 2010, the amendment A1:2010 was added to the EN 12975-1 to include concentrating solar collectors. As noted in Section B.1.1, the EN 19275-2:2006 has been replaced by the ISO 9806:2013.

B.2 Performance Test Computations

The performance of a PTC can be determined by calculating the instantaneous efficiency for different values of:

- inlet fluid temperature;
- ambient temperature;
- incident solar radiation.

This requires to measure experimentally, under steady state or quasi-steady state conditions:

- the mass flow rate of the HTF, $\dot{m}$;
- the inlet fluid temperature, T_{fi};

---

[1] Quasi-steady state describes solar collector test conditions when the flow rate, inlet fluid temperature, collector temperature, solar irradiance, and ambient environment have stabilized such an extent that these conditions may be considered essentially constant.

[2] EN 12975-2:2001 specified that, even though basically not applicable to tracking concentrating collectors, given quasi-dynamic testing was also applicable to most concentrating collector designs.

- the outlet fluid temperature, T_{fo};
- the ambient air temperature, T_{air};
- the beam solar radiation on the plane of aperture, $DNI \cos\theta$;
- the wind velocity, v_{air}.

The aperture area, A_{a}, and the specific heat capacity of the HTF, c_p, should also be measured with certain accuracy, since they appear in the expression of the thermal efficiency reported in Equation (B.6).

B.3 Measurement Requirements

The following measurements are the most important required to test liquid concentrating collectors glazed.

- The accuracy of the liquid flow rate measurements should be equal to or better than ±1.0% of the measured value in mass per unit time. The mass flow rate of the HTF should be the same (±10%) throughout the whole test sequence.
- Temperature measurements could require different accuracies, thus different sensors can be used (e.g., thermocouples, thermopiles, and resistance thermal detectors). In particular:
  - the inlet fluid temperature should be measured to a standard uncertainty of 0.1 K but, in order to check that the temperature is not drifting with time, a better resolution of the temperature to ±0.02 K could be required;
  - the difference between the outlet and inlet fluid temperatures should be determined to a standard uncertainty lesser than 0.05 K;
  - the ambient temperature should be measured to a standard uncertainty lesser than 0.5 K.
- The inlet pressure and the pressure drop across the collector should be measured with a device having an error lesser than 5% of the measured value or ±10 Pa.
- Pyranometers and pyrheliometers can be used for measuring solar radiation. These instruments should have minimum characteristics defined by the standards in detail and should be calibrated for solar response within one year preceding the collector tests against another instrument whose calibration uncertainty relative to recognized measurement standards is known.
- The average wind velocity should be measured to a standard uncertainty lesser than 0.5 m/s (0.25 m/s for unglazed collectors) for both indoor and outdoor testing. The measurement of the average value may be obtained either by an arithmetic average of sampled values or by a time integration over the test period.
- The collector gross area should be measured to a standard uncertainty of 0.3%.
- The specific heat capacity c_p and the density ρ of the fluid should be known to within ±1% over the range of fluid temperatures used during the tests.

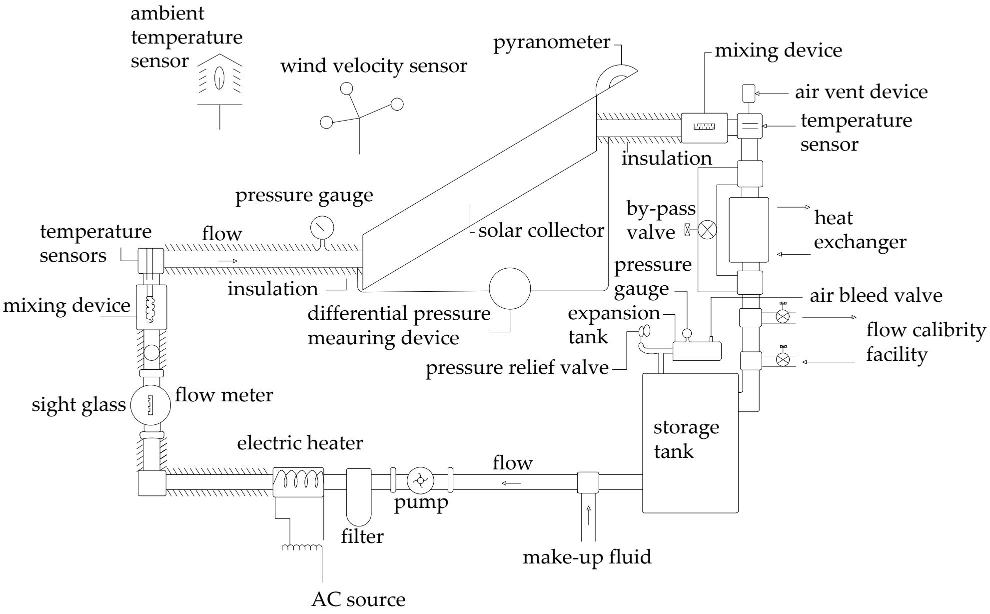

Figure B.1: Closed-loop testing configuration for liquid solar collectors. Adapted from [51].

The following correlations can be used for water at 1 bar and at a temperature between 0 and 99.5 °C. For the specific heat capacity:

$$c_p = 4.217 - 3.358 \times 10^{-3}T + 1.089 \times 10^{-4}T - 1.675 \times 10^{-6}T \\ + 1.309 \times 10^{-8}T - 3.884 \times 10^{-11}T \tag{B.1}$$

And for the density:

$$\rho = 999.85 + 6.187 \times 10^{-2}T - 7.654 \times 10^{-3}T + 3.974 \times 10^{-5}T \\ - 1.110 \times 10^{-7}T \tag{B.2}$$

Acceptable test configurations for testing liquid solar collectors are:

- closed-loop;
- open-loop;
- open-loop with fluid continuously supplied.

All these configurations are acceptable if the specified test conditions are satisfied. Figure B.1 shows an example of closed loop testing configuration when the heat transfer fluid is a liquid.

B.4 PTC Parameters

Tests are performed to determine the time response characteristics of the collector as well as how its steady-state thermal efficiency varies with the angle of incidence at various sun and collector positions. The parameters described in the following were developed to control test conditions so that a well-defined efficiency curve can be obtained with a minimum of data scatter.

B.4.1 Time Constant

The determination of the time response of a solar collector is required to evaluate the transient behavior of the collector itself and to select the proper time intervals for the quasi-steady or steady-state efficiency tests. Whenever transient conditions exist, Equation (B.6) does not govern the thermal performance of the collector, since part of the absorbed solar energy is used for heating up the collector or, if energy is lost, it results in cooling the collector. In this case, the transient behavior of a solar collector is described by Equation (A.73), and the following assumptions are considered valid:

- The beam radiation *DNI* is initially zero and is suddenly increased and held constant.
- η_o, U_L, T_air, $\dot{m}$, and c_p are considered constant during the transient period.
- The rate of change of the mean fluid temperature, T_fm, with time is related to the rate of change of the outlet fluid temperature, T_fo, with time by:

  $$\frac{\mathrm{d}T_\mathrm{fm}}{\mathrm{d}t} = K\frac{\mathrm{d}T_\mathrm{fo}}{\mathrm{d}t} \tag{B.3}$$

  where K is a dimensionless capacity factor which affects the rate at which a particular collector will heat up to steady state and to a stabilized outlet temperature, $T_\mathrm{fo,s}$. K is defined as

  $$K = \frac{\dot{m}\, c_p}{F'\, A_\mathrm{a} U_\mathrm{L}}\left(\frac{F'}{F_\mathrm{R}} - 1\right) \tag{B.4}$$

  where $F^{'}$ is the collector efficiency factor, U_L is the overall loss coefficient, and F_R is the heat removal factor (see Section A.3.9 fur further details).

With these assumptions, the collector time constant is defined as the time, t, the collector takes to go from its delta temperature with no solar radiation to 63.2% of its delta temperature at steady state conditions, given a stable exposure:

$$\frac{T_\mathrm{fo}(t) - T_\mathrm{fi}}{T_\mathrm{fo,s} - T_\mathrm{fi}} = 0.632 \tag{B.5}$$

where $T_\mathrm{fo,s}$ is the stabilized outlet temperature.

B.4.2 Thermal Efficiency

The thermal efficiency of a PTC is given by:

$$\eta = \frac{\dot{m}\, c_p (T_\mathrm{fo} - T_\mathrm{fi})}{\mathit{DNI}\cos\theta A_\mathrm{a}} = F_\mathrm{R}\left[\eta_\mathrm{o} - \frac{U_\mathrm{L}}{C}\left(\frac{T_\mathrm{fi} - T_\mathrm{air}}{\mathit{DNI}\cos\theta}\right)\right] \tag{B.6}$$

Equation (B.6) states that if the efficiency, η, is plotted as a function of $(T_\mathrm{fi} - T_\mathrm{air})/\mathit{DNI}\cos\theta$, a straight line will result considering U_L as a constant. Note that F_R depends on U_L, as Equation (A.77) shows. This straight line has the following parameters:

- the intercept is equal to $F_\mathrm{R}\eta_\mathrm{o}$;
- the slope is equal to $-\big(F_\mathrm{R}U_\mathrm{L}\big)/C$.

The thermal efficiency reaches a maximum (i.e., the intercept value) when the inlet fluid temperature equals the ambient temperature. On the contrary, the thermal efficiency is zero when the radiation level is low or the fluid temperature is as high as heat losses equal solar absorption. This last condition is called stagnation and usually occurs when no fluid flows in the collector. Collectors must be designed to withstand stagnation temperatures. The maximum temperature is given by:

$$T_{\mathrm{f,max}} = T_{\mathrm{air}} + \frac{\eta_{\mathrm{o}}\, C\, \mathit{DNI}}{U_{\mathrm{L}}} \tag{B.7}$$

It is worth noting that U_{L} is not always a constant but may be a function of the temperature of the absorber and of weather conditions. Similarly, the optical efficiency, η_{o}, varies with the angle of incidence.

B.4.3 Incident Angle Modifier

The optical efficiency in Equation (B.6) depends on the angle of incidence and for off-normal incidence angles is difficult to be described analytically and measured, since it strongly depends on the collector geometry and optics. However, the actual optical efficiency can be replaced by its value at normal incidence, $\eta_{\mathrm{o,n}}$, if a factor called incident angle modifier, $K_{\tau\alpha}$, is provided. The incident angle modifier is given by:

$$K_{\tau\alpha} = \frac{(\tau\alpha)\rho\gamma(1 - A_{\mathrm{f}})}{\left[(\tau\alpha)\rho\gamma\right]_{\mathrm{n}}(1 - A_{\mathrm{f,n}})} = \frac{\eta_{\mathrm{o}}}{\eta_{\mathrm{o,n}}} \tag{B.8}$$

therefore Equation (B.6) becomes

$$\eta = F_{\mathrm{R}}\left[K_{\tau\alpha}\eta_{\mathrm{o,n}} - \frac{U_{\mathrm{L}}}{C}\left(\frac{T_{\mathrm{fi}} - T_{\mathrm{air}}}{\mathit{DNI}}\right)\right] \tag{B.9}$$

Using the incident angle modifier, the thermal efficiency of a PTC can be determined at normal or near-normal incidence conditions. In this way, $K_{\tau\alpha} \simeq 1$ and the intercept of the efficiency curve is equal to $F_{\mathrm{R}}\eta_{\mathrm{o,n}}$. A separate measurement is conduced to determine the value of $K_{\tau\alpha}$ so that the collector performances can be predicted under a wide range of conditions and/or time of day using Equation (B.9).

B.5 Performance Test Procedures

To correctly characterize a glazed PTC, outdoor tests should be performed by satisfying the following conditions.

- The fluid flow rate should be set at approximately 0.02 kg/s per square meter of collector gross area. It should be held stable to within ±2% of the set value during each test period, and should not vary by more than ±10% of the set value from one test period to another. In any case, transitional regimes should be avoided.
- The hemispherical solar irradiance at the plane of the collector aperture should be greater than 700 W/m^2.
- The angle of incidence of direct solar radiation at the collector aperture should be in the range in which the incident angle modifier for the collector varies by

no more than ±2% from its value at normal incidence. In order to characterize the PTC performance at various angles, an incident angle modifier must be determined (Section B.4.3).

- The average value of wind velocity parallel to the collector aperture should be 3 ± 1 m/s.
- The inlet fluid temperature should remain constant within the operating range. In fact, small variations in the inlet temperature could lead to errors in the estimated thermal efficiency.
- Data points should be obtained for at least four different inlet fluid temperatures spaced evenly over the operating temperature range of the collector. A minimum of four independent data points should be registered for each inlet fluid temperature, for a total of sixteen data points. It is important that one inlet temperature is selected such that it lies within ±3 K of the ambient temperature, in order to obtain an accurate determination of the incident angle modifier.
- The ambient temperature should be lesser than 30 °C.

If the previous conditions are satisfied, the following testing procedure allows to determine the parameters which characterize the performance of a PTC, as described in Section B.4.

1. At first, a performance test is conduced on the PTC to determine its time constant. The inlet fluid temperature is adjusted as closely as possible to the ambient temperature and is controlled while circulating the HTF through the collector at the specified flow rate and maintaining steady or quasi-steady state conditions with the collector covered. Then, the incident solar radiation is abruptly increased to a value greater than $700\,\mathrm{W/m^2}$. Inlet and outlet fluid temperatures must be continuously monitored as functions of time until a steady state condition is achieved, that is when:

$$\Delta T_\mathrm{s} = T_\mathrm{fo,s} - T_\mathrm{fi} \tag{B.10}$$

   The actual time constant is the time t required to the collector to reach the condition expressed in Equation (B.5).

2. When the first test is completed, a series of thermal efficiency tests are carried out at near-normal incident conditions. The angle of incidence should be in the range in which the incident angle modifier varies by no more than ±2% from the normal incidence value. An acceptable evenly spaced distribution of inlet temperatures can be obtained by setting $(T_\mathrm{fi} - T_\mathrm{air})$ to 0%, 30%, 60%, and 90% of the value of $(T_\mathrm{fi} - T_\mathrm{air})$ reached at the maximum tested inlet temperature and at a given ambient temperature. At least four data points should be taken for each value of T_fi at steady or quasi-steady state conditions. The ambient temperature should not vary by more than ±1.5 °C.

3. Finally, the PTC incident angle modifier is determined as a function of the angle of incidence. The orientation of the collector should be such that the collector is maintained within ±2.5° of the angle of incidence for which the test is being conducted. For PTCs, the collector should be oriented so that the test incident angles are, approximately, 0, 30, 45, and 60°. It is recommended that these

data be taken during a single day. For each data point, the inlet temperature should be as closely as possible (±1 °C) to the ambient temperature, so that from Equation (B.9) one gets:

$$K_{\tau\alpha} \simeq \frac{\eta}{F_{\mathrm{R}}\eta_{\mathrm{o,n}}} \tag{B.11}$$

Since $F_{\mathrm{R}}\eta_{\mathrm{o,n}}$ will have already been obtained as the intercept of the efficiency curve, the values of $K_{\tau\alpha}$ can be computed for different angles of incidence with Equation (B.11). An expression for the incident angle modifier, i.e. $K_{\tau\alpha}(\theta)$, can be obtained by using curve fitting methods.

B.6 Uncertainty in PTC Thermal Efficiency

One of the aims of the performance tests is to determine the thermal efficiency of a PTC. But this parameter is the result of a series of measurements, thus it is only an approximation of the real value since all measurements are affected by uncertainty. The repetition of a measurement does not guarantee that the obtained results are always the same; instead, it is usually verified that the results of a repeated measurement are included in a well-defined range of values.

The result of a measurement should be expressed in a reliable form to be used in a useful way. In fact, without such form, the results of a measurement cannot be compared one another. This form can be expressed in terms of uncertainty of a measurement. Uncertainty in measurement is defined by international standards. One of these standards is the GUM, "Guide to the expression of Uncertainty in Measurement" [141], to which we will refer to develop an analysis of the uncertainty in PTC thermal efficiency testing.

As discussed in the previous sections, the thermal efficiency η cannot be measured directly, since it depends on N other input quantities through the following relationship:

$$\eta = f(\rho, \dot{V}, c_p, \Delta T, DNI, \theta, A_{\mathrm{a}}) = \frac{\rho \dot{V} c_p \Delta T}{DNI \cos\theta A_{\mathrm{a}}} \tag{B.12}$$

where ρ is the fluid density, $\dot{V}$ is the volumetric flow rate, and ΔT is the temperature difference between the outlet and the inlet of the receiver.

The best estimate (or expectation) of η can be written as:

$$\bar{\eta} = f(\bar{\rho}, \overline{\dot{V}}, \overline{c_p}, \overline{\Delta T}, \overline{DNI}, \bar{\theta}, \overline{A_{\mathrm{a}}}) = \frac{\bar{\rho}\overline{\dot{V}}\,\overline{c_p}\,\overline{\Delta T}}{\overline{DNI}\cos\bar{\theta}\,\overline{A_{\mathrm{a}}}} \tag{B.13}$$

where the bars indicate the best estimate of the each quantity. The following sections describe how to calculate the aforementioned estimates, their uncertainties, and the global uncertainty of the estimate of the thermal efficiency.

B.6.1 Type A and B Uncertainties of the Input Quantities

According to the GUM recommendations, uncertainties are classified into two types:

- Type A uncertainties are evaluated by means of a statistical analysis of series of observations;
- Type B uncertainties are evaluated by methods different from the statistical analysis.

The information used to estimate Type A uncertainty derives from the experiment/measurement being studied, while Type B uncertainty derives from external sources, e.g. previous measurements, experience or general knowledge of the properties of the used materials/instruments, data declared by the manufacturer, etc.

When an input quantity X is obtained experimentally by repeated measurements, uncertainty must be evaluated according to the Type A approach. Let us consider N statistically independent observations x_i of X; the best estimate of X is the arithmetic mean (or mean) of the N observations x_i:

$$\bar{x} = \frac{1}{N}\sum_{i=1}^{N} x_i \tag{B.14}$$

The best estimate of $\bar{x}$ is its standard deviation $\sigma(\bar{x})$, called experimental standard deviation of the mean and given by:

$$\sigma(\bar{x}) = \sqrt{\frac{1}{N(N-1)}\sum_{i=1}^{N}(x_i - \bar{x})^2} \tag{B.15}$$

The experimental standard deviation of the mean indicates how well $\bar{x}$ estimates the expectation of X. In other words, $\sigma(\bar{x})$ can be considered as a measure of the uncertainty of $\bar{x}$ and is defined Type A standard uncertainty:

$$u_{\mathrm{A}}(\bar{x}) = \sigma(\bar{x}) \tag{B.16}$$

As concerns the thermal efficiency of a PTC, u_{A} should be generally calculated for $\overline{\dot{V}}$, $\overline{\Delta T}$, and $\overline{DNI}$.

For an estimate $\bar{x}$ of an input quantity X which has not been obtained from repeated observations, the associated estimated uncertainty is evaluated by scientific judgment based on all of the available information on the possible variability of X. For example, when it is possible to know the upper (a^+) and lower (a^-) bounds assumed by X and there is no specific knowledge about the possible values of X within the interval, one can assume that it is equally probable for X to lie anywhere within it; in other words, a uniform (or rectangular) distribution of possible values can be considered. In this case, the Type B standard uncertainty associated to the expectation of X is:

$$u_{\mathrm{B}}(\bar{x}) = \sqrt{\frac{(a^+ - a^-)^2}{12}} \tag{B.17}$$

Finally, the Type A and B uncertainties of the estimate of an input quantity X can be combined together through the following expression:

$$u(\bar{x}) = \sqrt{u_{\mathrm{A}}^2(\bar{x}) + u_{\mathrm{B}}^2(\bar{x})} \tag{B.18}$$

where $u(\bar{x})$ denotes the combined uncertainty of the estimate of the input quantity.

B.6.2 Law of Propagation of Uncertainty

The law of propagation of uncertainties allows to calculate the uncertainty of the estimate of an output quantity Y when the uncertainty of the estimates of its input quantities X_i are known. Referring to the purpose of the present work, the law allows to calculate the combined uncertainty of $\bar{\eta}$ given the combined uncertainties of the estimates of its input quantities (see Equation B.13). It is necessary to consider two different input quantities:

- independent (or uncorrelated);
- interdependent (or correlated).

If all the input quantities are independent, the combined standard uncertainty of the estimate of the output is given by:

$$u_{\text{ind}}(\overline{y}) = \sqrt{\sum_{i=1}^{N} \left(\frac{\partial f}{\partial \overline{x_i}} \right) u^2(\overline{x_i})} \tag{B.19}$$

Considering for f the expression given in Equation B.13, the law of propagation of uncertainty for the thermal efficiency can be written as:

$$\begin{split} \frac{u_{\text{ind}}(\overline{\eta})}{\overline{\eta}} = \Bigg[\left(\frac{u(\overline{\rho})}{\overline{\rho}} \right)^2 + \left(\frac{u(\overline{\dot{V}})}{\overline{\dot{V}}} \right)^2 + \left(\frac{u(\overline{c_p})}{\overline{c_p}} \right)^2 + \left(\frac{u(\overline{\Delta T})}{\overline{\Delta T}} \right)^2 + \\ \left(\frac{u(\overline{DNI})}{\overline{DNI}} \right)^2 + \left(\frac{u(\overline{\theta})}{\overline{\theta}} \right)^2 + \left(\frac{u(\overline{A_\text{a}})}{\overline{A_\text{a}}} \right)^2 \Bigg]^{\frac{1}{2}} \end{split} \tag{B.20}$$

Otherwise, if among two or more input quantities exist a certain degree of correlation (e.g., the quantities are estimated with the same instrument), it is necessary to consider the more general case of law of propagation of uncertainty which can be expressed as:

$$u_{\text{dep}}(\overline{y}) = \sqrt{\sum_{i=1}^{N} \sum_{j=1}^{N} \frac{\partial f}{\partial \overline{x_i}} \frac{\partial f}{\partial \overline{x_j}} u(\overline{x_i}, \overline{x_j})} \tag{B.21}$$

where $u(\overline{x_i}, \overline{x_j})$ is the estimated covariance, a parameter that exhibits the degree of statistical dependence among the estimates of two input quantities:

$$u(\overline{x_i}, \overline{x_j}) = \frac{1}{N(N-1)} \sum_{i,j=1}^{N} (x_i - \overline{x_i})(x_j - \overline{x_j}) \tag{B.22}$$

B.7 Quality Test Methods

In addition to tests which provide the performance characteristics of a PTC, it is also important to conduce tests to determine the quality of a collector. Therefore, all the available standards include quality tests necessary to verify the resistance of a solar collector to different environmental conditions.

These tests are briefly described in the following list, valid for liquid non-organic solar collectors, and should be carried out in the reported sequence. It is suggested to consult one of the standards discussed in Section B.1 if further information is required.

1. Internal pressure test: the fluid channels should be tested to verify the extent to which they can withstand the pressures which they might meet in service.
2. High-temperature resistance test: a collector should withstand high temperature and irradiance levels without failures (e.g., glass breakage, collapse of plastic cover, melting of plastic absorber, etc.).
3. Standard stagnation temperature.

4. Exposure and pre-exposure test: it provides a low-cost reliability test sequence indicating (or simulating) operating conditions which are likely to occur during real service.
5. External thermal shock test: it assesses the capability of a collector to withstand thermal shocks such as rainstorms or hot sunny days without a failure.
6. Internal thermal shock test: to check the capability of the collector to withstand a cold HTF on hot sunny days without a failure.
7. Rain penetration test: applicable only for glazed collectors, it assesses the extent to which glazed collectors are resistant to rain penetration.
8. Freeze resistance test.
9. Mechanical load test with positive and negative pressure: the former is necessary to check if the transparent cover of the collector, the collector box, and the fixings are able to resist the positive pressure load due to the effect of wind and snow, while the latter to assess the deformation and the extent to which the collector box and the fixings are able to resist uplift forces caused by the wind.
10. Impact resistance test: to verify the resistance of a collector to the effect of impacts caused by hailstones.

Appendix C

Nomenclature

C.1 Latin Symbols

AAD	Average absolute deviation (%)
A	Area (m^2)
A_f	Ratio of ineffective area to the whole aperture area
$A_\mathrm{i}^{'}$	Area of the parabolic segment (m^2)
a	Accommodation coefficient, thermal efficiency intercept
B	Day of the year factor (°)
b	Interaction coefficient, thermal efficiency slope (W/(m^2 K))
C	Concentration ratio
COR	Cooker opto-thermal ratio (°C/(W/m^2))
c	Specific heat (J/(kg K)
D	Diameter (m)
d	Intersection of the bounding parabola with the rim of the trough (m)
d^*	Universal non-random error parameter due to receiver mislocation and reflector profile errors
$(d_\mathrm{r})_y$	Receiver mislocation along the optical axis (m)
DNI	Direct normal irradiance (W/m^2)
E	Equation of time (min), energy (J)
$F^{'}$	Heat exchange efficiency factor
F_1	First figure of merit (°C/(W/m^2))
F_2	Second figure of merit

F_{cyl}	Form factor for concentric cylinders
F_{R}	Heat removal factor
f	Focal length/distance (m), friction factor, frequency (Hz), function
G	Radiation intensity ($\mathrm{W/m^2}$)
H	Global radiation on the horizontal plane for the monthly average day ($\mathrm{kWh/m^2}$)
h_{air}	Convective heat transfer coefficient ($\mathrm{W/(m^2\,K)}$)
I	Local intensity in the medium ($\mathrm{W/m^2}$)
K	Extinction coefficient (1/m), capacity factor
$K_{\tau\alpha}$	Incident angle modifier
k	Mean-free path between collisions of a molecule (m)
L_{m}	Length (m)
L_{loc}	Longitude (°)
L_{st}	Standard meridian for the local time zone (°)
MAD	Maximum average deviation
m	Mass (kg)
$\dot{m}$	Mass flow rate (kg/s)
n	Day of the year, refractive index, rotating speed (RPM)
Nu	Nusselt number
P	Power (W), cooking power (W)
Pr	Prandtl number
p	Pressure (bar), annulus gas pressure (mmHg), magnetic poles
Q	Heat flux (W)
R^2	Coefficient of determination
Ra	Rayleigh number
Re	Reynolds number
RH	Relative humidity
$RMSE$	Root mean square error
r	Radius (m), specular reflectance, local mirror radius (m)
r_{r}	Mirror radius (m)
S	Distance between the receiver rim and the concentrator rim (m), beam radiation (W)

s	Electrical slip
T^*	Operative term (°C/(W/m^2))
T	Temperature (°C)
t	Time (s), time constant (s), boiling time (s), thickness of the cover (m)
U_L	Overall loss coefficient (W/(m^2 K))
u	Uncertainty
$\dot{V}$	Volumetric flow rate (m^3/s)
v	Velocity (m/s)
W	Aperture (m)
w	Aperture of the parabola (m)
$w^{'}$	Aperture of the parabolic segment (m)
X	Input quantity
x	Abscissa, input observation
Y	Output quantity
y	Ordinate
z	Height

C.2 Greek Symbols

α	Absorptance, altitude angle (°)
β	Slope (°), angle between the central solar ray and the normal to concentrator aperture plane (°)
β^*	Universal non-random error due to angular errors (°)
γ	Azimuth angle (°), intercept factor, ratio of specific heats for the annulus gas
δ	Declination (°), molecular diameter of the annulus gas (m)
ϵ	Emissivity
ζ	Friction factor
η	Thermal efficiency
η_o	Optical efficiency
θ	Angle of incidence (°)
θ_m	Half-acceptance angle (°)

θ_z	Zenith angle (°)
λ	Wavelength (nm), thermal conductivity (W/(m K))
μ	Dynamic viscosity (Pa s)
ξ	Roughness (m)
π	Pi
ρ	Reflectance, density ($\mathrm{kg/m^3}$)
$\boldsymbol{\sigma}$	Stefan-Boltzmann constant ($\mathrm{W/(m^2\,K^4)}$)
σ^*	Universal random error parameter
σ	Standard deviation
τ	Transmittance
$(\tau\alpha)$	Transmittance-absorptance product
Φ	Nanoparticle volume fraction
ϕ	Latitude (°), angle between the center line and a generic beam reflected at the focus (°), nanoparticle mass fraction
ϕ_r	Rim angle (°)
ω	Hour angle (°), angular speed (°)

C.3 Subscripts

a	Absorber, absorption, aperture
air	Air
amb	Ambient
ann	Annulus
av	Average
b	Beam
bf	Base fluid
c	Cover, collector, convective, characteristic
d	Diffuse
dep	Dependent
dp	Dew point
e	Effective, environment

eff	Effective
exp	Experimental
f	Fluid
g	Glass
i	Inner, inlet, ineffective
ind	Independent
k	Conductive
l	Loss
max	Maximum
m	Mean, mirror
n	Normal
nf	Nanofluid
np	Nanoparticle
o	Outer, outlet
r	Receiver, radiative, reflection, refraction
ref	Reference
s	Solar, stabilized, specific, standard
std	Standard
t	Tilted
tot	Total
u	Useful
x	Stagnation
$\|\|$	Parallel
$\perp$	Perpendicular

C.4 Acronyms

AISI	American Iron and Steel Institute
ANSI	American National Standards Institute
ASHRAE	American Society of Heating, Refrigerating and Air-Conditioning Engineers
CJC	Cold Junction Compensation
CPC	Compound Parabolic Collector
CSP	Concentrated Solar Power
DASC	Direct Absorption Solar Collector
DIISM	Department of Industrial Engineering and Mathematical Sciences
EN	European Standard
ENEA	Italian National Agency for New Technologies, Energy and Sustainable Economic Development
EPS	Extruded Polyester
ETC	Evacuated Tube Collector
EUR	Euro
FLC	Fresnel Lens Collector
FPC	Flat Plate Collector
GMT	Greenwich Mean Time
GUM	Guide to the expression of Uncertainty in Measurement
HFC	Heliostat Field Collector
HTF	Heat Transfer Fluid
HWB	Hottel-Whillier-Bliss
IAPWS	International Association for the Properties of Water and Steam
IEA	International Energy Agency
ISO	International Organization for Standardization
LFR	Linear Fresnel Collector
NIP	Normal Incidence Pyrheliometer
PCM	Phase Change Material
PDR	Paraboloid Dish Reflector
P&I	Piping and Instrumentation

PTC	Parabolic Trough Collector
PVC	Polyvinyl Chloride
RTD	Resistance Temperature Detector
SBC	Solar Box Cooker
SEGS	Solar Electric Generating System
TIM	Transparent Insulation Material
TMY	Typical Meteorological Year
UNIVPM	Marche Polytechnic University
USA	United States of America
USD	United States Dollar
UV	Ultraviolet
VARTM	Vacuum Assisted Resin Transfer Molding
XPS	Extruded Polystyrene

Bibliography

[1] A Eisentraut and A Brown. “Heating without global warming: market developments and policy considerations for renewable heat”. In: *Paris: International Energy Agency* (2014) (cit. on p. 1).

[2] *Key Issues for Renewable Heat in Europe – Solar Industrial Process Heat – State of the Art – WP3, Task 3.5.* European Solar Thermal Industrial Federation. 2006 (cit. on p. 1).

[3] WC Turkenburg. “Renewable energy technologies”. In: *World Energy Assessment: Energy and the Challenge of Sustainability* (2000), pp. 219–272 (cit. on p. 1).

[4] SA Kalogirou. “The potential of solar industrial process heat applications”. In: *Applied Energy* 76.4 (2003), pp. 337–361 (cit. on pp. 2, 72).

[5] SA Kalogirou. *Solar Energy Engineering: Processes and Systems.* Second edition. Processes and Systems Series. Elsevier Science, 2013 (cit. on pp. 2, 4, 7, 9, 10, 18, 19, 23, 37, 51, 53, 102–105).

[6] E Cuce and PM Cuce. “A comprehensive review on solar cookers”. In: *Applied Energy* 102 (2013), pp. 1399–1421 (cit. on pp. 2, 13–15, 20, 71, 98).

[7] SD Pohekar, D Kumar, and M Ramachandran. “Dissemination of cooking energy alternatives in India – A review”. In: *Renewable and Sustainable Energy Reviews* 9.4 (2005), pp. 379–393 (cit. on p. 2).

[8] NM Nahar. “Performance and testing of a hot box storage solar cooker”. In: *Energy Conversion and Management* 44.8 (2003), pp. 1323–1331 (cit. on pp. 2, 16).

[9] F Yettou, B Azoui, A Malek, A Gama, and NL Panwar. “Solar cooker realizations in actual use: An overview”. In: *Renewable and Sustainable Energy Reviews* 37 (2014), pp. 288–306 (cit. on pp. 2, 15).

[10] RM Muthusivagami, R Velraj, and R Sethumadhavan. “Solar cookers with and without thermal storage – A review”. In: *Renewable and Sustainable Energy Reviews* 14.2 (2010), pp. 691–701 (cit. on pp. 2, 12–14, 16).

[11] SP Sukhatme and JK Nayak. *Solar Energy: Principles of Thermal Collection and Storage.* Tata McGraw-Hill Publishing Company, 2008 (cit. on pp. 4, 6–11, 16–20, 115).

[12] W Stine and M Geyer. *Power from the Sun.* 2001. URL: `http://www.powerfromthesun.net` (cit. on pp. 5–8, 11, 12).

[13] PA Funk and DL Larson. “Parametric model of solar cooker performance”. In: *Solar Energy* 62.1 (1998), pp. 63–68 (cit. on p. 13).

[14] SS Nandwani. “Solar cookers – Cheap technology with high ecological benefits”. In: *Ecological Economics* 17.2 (1996), pp. 73–81 (cit. on p. 13).

[15] BP Kerr and J Scott. “Use of the solar panel cooker for medical pressure steam sterilization”. In: *Kerr-Cole Sustainable Living Center. Taylor, AZ* (2006), p. 6 (cit. on p. 14).

[16] L Anderson and R Palkovic. *Cooking with Sunshine.* Da Capo Press, Perseus Books Group. URL: `http://www.jknappcommunications.com/cookingwithsunshine/index.htm` (cit. on p. 14).

[17] ML Ghai and TD Bansal. “Design of reflector type direct solar cooker”. In: *Journal of Scientific & Industrial Research* 12 (1953), pp. 165–175 (cit. on p. 14).

[18] AMA Khalifa, MMA Taha, and M Akyurt. “Design, simulation, and testing of a new concentrating type solar cooker”. In: *Solar Energy* 38.2 (1987), pp. 79–88 (cit. on p. 15).

[19] GN Tiwari and YP Yadav. “A new solar cooker design”. In: *Energy Conversion and Management* 26.1 (1986), pp. 41–42 (cit. on p. 15).

[20] MA Al-Saad and BA Jubran. “The performance of a low cost clay solar cooker”. In: *Renewable Energy* 1.5-6 (1991), pp. 617–621 (cit. on p. 15).

[21] AV Sonune and SK Philip. “Development of a domestic concentrating cooker”. In: *Renewable Energy* 28.8 (2003), pp. 1225–1234 (cit. on p. 15).

[22] H Kurt, E Deniz, and Z Recebli. “An investigation into the effects of box geometries on the thermal performance of solar cookers”. In: *International Journal of Green Energy* 5.6 (2008), pp. 508–519 (cit. on p. 15).

[23] N Kumar, T Chavda, and HN Mistry. “A truncated pyramid non-tracking type multipurpose domestic solar cooker/hot water system”. In: *Applied Energy* 87.2 (2010), pp. 471–477 (cit. on p. 15).

[24] R Abu-Malouh, S Abdallah, and IM Muslih. “Design, construction and operation of spherical solar cooker with automatic sun tracking system”. In: *Energy Conversion and Management* 52.1 (2011), pp. 615–620 (cit. on p. 15).

[25] MRI Ramadan, S Aboul-Enein, and AA El-Sebaii. “A model of an improved low cost-indoor-solar-cooker in Tanta”. In: *Solar & Wind Technology* 5.4 (1988), pp. 387–393 (cit. on p. 16).

[26] K Schwarzer and MEV Da Silva. “Solar cooking system with or without heat storage for families and institutions”. In: *Solar Energy* 75.1 (2003), pp. 35–41 (cit. on p. 16).

[27] SD Sharma, D Buddhi, RL Sawhney, and A Sharma. “Design, development and performance evaluation of a latent heat storage unit for evening cooking in a solar cooker”. In: *Energy Conversion and Management* 41.14 (2000), pp. 1497–1508 (cit. on pp. 16, 98).

[28] JA Duffie and WA Beckman. *Solar Engineering of Thermal Processes.* Fourth edition. Wiley, 2013 (cit. on pp. 16, 18, 19, 29–31, 38, 51, 99–103, 111, 112, 114).

[29] H Schweiger, J F. Mendes, N Benz, K Hennecke, G Prieto, M Gusi, and H Gonçalves. “The potential of solar heat in industrial processes. A state of the art review for Spain and Portugal”. In: *Proceedings of Eurosun.* 2000 (cit. on p. 18).

[30] GW Treadwell. “Design considerations for parabolic-cylindrical solar collectors”. In: *Sharing the Sun: Solar Technology in the Seventies*. Vol. 2. 1976, pp. 235–252 (cit. on pp. 21, 23, 105).

[31] A Thomas and HM Guven. “Parabolic trough concentrators – Design, construction and evaluation”. In: *Energy Conversion and Management* 34.5 (1993), pp. 401–416 (cit. on p. 21).

[32] SA Kalogirou, P Eleftheriou, S Lloyd, and J Ward. “Low cost high accuracy parabolic troughs construction and evaluation”. In: *Renewable Energy* 5.1 (1994), pp. 384–386 (cit. on p. 22).

[33] SA Kalogirou, S Lloyd, J Ward, and P Eleftheriou. “Design and performance characteristics of a parabolic-trough solar-collector system”. In: *Applied Energy* 47.4 (1994), pp. 341–354 (cit. on pp. 22, 40).

[34] E Lüpfert, E Zarza, M Geyer, P Nava, J Langenkamp, W Schiel, A Esteban, R Osuna, and E Mandelberg. “Eurotrough collector qualification complete - Performance test results from PSA”. In: *ISES Solar World Congress, Göteborg, Sweden*. 2003 (cit. on p. 22).

[35] MJ Brooks, I Mills, and TM Harms. “Design, construction and testing of a parabolic trough solar collector for a developing-country application”. In: *Proceedings of the ISES Solar World Congress, Orlando, FL*. 2005, pp. 6–12 (cit. on pp. 22, 29, 40).

[36] C Rubbia, M Vignolini, D Prischich, A Miliozzi, and GM Giannuzzi. *Parabolic solar concentrator module*. US Patent App. 10/720, 632. 2003 (cit. on p. 22).

[37] A Miliozzi, GM Giannuzzi, and D Nicolini. *Linee guida per la progettazione strutturale di un concentratore solare*. Tech. rep. ENEA, 2006 (cit. on p. 22).

[38] C Rondoni, M Chieruzzi, A Miliozzi, D Nicolini, L Torre, and JM Kenny. “Use of composite structures for linear parabolic solar-energy collectors”. In: *26th International Conference SAMPE Europe*. April 2005 (cit. on p. 22).

[39] A Valan Arasu and T Sornakumar. “Design, manufacture and testing of fiberglass reinforced parabola trough for parabolic trough solar collectors”. In: *Solar Energy* 81.10 (2007), pp. 1273–1279 (cit. on pp. 22, 40).

[40] N Rosado Hau and MA Escalante Soberanis. “Efficiency of a parabolic trough collector as a water heater system in Yucatán, Mexico”. In: *Journal of Renewable and Sustainable Energy* 3.6, 063108 (2011), (cit. on pp. 22, 40).

[41] E Venegas-Reyes, OA Jaramillo, R Castrejón-García, JO Aguilar, and F Sosa-Montemayor. “Design, construction, and testing of a parabolic trough solar concentrator for hot water and low enthalpy steam generation”. In: *Journal of Renewable and Sustainable Energy* 4.5 (2012), p. 053103 (cit. on pp. 22, 29, 40).

[42] OA Jaramillo, E Venegas-Reyes, JO Aguilar, R Castrejón-García, and F Sosa-Montemayor. “Parabolic trough concentrators for low enthalpy processes”. In: *Renewable Energy* 60 (2013), pp. 529–539 (cit. on pp. 22, 29, 40).

[43] G Coccia, G Di Nicola, and M Sotte. “Design, manufacture, and test of a prototype for a parabolic trough collector for industrial process heat”. In: *Renewable Energy* 74 (2015), pp. 727–736 (cit. on pp. 22, 24, 40, 54).

[44] M Sotte. “Design, test and mathematical modeling of parabolic trough solar collectors”. PhD thesis. Università Politecnica delle Marche, 2012 (cit. on pp. 23, 24, 27, 28, 57).

[45] BD Agarwal, LJ Broutman, and K Chandrashekhara. *Analysis and Performance of Fiber Composites*. John Wiley & Sons, 2006 (cit. on p. 24).

[46] Wacker. *Hand lay-up*. Wacker Chemie AG. 2016. URL: `https://www.wacker.com/cms/en/industries/pl_composites/pl_comp_appl/handlayup.jsp` (cit. on p. 25).

[47] X Fu, C Zhang, R Liang, B Wang, and JC Fielding. "High temperature vacuum assisted resin transfer molding of phenyl-ethynyl terminated imide composites". In: *Polymer Composites* 32.1 (2011), pp. 52–58 (cit. on p. 25).

[48] F Lorenzetti. *Design and manufacturing of a parabolic trough solar concentrator for thermal oil heating applications*. Master's Thesis, Università Politecnica delle Marche. 2011 (cit. on pp. 26, 27, 29).

[49] Alanod-Solar GmbH & Co. KG. *MIRO-SUN®*. 2010 (cit. on pp. 28, 82).

[50] JJ Michalsky. "The Astronomical Almanac's algorithm for approximate solar position (1950–2050)". In: *Solar Energy* 40.3 (1988), pp. 227–235 (cit. on pp. 30, 51).

[51] *ANSI/ASHRAE Standard 93-2010 (RA2014), Methods of Testing to Determine the Thermal Performance of Solar Collectors*. 2014 (cit. on pp. 33, 37, 41, 51, 54, 124, 126).

[52] *ISO Standard 9060:1990, Solar Energy – Specification and Classification of Instruments for Measuring Hemispherical Solar and Direct Solar Radiation*. 1990 (cit. on pp. 36, 83).

[53] Eppley Laboratory, Inc. *ST-1 Normal Incedence Pyrheliometer*. 12 Sheffield Avenue, PO Box 419, Newport, RI (cit. on pp. 36, 83).

[54] HM Güven and RB Bannerot. "Derivation of universal error parameters for comprehensive optical analysis of parabolic troughs". In: *Journal of Solar Energy Engineering* 108.4 (1986) (cit. on pp. 37, 105–107).

[55] SM Jeter, DI Jarrar, and SA Moustafa. "Geometrical effects on the performance of trough collectors". In: *Solar Energy* 30.2 (1983), pp. 109–113 (cit. on pp. 37, 41, 51, 108, 109).

[56] G Coccia, G Latini, and M Sotte. "Mathematical modeling of a prototype of parabolic trough solar collector". In: *Journal of Renewable and Sustainable Energy* 4 (2012), p. 023110 (cit. on pp. 37, 113).

[57] SA Kalogirou. "Parabolic trough collector system for low temperature steam generation: design and performance characteristics". In: *Applied Energy* 55.1 (1996), pp. 1–19 (cit. on p. 40).

[58] P Hurtado and M Kast. "Experimental study of direct in-situ generation of steam in a line focus solar collector". In: *Report Number: DOE/SF/11946-T1, SERI* (1984) (cit. on p. 40).

[59] LM Murphy and EK May. *Steam Generation in Line-Focus Solar Collectors: a Comparative Assessment of Thermal Performance, Operating Stability, and Cost Issues*. Tech. rep. Solar Energy Research Inst., Golden, CO (USA), 1982 (cit. on p. 40).

[60] V Gnielinski. "New equations for heat and mass transfer in the turbulent flow in pipes and channels". In: *NASA STI/Recon Technical Report A* 41.1 (1975), pp. 8–16 (cit. on pp. 39, 55, 61, 116).

[61] CF Colebrook. “Turbulent flow in pipes, with particular reference to the transition region between the smooth and rough pipe laws”. In: *Journal of the ICE* 11.4 (1939), pp. 133–156 (cit. on pp. 39, 64, 116).

[62] W Wagner and HJ Kretzschmar. *International Steam Tables – Properties of Water and Steam based on the Industrial Formulation IAPWS-IF97*. Ed. by Springer. 2008 (cit. on pp. 39, 48).

[63] SUS Choi and JA Eastman. “Enhancing thermal conductivity of fluids with nanoparticles”. In: *ASME-Publications-Fed* 231 (1995), pp. 99–106 (cit. on p. 43).

[64] A Kasaeian, S Daviran, RD Azarian, and A Rashidi. “Performance evaluation and nanofluid using capability study of a solar parabolic trough collector”. In: *Energy Conversion and Management* 89 (2015), pp. 368–375 (cit. on p. 43).

[65] A Kasaeian, AT Eshghi, and M Sameti. “A review on the applications of nanofluids in solar energy systems”. In: *Renewable and Sustainable Energy Reviews* 43 (2015), pp. 584–598 (cit. on p. 44).

[66] AN Al-Shamani, MH Yazdi, MA Alghoul, AM Abed, MH Ruslan, S Mat, and K Sopian. “Nanofluids for improved efficiency in cooling solar collectors – A review”. In: *Renewable and Sustainable Energy Reviews* 38 (2014), pp. 348–367 (cit. on p. 44).

[67] S Ferrouillat, A Bontemps, JP Ribeiro, JA Gruss, and O Soriano. “Hydraulic and heat transfer study of SiO_2/water nanofluids in horizontal tubes with imposed wall temperature boundary conditions”. In: *International Journal of Heat and Fluid Flow* 32.2 (2011), pp. 424–439 (cit. on p. 44).

[68] L Zhang, J Lv, M Bai, and D Guo. “Effect of Vibration on Forced Convection Heat Transfer for SiO_2–Water Nanofluids”. In: *Heat Transfer Engineering* 36.5 (2015), pp. 452–461 (cit. on p. 44).

[69] WH Azmi, KV Sharma, PK Sarma, R Mamat, S Anuar, and LS Sundar. “Numerical validation of experimental heat transfer coefficient with SiO_2 nanofluid flowing in a tube with twisted tape inserts”. In: *Applied Thermal Engineering* 73.1 (2014), pp. 296–306 (cit. on p. 44).

[70] J Buongiorno, DC Venerus, N Prabhat, T McKrell, J Townsend, R Christianson, YV Tolmachev, P Keblinski, LW Hu, and JL Alvarado. “A benchmark study on the thermal conductivity of nanofluids”. In: *Journal of Applied Physics* 106.9 (2009), p. 094312 (cit. on p. 44).

[71] S Bobbo, L Colla, M Scattolini, F Agresti, S Barison, C Pagura, and L Fedele. “Thermal conductivity and viscosity measurements of water-based silica nanofluids”. In: *Proceedings of the Nanotech Conference and Expo*. 2011 (cit. on pp. 44, 46).

[72] YJ Chen, PY Wang, and ZH Liu. “Application of water-based SiO_2 functionalized nanofluid in a loop thermosyphon”. In: *International Journal of Heat and Mass Transfer* 56.1 (2013), pp. 59–68 (cit. on p. 44).

[73] AM Hussein, RA Bakar, and K Kadirgama. “Study of forced convection nanofluid heat transfer in the automotive cooling system”. In: *Case Studies in Thermal Engineering* 2 (2014), pp. 50–61 (cit. on p. 44).

[74] SMS Murshed, KC Leong, and C Yang. “Enhanced thermal conductivity of TiO_2–water based nanofluids”. In: *International Journal of Thermal Sciences* 44.4 (2005), pp. 367–373 (cit. on p. 44).

[75] WJ Tseng and KC Lin. “Rheology and colloidal structure of aqueous TiO_2 nanoparticle suspensions”. In: *Materials Science and Engineering* 355.1 (2003), pp. 186–192 (cit. on p. 44).

[76] TX Phuoc and M Massoudi. “Experimental observations of the effects of shear rates and particle concentration on the viscosity of Fe_2O_3–deionized water nanofluids”. In: *Int. Journal of Thermal Sciences* 48.7 (2009), pp. 1294–1301 (cit. on p. 44).

[77] MJ Pastoriza-Gallego, L Lugo, JL Legido, and MM Piñeiro. “Rheological non-Newtonian behaviour of ethylene glycol-based Fe_2O_3 nanofluids”. In: *Nanoscale Research Letters* 6.1 (2011), pp. 1–7 (cit. on p. 44).

[78] Y Vermahmoudi, SM Peyghambarzadeh, SH Hashemabadi, and M Naraki. “Experimental investigation on heat transfer performance of water nanofluid in an air-finned heat exchanger”. In: *European Journal of Mechanics-B/Fluids* 44 (2014), pp. 32–41 (cit. on p. 44).

[79] TH Tsai, LS Kuo, Ph Chen, DS Lee, and CT Yang. “Applications of ferro-nanofluid on a micro-transformer”. In: *Sensors* 10.9 (2010), pp. 8161–8172 (cit. on p. 44).

[80] TH Tsai, PH Chen, DS Lee, and CT Yang. “Investigation of electrical and magnetic properties of ferro-nanofluid on transformers”. In: *Nanoscale Research Letters* 6.1 (2011), pp. 1–5 (cit. on p. 44).

[81] I Nkurikiyimfura, Y Wang, and Z Pan. “Heat transfer enhancement by magnetic nanofluids – A review”. In: *Renewable and Sustainable Energy Reviews* 21 (2013), pp. 548–561 (cit. on p. 44).

[82] S Ferrouillat, A Bontemps, O Poncelet, O Soriano, and JA Gruss. “Influence of nanoparticle shape factor on convective heat transfer and energetic performance of water-based SiO_2 and ZnO nanofluids”. In: *Applied Thermal Engineering* 51.1 (2013), pp. 839–851 (cit. on p. 44).

[83] GJ Lee, CK Kim, MK Lee, CK Rhee, S Kim, and C Kim. “Thermal conductivity enhancement of ZnO nanofluid using a one-step physical method”. In: *Thermochimica Acta* 542 (2012), pp. 24–27 (cit. on p. 44).

[84] MT Zafarani-Moattar and R Majdan-Cegincara. “Effect of temperature on volumetric and transport properties of nanofluids containing ZnO nanoparticles poly (ethylene glycol) and water”. In: *The Journal of Chemical Thermodynamics* 54 (2012), pp. 55–67 (cit. on p. 44).

[85] T Sokhansefat, AB Kasaeian, and F Kowsary. “Heat transfer enhancement in parabolic trough collector tube using Al_2O_3/synthetic oil nanofluid”. In: *Renewable and Sustainable Energy Reviews* 33 (2014), pp. 636–644 (cit. on p. 44).

[86] M Kole and TK Dey. “Thermal conductivity and viscosity of Al_2O_3 nanofluid based on car engine coolant”. In: *Journal of Physics D: Applied Physics* 43.31 (2010), p. 315501 (cit. on p. 44).

[87] T Yousefi, F Veysi, E Shojaeizadeh, and S Zinadini. “An experimental investigation on the effect of Al_2O_3–H_2O nanofluid on the efficiency of flat-plate solar collectors”. In: *Renewable Energy* 39.1 (2012), pp. 293–298 (cit. on p. 44).

[88] CY Tsai, HT Chien, PP Ding, B Chan, TY Luh, and PH Chen. “Effect of structural character of gold nanoparticles in nanofluid on heat pipe thermal performance”. In: *Materials Letters* 58.9 (2004), pp. 1461–1465 (cit. on p. 45).

[89] B Wang, X Wang, W Lou, and J Hao. “Gold-ionic liquid nanofluids with preferably tribological properties and thermal conductivity”. In: *Nanoscale Research Letters* 6.1 (2011), pp. 1–10 (cit. on p. 45).

[90] N Shalkevich, W Escher, T Burgi, B Michel, L Si-Ahmed, and D Poulikakos. “On the thermal conductivity of gold nanoparticle colloids”. In: *Langmuir* 26.2 (2009), pp. 663–670 (cit. on p. 45).

[91] L Fedele, L Colla, and S Bobbo. “Viscosity and thermal conductivity measurements of water-based nanofluids containing titanium oxide nanoparticles”. In: *International Journal of Refrigeration* 35.5 (2012), pp. 1359–1366 (cit. on p. 46).

[92] L Colla, L Fedele, M Scattolini, and S Bobbo. “Water-Based Fe_2O_3 Nanofluid Characterization: Thermal Conductivity and Viscosity Measurements and Correlation”. In: *Advances in Mechanical Engineering* (2011) (cit. on p. 46).

[93] L Colla, L Marinelli, L Fedele, S Bobbo, and O Manca. “Characterization and Simulation of the Heat Transfer Behaviour of Water-Based ZnO Nanofluids”. In: *Journal of Nanoscience and Nanotechnology* 15.5 (2015), pp. 3599–3609 (cit. on pp. 46, 55, 61).

[94] G Coccia, G Di Nicola, L Colla, L Fedele, and M Scattolini. “Adoption of nanofluids in low-enthalpy parabolic trough solar collectors: Numerical simulation of the yearly yield”. In: *Energy Conversion and Management* 118 (2016), pp. 306–319 (cit. on p. 46).

[95] EW Lemmon, MO McLinden, and ML Huber. *REFPROP: Reference Fluid Thermodynamic and Transport Properties, NIST Standard Reference Database 23, Version 9.0, National Institute of Standards and Technology, Gaithersburg, MD.* 2010 (cit. on p. 46).

[96] S Bobbo, L Fedele, A Benetti, L Colla, M Fabrizio, C Pagura, and S Barison. “Viscosity of water based SWCNH and TiO_2 nanofluids”. In: *Experimental Thermal and Fluid Science* 36 (2012), pp. 65–71 (cit. on p. 46).

[97] *The Astronomical Almanac.* U.S. Gov’t. Printing Office, 1986 (cit. on p. 51).

[98] WA Beckman, SA Klein, and JA Duffie. *Solar Heating Design.* Wiley, 1977 (cit. on p. 51).

[99] G Coccia, G Di Nicola, and A Hidalgo. *Parabolic Trough Collector Prototypes for Low-Temperature Process Heat.* Springer, 2016 (cit. on p. 55).

[100] F Spinelli. *La Stima della Radiazione Solare mediante Immagini Satellitari.* Tech. rep. ENEA, Unità Tecnica Fonti Rinnovabili, Laboratorio Progettazione Componenti e Impianti, 2011 (cit. on pp. 56, 57).

[101] Weather Underground Inc. *Wunderground Meteorological Database.* URL: `http://www.wunderground.com` (cit. on p. 57).

[102] YA Çengel and AJ Ghajar. *Heat and Mass Transfer: Fundamentals & Applications.* McGraw-Hill, 2011 (cit. on p. 66).

[103] AVN Rao, TLS Rao, and S Subramanyam. “Mirror boosters for solar cookers – I”. In: *Energy Conversion and Management* 28.3 (1988), pp. 265–269 (cit. on p. 71).

[104] AVN Rao, TLS Rao, and S Subramanyam. “Mirror boosters for solar cookers – III”. In: *Energy Conversion and Management* 32.1 (1991), pp. 51–58 (cit. on p. 71).

[105] MB Habeebullah, AM Khalifa, and I Olwi. "The oven receiver: an approach toward the revival of concentrating solar cookers". In: *Solar Energy* 54.4 (1995), pp. 227–237 (cit. on p. 71).

[106] A Harmim, M Belhamel, M Boukar, and M Amar. "Experimental investigation of a box-type solar cooker with a finned absorber plate". In: *Energy* 35.9 (2010), pp. 3799–3802 (cit. on p. 72).

[107] VM Shrestha. "Modification of the solar cooker". In: *Solar & Wind Technology* 4.3 (1987), pp. 305–311 (cit. on p. 72).

[108] AR Reddy and AVN Rao. "Prediction and experimental verification of performance of box type solar cooker – Part I. Cooking vessel with central cylindrical cavity". In: *Energy Conversion and Management* 48.7 (2007), pp. 2034–2043 (cit. on p. 72).

[109] D Buddhi and LK Sahoo. "Solar cooker with latent heat storage: design and experimental testing". In: *Energy Conversion and Management* 38.5 (1997), pp. 493–498 (cit. on p. 72).

[110] R Domanski, AA El-Sebaii, and M Jaworski. "Cooking during off-sunshine hours using PCMs as storage media". In: *Energy* 20.7 (1995), pp. 607–616 (cit. on p. 72).

[111] A Saxena, SP Pandey, and G Srivastav. "A thermodynamic review on solar box type cookers". In: *Renewable and Sustainable Energy Reviews* 15.6 (2011), pp. 3301–3318 (cit. on p. 73).

[112] NM Nahar, RH Marshall, and BJ Brinkworth. "Studies on a hot box solar cooker with transparent insulation materials". In: *Energy Conversion and Management* 35.9 (1994), pp. 787–791 (cit. on p. 73).

[113] RS Mishra and SP Sabberwal Prakash. "Evaluation of solar cooker thermal performance using different insulating materials". In: *International Journal of Energy Research* 8.4 (1984), pp. 393–396 (cit. on p. 73).

[114] G Crovatto. *Costruzione di un Forno ad Alta Efficienza*. 2011. URL: `http://digilander.libero.it/giannicrovatto/f-effic.htm` (cit. on pp. 73, 76, 77).

[115] AMA Khalifa, MMA Taha, and M Akyurt. "Solar cookers for outdoors and indoors". In: *Energy* 10.7 (1985), pp. 819–829 (cit. on pp. 84, 85).

[116] SC Mullick, TC Kandpal, and AK Saxena. "Thermal test procedure for box-type solar cookers". In: *Solar Energy* 39.4 (1987), pp. 353–360 (cit. on p. 85).

[117] PA Funk. "Evaluating the international standard procedure for testing solar cookers and reporting performance". In: *Solar Energy* 68.1 (2000), pp. 1–7 (cit. on pp. 85, 91–93, 96).

[118] PJ Lahkar, RK Bhamu, and SK Samdarshi. "Enabling inter-cooker thermal performance comparison based on cooker opto-thermal ratio (COR)". In: *Applied Energy* 99 (2012), pp. 491–495 (cit. on pp. 86, 93, 95, 96).

[119] OO Fasina and Z Colley. "Viscosity and specific heat of vegetable oils as a function of temperature: 35 °C to 180 °C". In: *International Journal of Food Properties* 11.4 (2008), pp. 738–746 (cit. on pp. 88, 93).

[120] SC Mullick, TC Kandpal, and S Kumar. "Testing of box-type solar cooker: second figure of merit F2 and its variation with load and number of pots". In: *Solar Energy* 57.5 (1996), pp. 409–13 (cit. on p. 91).

[121] D Buddhi, SD Sharma, and RL Sawhney. “Performance test of a box-type solar cooker: effect of load on the second figure of merit”. In: *International Journal of Energy Research* 23.9 (1999), pp. 827–830 (cit. on p. 91).

[122] AA El-Sebaii and A Ibrahim. “Experimental testing of a box-type solar cooker using the standard procedure of cooking power”. In: *Renewable Energy* 30.12 (2005), pp. 1861–1871 (cit. on pp. 91, 94, 96).

[123] VP Sethi, DS Pal, and K Sumathy. “Performance evaluation and solar radiation capture of optimally inclined box type solar cooker with parallelepiped cooking vessel design”. In: *Energy Conversion and Management* 81 (2014), pp. 231–241 (cit. on p. 92).

[124] TP Otanicar, PE Phelan, RS Prasher, G Rosengarten, and RA Taylor. “Nanofluid-based direct absorption solar collector”. In: *Journal of Renewable and Sustainable Energy* 2.3 (2010), p. 033102 (cit. on p. 98).

[125] M Chieruzzi, GF Cerritelli, A Miliozzi, and JM Kenny. “Effect of nanoparticles on heat capacity of nanofluids based on molten salts as PCM for thermal energy storage”. In: *Nanoscale Research Letters* 8.1 (2013), p. 1 (cit. on p. 98).

[126] A Miliozzi, E Veca, S Sau, R Grena, M Celino, M Falconieri, and F Rondino. “Individuazione e caratterizzazione di miscele di materiali a cambiamento di fase e nanoparticelle da impiegare come sistemi alternativi di accumulo termico”. In: *Report Ricerca di Sistema Elettrico, Accordo di Programma Ministero dello Sviluppo Economico–ENEA* (2013) (cit. on p. 98).

[127] M Chieruzzi, JM Kenny, and A Miliozzi. “Studio e sviluppo di un mezzo di accumulo a calore latente a media temperatura (200–400 °C) costituito da una miscela di sali e nanoparticelle”. In: *Report Ricerca di Sistema Elettrico, Accordo di Programma Ministero dello Sviluppo Economico–ENEA* (2013) (cit. on p. 98).

[128] M Chieruzzi, A Miliozzi, T Crescenzi, L Torre, and JM Kenny. “A new phase change material based on potassium nitrate with silica and alumina nanoparticles for thermal energy storage”. In: *Nanoscale Research Letters* 10.1 (2015), p. 1 (cit. on p. 98).

[129] A Rabl. “Comparison of Solar Concentrators”. In: *Solar Energy* 18.2 (1976), pp. 93–111 (cit. on p. 103).

[130] RE Forristall. *Heat Transfer Analysis and Modeling of a Parabolic Trough Solar Receiver Implemented in Engineering Equation Solver.* Tech. rep. National Renewable Energy Laboratory, 2003 (cit. on p. 113).

[131] A Ratzel, C Hickox, and D Gartling. “Techniques for reducing thermal conduction and natural convection heat losses in annular receiver geometries”. In: *Journal of Heat Transfer* 101.1 (1979), pp. 108–113 (cit. on p. 116).

[132] N Marshal. *Gas Encyclopedia.* New York: Elsevier, Transl. 1976 (cit. on p. 117).

[133] KGT Hollands, GD Raithby, and L Konicek. “Correlation equations for free convection heat transfer in horizontal layers of air and water”. In: *International Journal of Heat and Mass Transfer* 18.7 (1975), pp. 879–884 (cit. on p. 117).

[134] SW Churchill and M Bernstein. “A correlating equation for forced convection from gases and liquids to a circular cylinder in crossflow”. In: *ASME Transactions Journal of Heat Transfer* 99 (1977), pp. 300–306 (cit. on p. 119).

[135] SW Churchill and HHS Chu. “Correlating equations for laminar and turbulent free convection from a horizontal cylinder”. In: *International Journal of Heat and Mass Transfer* 18.9 (1975), pp. 1049–1053 (cit. on p. 119).

[136] M Martin and P Berdahl. “Characteristics of infrared sky radiation in the United States”. In: *Solar Energy* 33.3 (1984), pp. 321–336 (cit. on p. 119).

[137] *ISO Standard 9806:2013, Solar Energy – Solar Thermal Collectors – Test Methods*. 2013 (cit. on p. 123).

[138] *ANSI/ASHRAE Standard 93-1986, Methods of Testing to Determine the Thermal Performance of Solar Collectors*. 1986 (cit. on p. 124).

[139] *EN 12975-1:2000 Thermal Solar Systems and Components – Solar Collectors – Part 1: General Requirements*. 2000 (cit. on p. 124).

[140] *EN 12975-2:2001 Thermal Solar Systems and Components – Solar Collectors – Part 2: Test Methods*. 2001 (cit. on p. 124).

[141] Working Group 1 of the Joint Committee for Guides in Metrology. *Evaluation of Measurement Data – Guide to the Expression of Uncertainty in Measurement*. Ed. by JCGM. 2008 (cit. on p. 130).